SCIENCE CHINA
Physics, Mechanics & Astronomy

•Invited Review•
Special Topic: Advances in Pulsed Laser Synthesis of Nanoparticles in Liquids

July 2022 Vol. 65 No. 7: 274203
https://doi.org/10.1007/s11433-021-1860-x

Diverse nanomaterials synthesized by laser ablation of pure metals in liquids

DongShi Zhang[1*], ZhuGuo Li[1,2*], and ChangHao Liang[3,4*]

[1] *Shanghai Key Laboratory of Materials Laser Processing and Modification, School of Materials Science and Engineering, Shanghai Jiao Tong University, Shanghai 200240, China;*
[2] *State Key Lab of Metal Matrix Composites, School of Materials Science and Engineering, Shanghai Jiao Tong University, Shanghai 200240, China;*
[3] *Key Laboratory of Materials Physics and Anhui Key Laboratory of Nanomaterials and Nanotechnology, Institute of Solid State Physics, Chinese Academy of Sciences, Hefei 230031, China;*
[4] *Department of Materials Science and Engineering, University of Science and Technology of China, Hefei 230026, China*

Received November 13, 2021; accepted January 17, 2022; published online May 31, 2022

Diverse nanomaterials, in the forms of carbides, sulfides, oxides, metals, hydroxides, etc., have been synthesized by laser ablation in liquids (LAL) with metal targets as the dominant educts. Many advantages of LAL technique itself and its products have been revealed since 1983 when the first report about LAL was released. Different from traditional wet-chemical synthesis, one unique feature of LAL is its resultant extreme high-temperature and high-pressure local environment for the nucleation and growth of nanomaterials, despite being performed at room temperature. This extreme condition can induce the atomization and ionization of the target materials and liquid molecules to incur different chemical reactions. The laser, liquid, liquid additive, and target can significantly alter the local environment in a broad range. Thus, different phases and shapes of nanomaterials are producible even from the same target. Through directly comparing the products of LAL of 13 kinds of chosen representative metals synthesized under different conditions, this review presents and discusses current understandings, challenging issues, and perspectives related to the diversity of LAL-products, which is willing to promote a deeper investigation and discussion on a clear clarification of the chemical reactions and particle nucleation/growth processes.

nanomaterial synthesis, laser ablation in liquid, phase manipulation, morphology diversity

PACS number(s): 81.07.-b, 79.20.Ds, 78.67.Bf, 81.10.Dn

Citation: D. S. Zhang, Z. G. Li, and C. H. Liang, Diverse nanomaterials synthesized by laser ablation of pure metals in liquids, Sci. China-Phys. Mech. Astron. **65**, 274203 (2022), https://doi.org/10.1007/s11433-021-1860-x

1 Introduction

Nowadays, the development of nanomaterials in many fields related to human life and industry is rapidly advancing. With the emergence of extreme weather due to the CO_2-induced greenhouse effect, developing renewable and sustainable energy to build smart cities and industries [1] is important for the long-run interests of humankind, where high-performance nanocatalysts are critical keys [2]. Future flexible electronics also resort to 1D and 2D hybrid nanomaterials [3]. Other applications related to environmental remediation (such as removal of radionuclides [4] and heavy metal ions [5]), and biomedicine (such as photothermal therapy [6], antibacterial [7], and drug delivery [8]) are as well the driving forces that push forward enriching the diversity of

*Corresponding authors (DongShi Zhang, email: zhangdongshi@sjtu.edu.cn; ZhuGuo Li, email: lizg@sjtu.edu.cn; ChangHao Liang, email: chliang@issp.ac.cn)

nanomaterials and elevating the performance of nanomaterials, which consequently promote the exploration and innovation of bottom-up and top-down nanomaterial synthesis techniques [9].

Owing to the invention of the laser system by Maiman [10] in 1960 and its continuous innovation with a milestone of chirped pulse amplification, ultrashort lasers with high powers and short pulse durations and increasingly low prices have become accessible to researchers, which open up many avenues for material processing, such as laser cutting [11], laser functional structuring [12-16], laser machining [17], laser cross-linking [18], 3D/4D laser printing [19-21], additive manufacturing [22], and laser patterning [23,24]. Unlike laser additive manufacturing and laser printing techniques that are aimed to construct 3D or 4D structures from smaller-scale building blocks, laser ablation is a subtractive manufacturing technique with micro/nanomaterials as the subtractive materials [11,25]. Confined in liquids to ensure the security of operators and to realize *in situ* nanomaterial dispersion, laser-based nanomaterial synthesis techniques, including laser ablation in liquids (LAL), laser fragmentation in liquids (LFL), laser melting in liquids (LML), and laser defect engineering in liquids (LDL) (Figure 1), have become an important branch of nanomaterial synthesis techniques [26], which can trace back to its first discovery in 1983 [27]. After almost three decades of development, many advantages of these techniques have been unveiled, including extreme convenience, capacity in processing any bulky materials, cost-effective educts, synthesis of pure nanocrystals, remote-control operation, and green synthesis of high-purity products without the need of chemicals (Figure 1) [26,28]. High-purity makes LAL-synthesized nanomaterials highly competitive for applications in catalyst-based applications [29-31].

Numerous reviews have been published to introduce the progress in LAL, LFL, LML, and LDL from the fundamental and applicational perspectives, with LAL prevailing in the reports. Explosive growth in the review/perspective publication number has been witnessed since 2017, which indicates the gradually rising status of laser-based synthesis techniques in nanoscience. Barcikowski's group [28] comprehensively reviewed the fundamentals and applications of laser synthesis and processing of colloids (LSPC) in liquids and summarized the advantages of this technique and colloids for various applications. Moreover, they reviewed the progress in applying laser colloids for heterogeneous catalysis [29]. Yang's group [32] reviewed how to combine multiple external fields (e.g., magnetic, electric, and electrochemical) with LAL to diversify the products. Kanitz et al. [33] introduced the critical factors that influence particle formation in the early stages of LAL. Zhang et al. [34,35] proposed six growth mechanisms for laser-synthesized nanomaterials and explained how to utilize LSPC and its compatible downstream processes to prepare particle-polymer composites [35]. Müller's [36] and Ma's [31], and Liang's [30] groups summarized the merits of using laser-synthesized nanomaterials for catalytic applications. Liang and his colleagues [37] provided their perspectives on how to produce amorphous metal nanoparticles (NPs) and where to apply them. Magnetic particles/composites [38], monometallic and bimetallic Ni-Based NPs [39], rare-earth doped NPs [40], Ag NPs and their application as antimicrobial

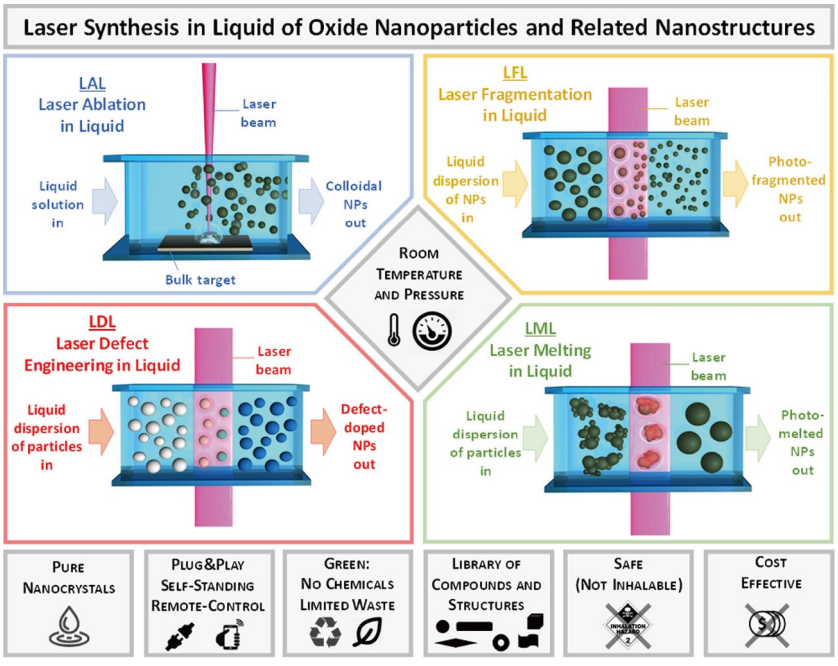

Figure 1 (Color online) Sketch of LAL, LFL, LML, and LDL and their advantages. Copied from ref. [26] with permission.

agents [41], and diversities of liquids and targets used for LAL [42] have also been reviewed in recent years. Despite the existence of many reviews/perspectives, how to control the phases of laser-synthesized nanomaterials is still challenging because of enormous laser and processing parameters and the diversity of liquid compositions. A direct comparison of various products from the same educt target is needed to shed light on the critical factors that govern the nucleation and growth of desirable nanomaterials.

Various types of nanomaterials are attainable from the majority of elemental metal materials in the periodic table, including alkaline metals, alkaline earth metals, transition metals, main group metals, lanthanides, and actinium series. Alkaline metals such as Li and Na are active and dangerous to be put into liquids; hence no report about LAL of alkaline metals has been published. Within the scope of alkaline earth metals, only LAL of Mg has been studied. For main group metals, many studies focused on LAL of Al, Bi, Sn [43-57], and Ge [58-67], but few reports are available on Sb [68-70], In [71,72], and Pb [73,74]. Transition metals are most frequently investigated for LSPC, which can be transformed into different phases of metals, oxides, sulfides, nitrides, carbides, hydroxides, and metal-polymer composites via reactive laser ablation in liquids (RLAL). In view of the great potential for these products to be used in multiple applications, their progress deserves special attention to clarify how a chemical reaction or phase evolution takes place. Most lanthanides are used as dopants, whereas actinium series metals are radioactive. Hence, this review mainly focuses on the progress in nanomaterials synthesized starting from transition metals and provides a short introduction about an alkaline earth metal and a main group metal. In specific, Mg is selected as the representative for alkaline earth metals, Ti/Mn/Fe/Co/Cu/Zn/Ru/Rh/Pd/Pt for transition metals, and Al for main group metals. With respect to the selected transition metals, Ru/Rh/Pd/Pt are precious metals that are less reviewed compared with Au and Ag in previous reviews [29,41,75]. Thus, the present review briefly introduces the current states of LAL of Ru/Rh/Pd/Pt in liquids. The correlation of nanomaterial properties, such as phases and morphologies, with laser parameters and liquid compositions, is presented, and the corresponding potential reasons are discussed. Compared with other synthesis methods based on organic molecules, polymers, and biomolecules [76,77], morphological diversity of laser-synthesized nanomaterials lags far behind unless with the aid of aging colloids or triggering chemical reactions [28]. Thus, an emphasis is placed on the achievable nonspherical nanomaterials and their formation mechanisms/conditions. For Pt/Pd particles that are widely used for catalysts [78,79], their particle size and shape really matter, which are the key points for the introduction. Finally, current challenges are summarized, and our perspectives on future development are presented.

Methodologies of LAL, LFL, LML, and LDL have been reviewed elsewhere [26,28]. Most application reports did not show the unique advantages of laser-synthesized nanomaterials. They are only briefly introduced but not stressed in this review unless they have some fundamental breakthroughs.

2 Alkaline earth metal (Mg)

Elemental magnesium (Mg) is an actively flammable material. Once burned, Mg releases immense heat instantaneously and may trigger an explosion. Hence, the synthesis of pure Mg nanomaterials starting from bulky metal targets is challenging but achievable via LAL, which is beneficial because of its incapability to react with water and organic solvents at room temperature. Synthesis of pure Mg nanomaterials under optimized environments is feasible following two methodologies. One synthesis route is to prevent the generation of reactants (e.g., oxygen or hydroxyl) during LAL that can react with Mg atoms/ions. In this regard, organic solvents that can provide a reductive environment (i.e., CO, CH_4, etc.) during LAL [80] are preferable for LAL of Mg, which can decompose MgO even when they form during LAL. By removing the dissolved oxygen gases in liquids using nitrogen (N_2) gases, ElFaham et al. [81] synthesized pure Mg nanomaterials by LAL of Mg in 2-butanol, as confirmed by X-ray diffraction (XRD). Prolonging the ablation time from 10 to 30 min slightly decreases the particle size from 30 to 21 nm. The other favorable synthesis route is to encapsulate Mg particles in a matrix to prevent their reaction with other active species. Organic-solvent dissolved polymer matrix solution (e.g., THF/PMMA, tetrahydrofuran (THF), poly(methyl methacrylate) (PMMA)) [82] offers a choice. XRD characterization (Figure 2(a)) of as-prepared nanocomposites indicates the formation of pure Mg particles (JCPDS 04-0770) without any MgO and $Mg(OH)_2$ impurities. Due to the size quenching effect induced by PMMA molecules, the particle size is small, with the majority less than 5 nm (Figure 2(b)). The synthesized PMMA-Mg polymer-particle composites have the potential to be used as catalysts for hydrogen storage [82].

Compared with pure Mg nanomaterials and Mg-polymer composites, $Mg(OH)_2$ and MgO nanomaterials presenting various morphologies such as spheres, lamellar, fibers, platelets, flowers, and cubes are much easier to be prepared by LAL, as listed in Table 1 [74,81-91], and they are as abundant as those prepared using top-down and bottom-up techniques [92]. Hollow structures originate from the cluster aggregation on the bubble interfaces generated during LAL [93]. The growth mechanism for nonspherical MgO nanostructures is difficult to clarify because of the ultrafast processes of LAL [28]. Other synthesis methods, such as the sol-

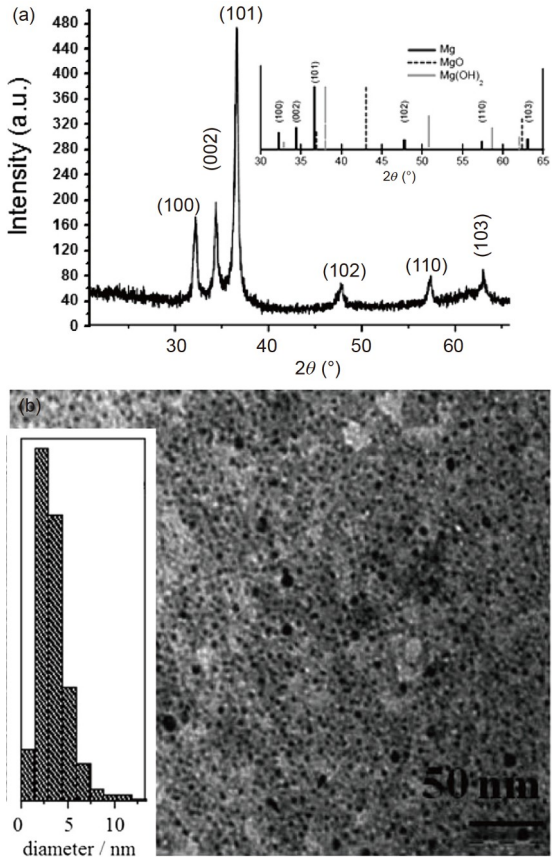

Figure 2 LAL-synthesized Mg/PMMA composites. (a) XRD spectrum of composites, where Mg, cubic MgO, and hexagonal $Mg(OH)_2$ featured peaks are included for identification. (b) Transmission electron microscope (TEM) image of Mg particles and corresponding size histogram. Copied from ref. [82] with permission.

gel method [94], may provide inspiration to speculate on the formation mechanism for LAL. LAL of organic solvents often causes the decomposition of organic solvent molecules, leading to the formation of C_xO_y or $C_xH_yO_z$ ion species, which may react with Mg^{2+} to form MgC_xO_y or $MgC_xH_yO_z$ in the plasma phase. Subsequent dehydration and decomposition of these compounds at temperatures of hundreds of °C lead to the formation of nanostructures with different morphologies [94]. Another possibility is that hydrocarbon byproducts generated by LAL or the solvent themselves serve as adsorbents to guide the anisotropic growth of MgO nanostructures.

The most frequently adopted liquid for LAL of Mg is water, sometimes with additives such as surfactants (e.g., sodium dodecyl sulfate (SDS) and sodium citrate (SC) [88]) and supporting materials (e.g., graphene oxide (GO) nanosheets [87]). Mixtures of MgO and $Mg(OH)_2$ are the main products of LAL of Mg in water and aqueous solutions. Aside from $Mg(OH)_2$ and MgO phases, $Mg_5O(OH)_8$ lamellar structures are also achievable in water [84]. Deduced from the formation of $Mg(OH)_2$, MgO, and $Mg_5O(OH)_8$, LAL in water should produce a large amount of oxygen and hydroxyl species that can react with Mg atoms/ions ejected from the target. MgO may be first generated and then evolve into $Mg(OH)_2$ through the reaction of $MgO + H_2O \rightarrow Mg(OH)_2$ [95]. The opposite decomposition reaction of $Mg(OH)_2$ into MgO occurs at ~370°C [96], which can also be induced during LAL. $Mg(OH)_2$ decomposition is a dehydration and heat storage process, whereas the evolution of MgO into $Mg(OH)_2$ is a hydration and heat output process [95]. Reaction cycles for hydration and dehydration processes can be tens of times [97]. After dehydration, the structural shape can be well preserved [98]. Successively incident pulses can continuously create a high-pressure, high-temperature environment and then induce its ultrafast quenching to room temperature. Repetitive hydration and dehydration reactions must have occurred during LAL. Hence, the mixture of $Mg(OH)_2$ and MgO phases can be simultaneously produced after LAL of Mg in water [84].

Only three reports demonstrated the possibility to produce pure $Mg(OH)_2$ nanostructures, including $Mg(OH)_2$ platelet-like structures produced in pure water [86], $Mg(OH)_2$ nanoflakes in water with GO [87] and SDS additives [90], respectively. In another report [88], the authors claimed that surfactants such as SDS or SC could inhibit the adsorption of water molecules on MgO. Thus, the chance to produce pure $Mg(OH)_2$ via the reaction between MgO and water molecules ($MgO\ (s) + H_2O \rightarrow Mg(OH)_2$) [95] is significantly reduced. In consequence, they produced the mixture of lamellar and hollow MgO and $Mg(OH)_2$ nanostructure [88], and so did the work performed by Pereira et al. [89]. As shown in Table 1, laser parameters (i.e., pulse duration, repetition rate, wavelength, and pulse energy) adopted for these three experiments are different, making it difficult to conclude which factor is critical for the generation of pure-phase Mg-based nanomaterials. Currently, how Mg atoms react with other species to form various products remains unclear, especially the reaction routes for the formation of abnormal species of $Mg_5O(OH)_8$ magnesium oxyhydroxide and pure $Mg(OH)_2$ nanostructures.

Organic solvents such as acetone [91], ethanol [74], ethyl acetate [84], *n*-hexane [84], and their mixtures [74] can further enrich the products of LAL of Mg, as listed in Table 1. Unlike aqueous solutions, MgO is the dominant phase produced in organic solvents [28], sometimes in a high purity. In the ambient environment, oxygen gases generally dissolve in liquids. Decomposition of organic molecules (e.g., ethanol, acetone) yields hydroxyl ions. Hence, the possibility of producing $Mg(OH)_2$ cannot be completely ruled out. Considering no discovery of $Mg(OH)_2$ phase in most studies of LAL in organic solvents. Thus, it is deduced that they should completely decompose into the MgO phase ($Mg(OH)_2 \rightarrow MgO + H_2O$). Following this speculation, the bubble temperature during $Mg(OH)_2$ nucleation should be much higher than that in water. Hence, the calcination pro-

Table 1 Summary of Mg-based nanomaterials synthesized by LAL of Mg in different liquids, gas environments using different laser parameters[a)]

Liquid	Laser	Atmosphere	Shape	Phase	Ref.
2-Butanol	7 ns, 1064 nm, 10 Hz, 90 mJ/pulse	N_2	–	Mg	[81]
Water	7 ns, 532 nm, 2 Hz	air	nanoflowers, nanofibers	Mg, MgO, $Mg(OH)_2$	[83]
Water	7 ns, 1064 nm, 20 Hz, 180 mJ/pulse	air	lamellar	$Mg_5O(OH)_8$, $Mg(OH)_2$, MgO	[84]
Water	7 ns, 1064 nm, 15 Hz, 200 mJ/pulse	air	lamellar	$Mg_5O(OH)_8$, $Mg(OH)_2$	[85]
Water	35 ns, 510.5/578 nm, 10 kHz	air	platelet-like	$Mg(OH)_2$	[86]
Water + GO	6 ns, 1064 nm, 10 Hz, 100 mJ/pulse	air	nanoflakes	$Mg(OH)_2$	[87]
Water, water + SDS/SC	30 ns, 10 Hz, 7.5 and 15 J/cm^2	air	lamellar, hollow	MgO, $Mg(OH)_2$	[88]
Water + SDS (0.025 mol/L)	35 ns, 1064 nm, 20 kHz, 2400, 4800, 9600, 19200 J/cm^2	air	nonspherical	Mg, MgO, $Mg(OH)_2$	[89]
Water + SDS (0, 0.001, 0.01, 0.05 mol/L)	7-8 ns, 355 nm, 10 Hz, 100 mJ/pulse	air	wormhole-like, fiber-like, rod-like and platelet-like	$Mg(OH)_2$	[90]
Ethyl acetate, ethanol, *n*-hexane	7 ns, 1064 nm, 20 Hz, 180 mJ/pulse	air	spheroidal, hollow	MgO, Mg	[84]
Acetone	240 ns, 1064 nm, 210 Hz, 3.5 mJ/pulse, 91 J/cm^2	air	square (AVG 1-1.5 μm)	Mg, MgO	[91]
Ethanol	1 ms, 1064 nm, 1 Hz, 10^6 W/cm^2	air	cubic	MgO	[74]
THF/PMMA	1064 nm, 10 Hz,	air	spherical (size dominates at 2-6 nm)	Mg	[82]
Ethanol/*n*-hexane (1:5 v/v)	1 ms, 1064 nm, 1 Hz, 10^6 W/cm^2	air	hollow	MgO	[74]

a) SDS, sodium dodecyl sulfate; SC, sodium citrate, PMMA, polymethylmethacrylate; THF, tetrahydrofuran; GO, graphene oxide; AVG, average size.

cess should be *in situ* triggered to induce the instantaneous transformation of $Mg(OH)_2$ into MgO.

Some attempts have been dedicated to the applications of LAL-synthesized MgO, $Mg(OH)_2$, and their mixed products. For example, LAL-prepared $Mg(OH)_2$ structures possess a good optical nonlinearity with a potential application in nonlinear optics [86]. Wang et al. [87] showed that $Mg(OH)_2$/GO composites synthesized by *in situ* LAL of Mg in GO solution are good photocatalysts and adsorbents for pollutant degradation and heavy metal removal. Nemoykina et al. [85] reported that LAL-synthesized lamellar $Mg_5O(OH)_8$ and $Mg(OH)_2$ structures are effective in increasing the transparency, strengthening and deacidification of old paper for its long-term restoration and conservation. However, compared with extensively reported physicochemical properties and applications of MgO and $Mg(OH)_2$ [92], the study on LAL-synthesized Mg-based nanomaterials is still in its infancy, and the advantages of LAL-synthesized Mg-containing nanomaterials over their counterparts obtained by other methods are still unclear, deserving further investigation.

3 Transition metals

3.1 Ti

Titanium, constituting 0.44% of the Earth's crust, is very reactive toward nitrogen, carbon, and oxygen during LAL, in which solvents and their decomposed products are reactants. Consequently, nitride, carbide, and oxide Ti-based nanomaterials are producible by LAL, as shown in Table 2 [99-114]. For example, Takada et al. [99] reported the possibility of triggering RLAL in liquid nitrogen to produce polycrystalline TiN particles with the N/Ti atomic ratio of 0.4. LAL of Ti in organic solvents such as ethanol, acetone, *n*-hexane, and toluene produces TiC@C core-shell particles [100]. The product phases strongly depend on the pulse duration of laser systems and the compositions of organic solvents. Nanosecond (ns) LAL of Ti in acetone generates pure TiC particles [101], whereas femtosecond (fs) LAL produces a mixture of TiC and TiO_x [100]. Oxidants come from the dissolved oxygen in liquids and LAL-decomposed organic molecules. The formation of pure TiC by ns-LAL is attributed to the thermal effect of ns lasers, which can trigger the reduction of TiO_x by carbon shells or reductive gases surrounding the particles. If aiming at producing TiC@C particles by fs-LAL, organic solvents whose molecular formula should not contain oxygen, such as toluene [100], and optimization of organic solvents for ns-LAL is not needed [101]. When bubbling organic solvents with hydrogen gases to make them saturated for ns-LAL, porous NPs with a cavity volume ratio of 20%-50% are achievable [102]. In the case of LAL in organic solvents (i.e., ethanol) using a continuous wave (CW) laser, TiO_x rather than TiC particles are generated. Three TiO_2 phases, including rutile, anatase, and brookite, are produced with brookite as the dominant phase [103]. Researchers only used fast Fourier transform to confirm the phases from only a few NPs; hence, some other phases may

Table 2 Summary of products obtained by LAL of Ti in different liquids, gas environments using different laser parameters[a)]

Liquid	Laser	Atmosphere + post-treatment	Shape	Phase	Ref.
Water	10 ns, 1064 nm, 10 Hz, 5 J/cm^2	air	spherical (AVG 34 nm)	amorphous TiO_x	[105]
Water + SDS (0, 0.001, 0.01, 0.1 mol/L)	355 nm, 10 Hz, 150 mJ/pulse, 60 min	air	spherical (AVG 3 nm)	amorphous, amorphous/anatase TiO_2	[106]
Water + SDS (0, 0.01 mol/L)	CW, 1070 nm, 250 W, 2×10^7 J/cm^2	air	spherical (AVG 27 and 40 nm)	anatase, anatase/rutile TiO_2	[104]
Ethanol	180 fs, 800 nm, 1 kHz, 2 J/cm^2; 70 ns, 1064 nm, 2 kHz	H_2	spherical (30-50 nm); facetted (>100 nm)	quasi-spherical with holes inside	[102]
Ethanol	CW, 200 W, 10^6 W/cm^2	air	spherical (5-50 nm)	rutile, anatase, brookite TiO_2	[103]
Water	5 ns, 532 nm, 15 Hz, 4 mJ/pulse	focus, below/above focus	spherical (13, 9, 12 nm)	$TiO_{1.5}$/TiO_2 (rutile), $TiO_{1.5}$/TiO_2 (anatase)/Ti, $TiO_{1.5}$	[107]
Water + PVP (0.01, 0.05 mol/L)	10 ns, 1064 nm, 80 mJ/pulse	air	spherical (AVG 35/55 nm)	rutile TiO_2	[108,109]
Water	10 ns, 532 nm, 80 J/cm^2	air	spherical (AVG 13 nm)	rutile TiO_2	[110]
Water	10 ns, 1064 nm, 1 Hz, 400 mJ/pulse,	air	spherical (40-110 nm)	anatase TiO_2	[111]
Water	CW, 1075 nm, 200 W, 1.3×10^7 W/cm^2	air + laser irradiation	spherical (AVG 11-17 nm)	rutile/anatase TiO_2	[112]
Water	8 ns, 1064 nm, 10 Hz, 120 mJ/pulse	air	spherical	anatase TiO_2	[113]
Water	6 ns, 1064 nm, 20 Hz, 20 J/cm^2	successive LAL of Pt	spherical (5-30 nm)	anatase TiO_2	[114]
Acetone	7 ns, 1064 nm, 100 mJ/pulse	air	core-shell (AVG 12.7 nm)	TiC@C	[101]
Acetone, *n*-hexane, toluene	100 fs, 800 nm, 1 kHz, 3 mJ/pulse,	air	core-shell (AVG 10, 19, 20 nm)	TiC/TiO_x@C, TiC@C, TiC@OLC	[100]
Liquid N_2	6 ns, 1.06 μm, 10 Hz, 1-30 J/cm^2	N_2	spherical (AVG 800 nm)	TiN	[99]

a) OLC, onion-like carbon; PVP, polyvinylpyrrolidone.

be omitted. Their results showed that CW laser is inefficient to decompose organic solvent molecules, at least much less efficient than ns and fs lasers. In addition, water boiling or ignition of organic solvents can be easily induced because of the strong thermal effect from CW lasers more than that from ns lasers. Thus, the ablation period for CW-LAL is normally constrained in a short period, such as 1 s [104]. Hence, CW-LAL has been seldomly reported, even though the products differ greatly from those generated by pulsed LAL. Of great interest, C–H-doped anatase nanospheres with disordered $C_{1-x}Si_x$:H shell and planar defects have been produced by LAL of Ti in tetraethyl orthosilicate (TEOS), which indicates the possibility to realize self-doping during LAL with the dopants originating from the decomposed liquid molecules [115].

Nonstoichiometric TiO_x and three stoichiometric phases of TiO_2, including rutile, anatase, and brookite, are the main products of LAL of Ti in aqueous solutions. The thermodynamic stability of rutile, anatase, and brookite is correlated with particle size. Anatase is more stable than rutile when the particle size is small, such as less than 14 nm [116] or less than 40 nm [117]. The most stable phase for TiO_2 particles 11-35 nm in diameter is brookite [118]. However, these empirical conclusions applicable to other synthesis methods are no longer relevant to LAL-synthesized particles because of superfast quenching. As shown in Table 2, anatase TiO_2 particles in small (i.e., ~5 nm [57]) and large dimensions (i.e., 40-110 nm [111]) and rutile particles with an average size of 13 nm [110] are all producible via LAL. Brookite is a metastable TiO_2 polymorph that is difficult to synthesize and only appears as a byproduct with anatase and rutile phases [103].

The phase of the colloids from LAL of Ti in aqueous solutions depends on the ablation condition (governing the temperature). For example, anatase TiO_2 particles can be produced by LAL at a low pulse energy of 1 mJ/pulse, characterized by an absorption peak at the wavelength of 253 nm, as shown in Figure 3 [119]. Increasing the pulse energy to 2 mJ/pulse leads to the emergence of a rutile-phase peak at ~337 nm, which becomes more apparent when the laser pulse energy is 3.5 mJ/pulse. This result indicates a preferable nucleation/growth of anatase and rutile at low and high pulse energies, respectively, which is in accordance with previous reports showing that anatase evolves into rutile while heating at hundreds of °C [120]. Interface nucleation between small anatase particles may occur, leading to the

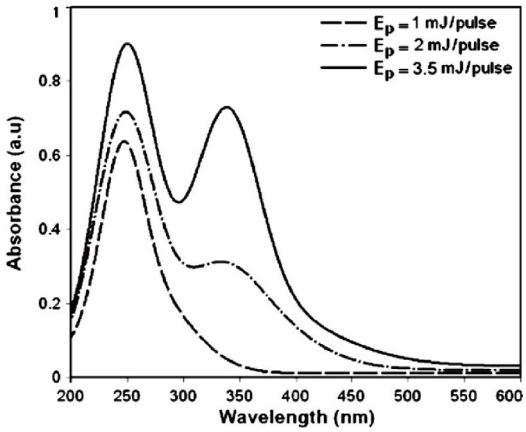

Figure 3 Optical absorption spectra of the titania NPs, synthesized by LAL of Ti in water at laser pulse energies of 1, 2, and 3.5 mJ. Copied from ref. [119] with permission.

formation of large rutile-phase TiO_2 particles [120]. The low heating rate causes the coarsening of particles, resulting in the formation of large rutile TiO_2 particles [120].

Sharma and Nath [121] performed a theoretical simulation and claimed that cavitation bubble collapse and shockwave promote the formation of the rutile phase through mechanical effects. However, the applicability of this simulation is doubtful because anatase and rutile TiO_2 particles have been generated by LAL; nevertheless, it provides a new mechanism to explain the formation of the rutile phase during LAL. X-ray photoelectron spectroscopy (XPS) analysis revealed that there are abundant oxygen vacancies on LAL-synthesized TiO_2 particles [122]. Photoluminescence (PL) characterization of LAL-synthesized anatase TiO_2 also confirms the formation of oxygen vacancy and interstitial titanium atoms [123]. Hence, even though XRD characterization indicates the formation of pure TiO_2 phases, some defects still exist on the surfaces or inside the particles.

Different types of nonstoichiometric TiO_x nanomaterials have been produced by LAL of Ti in water, such as TiO [124], Ti_8O_{15} [125], $TiO_{1.5}$ [107], and $TiO_{1.04}/Ti_2O_3$ [126]. The formation rate of $TiO_{1.5}$ particles depends on laser focus conditions because of the variation in laser fluence, which causes the change in the production rate and size of anatase and rutile TiO_2 particles, as shown in Figure 4 [107]. Laser fluences of 10 mm above the focus, at the focus, and 5 mm below the focus (Figure 4(a), (b)) are 1.4, 80, and 0.2 J/cm^2, respectively, under which conditions the average sizes of particles are 12, 13, and 9 nm, respectively (Figure 4(c)-(e)). $TiO_{1.51}$ particles are generated in these three conditions but other products are different. A tightly focused laser at the highest fluence produces a high-temperature and high-pressure environment, enabling the generation of rutile TiO_2 (Figure 4(g)), which is the most thermodynamically stable phase normally formed at the temperature range of 600°C-1855°C. When the target is below the focus, plasma induces

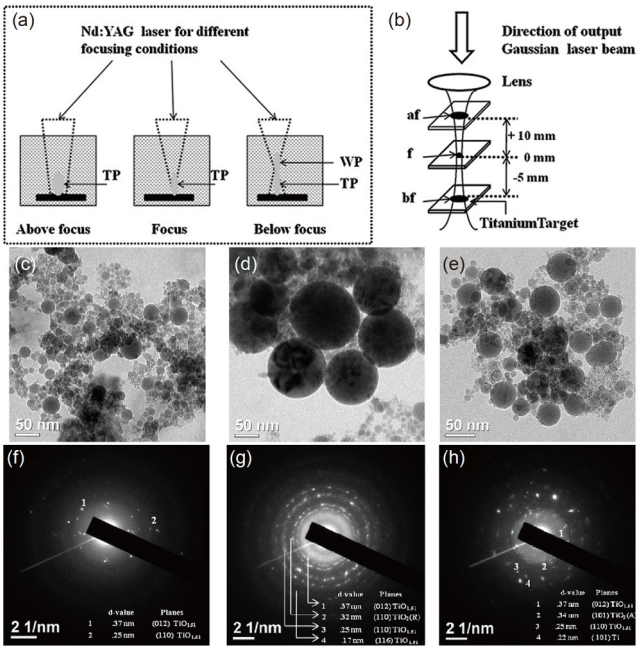

Figure 4 LAL-synthesized non-stoichiometric TiO_x particles. (a) Focus changing experimental set-up (WP: water plasma; TP: target plasma). (b) Laser spot variation due to focus change (af: above focus; f: focus; bf: below focus). TEM images (c)-(e) and SAED patterns (f)-(h) of NPs prepared above focus, focus, and below focus, respectively. (A: anatase; R: rutile), respectively. Copied from ref. [107] with permission.

the formation of a large number of cavitation bubbles filled with O_2 gases and water vapors, which facilitate the formation of anatase TiO_2 (Figure 4(h)). Under the above-focus condition, no extra O_2 gas is generated, and the products are pure $TiO_{1.5}$ particles without any rutile and anatase TiO_2 particles (Figure 4(f)). Although the above-focus condition significantly diminishes the effective energy used for LAL, it offers opportunities to synthesize nonstoichiometric TiO_x nanomaterials. LAL-synthesized nonstoichiometric TiO_x nanomaterials, such as anorthic Ti_8O_{15}, can be transformed into anatase and rutile phases by post-irradiation treatment at optimized periods of 10 and 20 min [125]. In other solutions such as supercritical CO_2, metastable phases (anatase-TiO_2, Ti_2O_3, and $TiO_{0.89}$) are producible (Figure 5(a)), whereas LAL in water under the same condition is only capable of producing rutile/brookite-TiO_2 (Figure 5(b)) [127]. This phenomenon indicates that different oxygen concentrations in the local environment originating from different solutions and dynamics (pressure and temperature) are critical for the generation of nonstoichiometric TiO_x nanomaterials, which are in high possibility to appear as byproducts together with dominant anatase/rutile-TiO_2 particles. In addition, Ti_2O_3 particles synthesized in supercritical CO_2 are well dispersed (Figure 5(c)), unlike those synthesized in water, which aggregate into web-like nanostructures (Figure 5(d)). This phenomenon is attributed to the non-polar and zero surface tension of supercritical CO_2 and the absence of hydrogen for

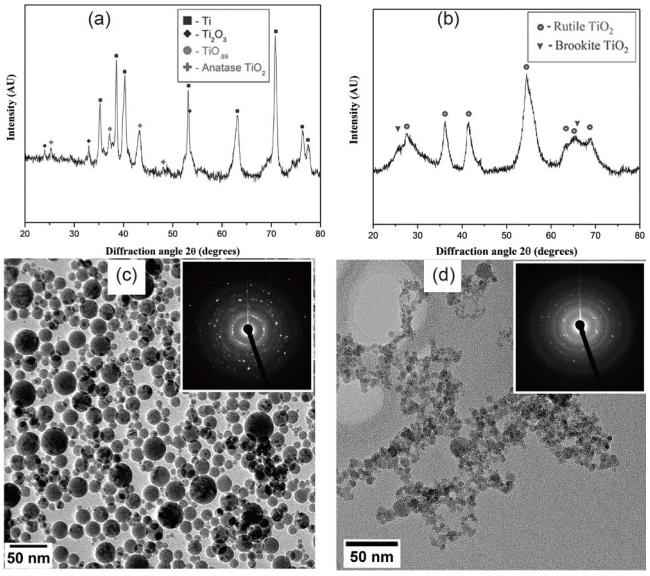

Figure 5 XRD pattern, TEM/SAED images of nanoparticles produced by LAL of Ti in supercritical CO_2 (a), (c) and H_2O (b), (d), respectively. Copied from ref. [127] with permission.

the formation of electrical double layers on the particles.

Aside from the influence of liquid composition on ablation dynamics, additives such as surfactants, polymers, salts, or colloids also affect colloidal phases [28]. For example, SDS molecules can decrease the surface/interface tension and increase solution viscosity and thermal conductivity, leading to the formation of long lifetime cavitation bubbles with high temperature and high pressure [128,129]. When the SDS concentration is around the critical micelle concentration (CMC, 8.6×10^{-3} mol/L [130]), finely crystalline anatase TiO_2 particles are achievable [106]. Other concentrations either less (0, 0.001 mol/L) or more (0.1 mol/L) than CMC only produce amorphous TiO_2 particles [106]. The formation of amorphous structures is associated with the strong thermal effect induced by the third harmonic laser (355 nm), which is often adopted for LML with a purpose for submicron spheres preparation [28,131,132]. Chaturvedi et al. [128] found that LAL of Ti in water can produce anatase TiO_2, independent of the ablation period, but LAL of Ti in an SDS aqueous solution (0.001 mol/L) yields a rutile phase when the ablation period is no more than 60 min. In analogy, rutile TiO_2 particles are produced in aqueous solutions containing polyvinylpyrrolidone (PVP) surfactants [108,109]. The ablation period should not be too long; otherwise, SDS will be completely consumed before ablation terminates, so other phases may be generated. For example, elongating the ablation period of LAL in SDS solutions to 90 min produces a mixture of anatase and rutile phases [128].

Oxygen vacancies can narrow the TiO_x bandgap to dramatically enhance light absorbance and photothermal conversion efficiency, making them suitable to be directly used as photocatalysts [133] and photothermal converters for enhanced solar water evaporation [134]. The existence of abundant oxygen vacancies also allows defect engineering through post treatments such as hydrothermal, heating, *in situ* reduction and ultraviolet (UV) irradiation, to build a bunch of composite catalysts (e.g., Ag/TiO_2 [113], Pt/TiO_2/rGO [43]) for photocatalytic and electrocatalytic applications, as reviewed in ref. [30]. Figure 6(a) displays the procedures of how to prepare Pt/TiO_2/rGO by *in situ* LAL in the presence of GO nanosheets, subsequent H_2PtCl_4 salt mixing, and *in situ* reduction of Pt NPs on TiO_2 NPs, which also leads to the reduction of GO into rGO. Figure 6(b), (c) display different magnifications of the resultant Pt/TiO_2/rGO composites, from which (004)/(111) lattice planes of anatase TiO_2 and Pt NPs are identifiable, respectively. Pt NPs decorated on TiO_2 particles are ultrasmall with an average size of (1.7±0.6) nm (Figure 6(d), (e)). Energy dispersive X-ray spectroscopy (EDS) mapping in Figure 6(f) indicates the uniform distribution of TiO_2 and Pt on rGO nanosheets. Such Pt/TiO_2/rGO ternary electrocatalysts display an excellent performance for methanol oxidation reaction with a mass activity of 698.9 mA/mg (Figure 6(g)), which is much better than those of Pt/SnO_2/rGO, Pt/C, and Pt/rGO catalysts [65]. Meanwhile, 81.4% of mass activity is still preserved after 1200 cycles, displaying excellent stability and robustness (Figure 6(g)). Ag/TiO composites synthesized by *in situ* LAL in $AgNO_3$ aqueous solutions are good multifunctional coating materials on polyvinylidenefluoride (PVDF) nanofibrous membranes to enhance antifouling and catalytic properties for oil-water separation [126]. Other applications such as antibacterial [105] and lithium-ion batteries [135] have also been investigated. The photocatalytic and antibacterial performances of LAL-synthesized amorphous TiO_2 particles (AVG ~50 nm) are superior to those of commercial TiO_2 particles [105]. LAL-synthesized TiO_2 particles are more effective in inhibiting gram-negative charged bacteria than gram-positive ones because of the electromagnetic attraction and TiO_2 particles, which can enhance the antibacterial effect of amoxicillin, a penicillin antibiotic [136]. In recent years, anatase-TiO_2/carbon quantum dots (CQDs) and Ag/TiO_2 composites have also been developed for sugar detection [137] and nonlinear optic [138] applications via LAL of Ti in a solution containing CQDs and $AgNO_3$ salt, respectively.

3.2 Mn

Mn is a highly reactive transition metal that can be transformed into a large variety of compounds with multiple valence states of +2, +3, +4, +5, and +6. LAL of Mn is primarily performed to synthesize different types of manganese oxide nanomaterials; it is sometimes employed to synthesize Mn-doped nanostructures, as shown in Table 3 [139-146]. LAL of Mn in water excels at the synthesis of

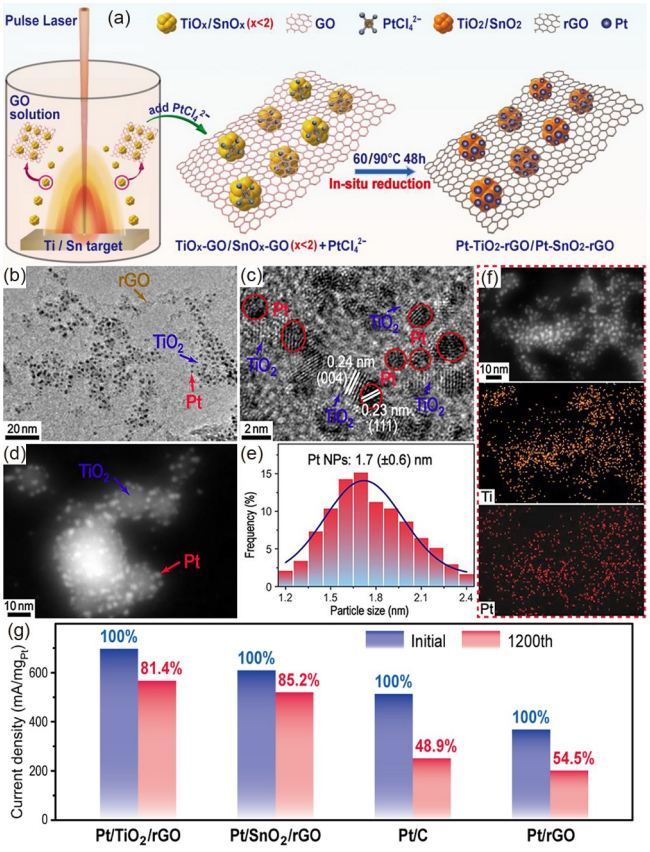

Figure 6 (Color online) Usage of LAL-TiO_x as both adsorbents and adsorbates for composite catalyst application. (a) Schematic illustration of the procedures for preparing Pt/TiO_2/rGO and Pt/SnO_2/rGO composites, including *in situ* LAL, addition of H_2PtCl_4 salt, and *in situ* reduction at 60°C/90°C for 48 h. (b), (c) TEM images, (d) high-angle annular dark field scanning transmission electron microscopy (HAADF-STEM) image, (e) Pt particle size distribution, and (f) STEM-EDS mapping of Pt/TiO_2/rGO composites. (g) Mass activity of different catalysts towards methanol oxidation reaction. Copied from ref. [43] with permission.

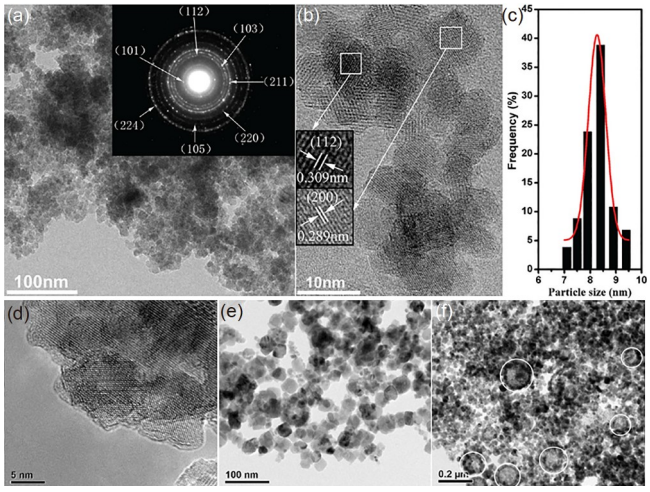

Figure 7 (Color online) LAL-synthesized Mn_3O_4 nanocrystals and their two-stage growth into nanocubes and hollow spheres. (a)-(c) TEM/SAED, HRTEM and particle size distribution histogram of LAL-synthesized Mn_3O_4 nanocrystals [147]. (d) Particle-attachment of Mn_3O_4 particles (8-11 nm) into nanocubes (20-30 nm) (e), and their further growth into bigger hollow spheres (90-170 nm) (f). Copied from ref. [139] with permission.

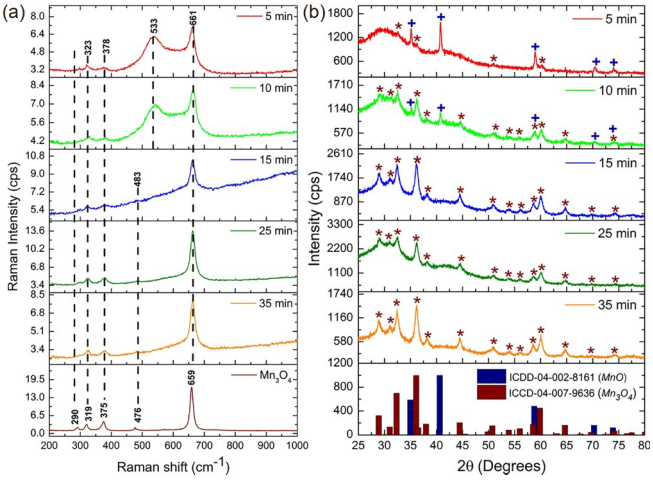

Figure 8 (Color online) LAL-period dependent phase evolution. (a), (b) Raman and XRD spectra of the colloids obtained by LAL of Mn in water for 5, 10, 15, 25, and 35 min. Featured Mn_3O_4 Raman spectrum and XRD pattern of MnO and Mn_3O_4 are included for comparison. Copied from ref. [142] with permission.

cubic Mn_3O_4 nanocrystals (Figure 7(a), (b)) with sizes dominant at 8-9 nm (Figure 7(c)), irrespective of pulse duration. When the concentration of Mn_3O_4 crystal is sufficiently high (achievable by ps-LAL at a high repetition rate of 100 kHz), the two stage growth of Mn_3O_4 crystals can be triggered (Figure 7(d)-(f)) [139]. Small Mn_3O_4 crystals (Figure 7(d)) first grow into nanocubes (Figure 7(e)), which can further evolve into large hollow spheres (Figure 7(f)). Another report showed that Mn_3O_4 may evolve from MnO, as illustrated in Figure 8. LAL, with an ablation period of no more than 15 min only produces a mixture of MnO and Mn_3O_4. MnO dominates the products after 5 min-LAL but becomes less in the case of 10 min-LAL (Figure 8(a), (b)). When the ablation period is no less than 15 min, pure Mn_3O_4 is produced (Figure 8) [142], which indicates that Mn_3O_4 may evolve from a phase transition of MnO through a completely progressive oxidation process. In general, seed growth based on the wet-chemical LaMer model can only proceed after the seed concentration is above the critical concentration but terminates when it drops below this value [34]. A long period of LAL assures both the concentrations of the smallest building blocks and their assembly structures to increase above the critical concentration values to trigger multi-growth [34], allowing the naked ligand-free particles to grow into novel structures. Aside from hollow spheres [139], LAL-synthesized Mn_3O_4 nanocrystals can also evolve into γ-MnOOH (the most stable polymorph of trivalent hydroxides) nanowires via a protonation process during colloid aging [140] and hydrothermal treatment [141]. Increasing the colloid temperature via thermal treatment accelerates the transition rate. The width of nanowires is larger than the size of Mn_3O_4 building nanocrystals, indicating that Oswald ri-

Table 3 Summary of the products obtained by LAL of Mn in different liquids, gas environments and post treatments using different laser parameters[a)]

Liquid	Laser	Atmosphere + post-treatment	Shape	Phase	Ref.
Water	10 ps, 1064 nm, 100 kHz, 80 μJ/pulse	air	cube → hollow	Mn_3O_4	[139]
Water	10 ns, 532 nm, 10 Hz, 700 mJ/pulse	air + aging	cube → nanowire	Mn_3O_4 → γ-MnOOH	[140]
Water	10 ns, 1064 nm, 60 mJ/pulse	air + hydrothermal	cube → nanowire	Mn_3O_4 → γ-MnOOH	[141]
Water	1064 nm, 15 Hz, 50 mJ/pulse	air	irregularly nonspherical shapes (AVG 9-11 nm)	MnO/Mn_3O_4 → Mn_3O_4	[142]
Ethanol	50 ps, 1064 nm, 2 Hz, 3 mJ/pulse	air + aging	spherical → triangular and square (6-50 nm → 7-14 nm)	Mn	[143]
$NiCl_2$ solution	10 ns, 1064 nm, 160 mJ/pulse	air	nanosheets	Mn-doped α-$Ni(OH)_2$	[144]
Water	1064 nm, 10 Hz, 20-50 mJ/pulse	air + aging	nanowire, cube, sphere, nanorods	MnO	[145]
Water	10 ns, 523 nm, 10 Hz, 70 mJ/pulse	air	polygonal (AVG 9 nm)	Mn_3O_4	[146]

a) BTC, benzene-1,3,5-tricarboxylic acid; MeOH, with methanol; DMF, dimethylformamide.

pening and orientated attachment growth mechanisms are involved in the morphology transition. Manganese oxides are magnetic; thus, the colloid tends to aggregate, making the particle size difficult to identify. Magnetic measurement, especially the blocking temperatures shown in the zero-field-cooled (ZFC) and field-cooled (FC) magnetization curves can give an indirect deduction of particle sizes through comparing with the counterparts synthesized by the wet-chemical method [147].

A long-period (e.g., 1 h) of ns-LAL can significantly increase the temperature of colloids and generate a large amount of Mn ions and hydroxyl ions, promoting the anisotropic growth of MnO particles into nanowires and nanorods [145]. In the presence of SDS, small MnO(OH) spherical particles with sizes of 10-20 nm are generated because of their different ablation dynamics as compared with that in water [148]. During colloid aging, particles first grow into large spheres and then transit into flower-like and microrod-like shapes with SDS as assembly linkers [148]. However, the reason why the MnO and MnO(OH) phases rather than the Mn_3O_4 phase are generated in these experiments remains unclear to date.

LAL-synthesized high-purity Mn_3O_4 particles of 9 nm in diameter are superior to commercial gadolinium (Gd)-based contrast agents for magnetic resonance imaging (MRI) [146]. The relaxivity of water protons for LAL-Mn_3O_4 NPs is 8.26 mM^{-1} s^{-1}, which is much higher than the 4.11 mM^{-1} s^{-1} of Gd agent because of the shorter distance between water protons and Mn ions of ligand-free Mn_3O_4 particles, thus enabling a clear *in vivo* imaging of organ tissues. High biocompatibilities *in vitro* and *in vivo* reported by the authors make LAL-Mn_3O_4 particles good substitutes for commercial Gd-based contrast agents for clinical MRI tests. However, another report showed that LAL-Mn_3O_4 NPs may induce subchronic toxicity in rats [149]. Hence, a comprehensive evaluation of their biocompatibility and toxicity for LAL-synthesized manganese oxide nanomaterials must be conducted before practical applications. Other than biological applications, nonlinear optical application [143] and the capacity for rapid removal of trace pentachlorophenol by physical adsorption [147] have also been demonstrated for LAL-synthesized Mn-based nanomaterials. However, these reports only indicate that these nanomaterials are suitable for these applications and fail to specify their advantages over their counterparts.

Mn-based colloids are good dopants for the growth of nonspherical nanomaterials to extend their application scope. For example, LAL of Mn in $NiCl_2$ (0.01 mol/L) aqueous solution produces Mn-doped $Ni(OH)_2$ nanostructures without any Mn-related phases [144], indicating the affinity of Ni^{2+} ions to OH^- ions for chemical reactions. As-prepared Mn-doped $Ni(OH)_2$ nanostructures for electrochemical supercapacitors exhibit an excellent cycling ability and a specific capacitance of ~1000 F/g under a current density of 5 A/g [144]. Hydrothermal treatment of LAL-MnO_x colloid and $FeCl_3 \cdot 6H_2O$ salt mixture can produce Mn-doped α-Fe_2O_3 polyhedral NPs, saucer-shaped, and hexagonal nanosheets, which are helpful to identify the facet-dependent adsorption ability toward Pb(II) and Cd(II) heavy-metal ions [150]. Figure 9(a)-(i) display the TEM images, size distributions, HADDF-STEM images, SAED patterns, and EDS analysis of Mn-doped α-Fe_2O_3 polyhedral NPs, saucer-shaped, and hexagonal nanosheets obtained using 3/10/12-min LAL-synthesized MnO_x colloids. The average sizes of polyhedral NPs, saucer-shaped, and hexagonal nanosheets are 30, 81, and 63 nm (inset images in Figure 9(a)-(c)), respectively. The dominated facets are isotropic for polyhedral NPs and {116} and {001} planes for saucer-shaped and hexagonal nanosheets, respectively (Figure 9(d)-(f)). The doping levels are 3%, 7%, and 11% (as confirmed by EDS analysis in Figure 9(g)-(i)), respectively. Square wave anodic stripping voltammetric tests show that the as-prepared nanostructures display different facet-dependent adsorption abilities toward Pb(II) and Cd(II) heavy-metal ions. Polyhedral NPs possess a weak adsorption capacity toward both Pb^{2+} and Cd^{2+} ions, whereas saucer-shaped and hexagonal

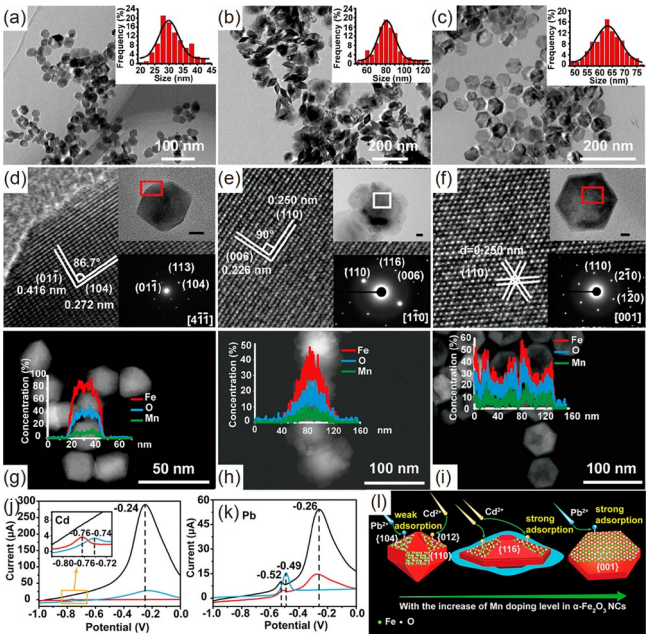

Figure 9 (Color online) Mn-doped α-Fe_2O_3 nanostructures obtained from hydrothermal of LAL-MnO_x colloid and $FeCl_3 \cdot 6H_2O$ salt. TEM images (a)-(c), HRTEM (d)-(f), and HAADF-STEM-EDS (g)-(i) analysis of the Mn-doped α-Fe_2O_3 nanostructures with shapes of polyhedral NPs, saucer-shaped nanosheets, and hexagonal nanosheets. Insets in (a)-(c) and (d)-(f) are nanostructure size distribution histograms and analyzed regions, respectively. The scale bar in the inset is 10 nm. (j)-(k) Typical SWASV responses of polyhedral (black lines), saucer-shaped (red lines), and hexagonal (blue lines) nanostructures, with a modified GCE for analysis of (j) 1.6 μmol/L Pb(II), (k) 2.0 μmol/L Cd(II). (l) Simulated crystal morphology of the Mn-doped α-Fe_2O_3 NCs and their ion adsorption ability. Copied from ref. [150] with permission.

nanosheets feature a highly selective adsorption toward Pb^{2+} and Cd^{2+} ions, respectively (Figure 9(j)-(l)). These facet-controllable nanostructures grown from LAL-MnO_x colloids are a good supplementary of wet-chemical synthesized nanostructures to shed light on facet-related properties, such as ion adsorption.

3.3 Fe

Fe is the fourth-most material in the earth's crust, after oxygen, silicon, and aluminum. Iron and its multiple compounds are widely applied in biomedicine [151], energy [152], and environmental remediation [153]. Aside from zero valence of Fe^0, Fe has various valences including Fe^{2+}, Fe^{3+}, Fe^{4+}, Fe^{5+}, and Fe^{6+}, with Fe^{2+} and Fe^{3+} forming most Fe-based compounds. The main products of LAL are amorphous Fe, α-Fe (ferrite), α-Fe_2O_3 (hematite), Fe_3O_4 (magnetite), γ-Fe_2O_3 (maghemite), Fe_3C (iron carbide), and FeO (wustite), as shown in Table 4 [154-170].

LAL of Fe in water generally yields complex products, such as Fe_3O_4/α-Fe_2O_3/γ-Fe_2O_3/FeO/Fe [159], α-Fe/FeO [161], and Fe/FeO/Fe_3O_4 [171]. In the presence of reductant $NaBH_4$, α-Fe particles are producible, whereas the addition of ascorbic acid enables the encapsulation of α-Fe particles by carbon, leading to the formation of α-Fe@C core-shell particles [170]. Carboxylate ions bonding via *in situ* LAL in citric acid solutions produces FeO_x colloids with hydrophilic surfaces [172], which may promote their biological applications through bioconjugation. LAL of Fe in PVP-containing aqueous solution producing pure FeO particles with their sizes adjustable from 45 to 5 nm by increasing PVP concentration from 0.01 to 0.2 mol/L [168].

Colloidal phases of LAL of Fe are highly sensitive to solution compositions. Figure 10(a)-(e) and (f)-(j) display the TEM morphologies and corresponding SAED patterns of the particles synthesized by LAL in water, methanol, ethanol, acetone, and toluene [173]. Besides an irregular amorphous Fe@C particle obtained in toluene (Figure 10(e) and (j)), products in other solvents are complex spherical particles containing at least three phases, as marked by different colors (Figure 10(a)-(d)) and confirmed by SAED analysis (Figure 10(f)-(i)). The carbon shell is composed of onion-like carbon and amorphous carbon (Figure 10(p), (q)) [154]. Amorphous Fe@C particles are formed by the ejection of molten Fe

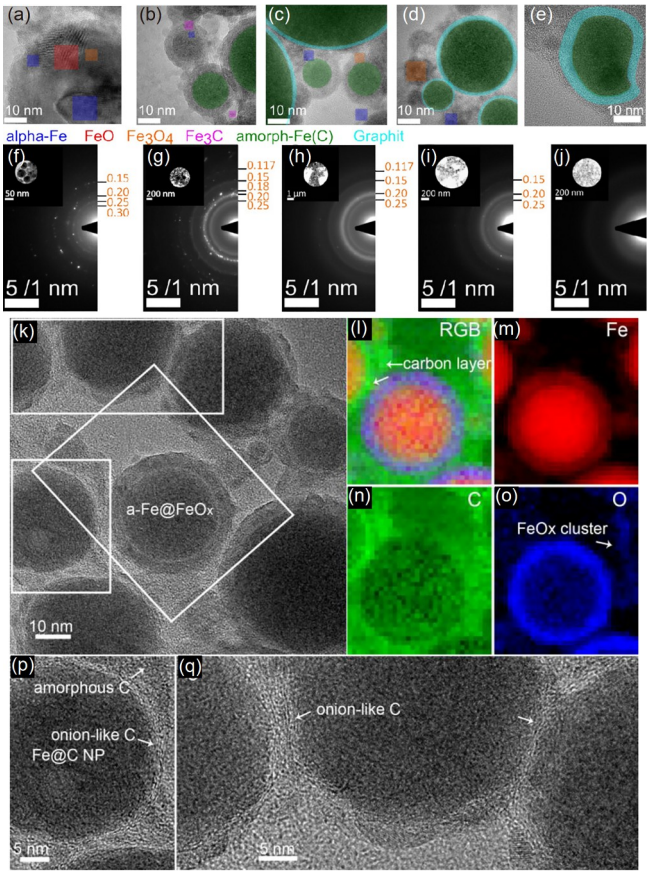

Figure 10 (Color online) (a)-(e) HRTEM images and (f)-(j) SAED analysis of colloids generated by LAL of Fe in (a) water, (b) methanol, (c) ethanol, (d) acetone, and (e) toluene. Copied from ref. [173] with permission. (k) TEM image and (l)-(o) EDX mapping of an Fe@FeO_x core-shell particle synthesized by LAL of Fe in acetone. (p), (q) TEM images of Fe@C particles. Copied from ref. [154] with permission.

Table 4 Summary of products obtained by LAL of Fe in different liquids, gas environments and post treatments using different laser parameters[a)]

Liquid	Laser	Atmosphere + post-treatment	Shape	Phase	Ref.
Acetone	457 fs, 1045 nm, 100 kHz, 6 μJ/pulse	air	core-shell (AVG 4-5 nm)	Fe@FeO_x, Fe@C and α-Fe_2O_3	[154]
Water	7 ns, 1064 nm, 20 Hz, 150 mJ/pulse	air	spherical (1-10 nm)	Fe, Fe_2O_3, Fe_3O_4	[155]
Water	5 ns, 532 nm, 20 Hz, 1900 J/cm^2	air	spherical	Fe, α-Fe_2O_3, Fe_3O_4	[156]
Acetone, water	250 fs, 527 nm, 10 Hz, 15 J/cm^2	air	spherical (bimodal 11/29 nm, 9/25 nm)	Fe/α-Fe_2O_3, FeO/Fe_3O_4	[157]
Ethanol	750 ps, 1064 nm, 10 Hz, ~13 J/cm^2	air	spherical (bimodal, 3 nm and 12 nm)	Fe_3C, Fe_3O_4	[158]
Ethanol	5 ns, 532 nm, 20 Hz, 1900 J/cm^2	air	core-shell (bimodal 17 nm, 24 nm)	Fe, Fe_2O_3	[156]
Water	7 ns, 1064 nm, 20 Hz, 150 mJ/pulse	air	spherical (2-80 nm)	Fe_3O_4, α-Fe_2O_3, γ-Fe_2O_3, FeO, and Fe	[159]
Water	240 ns, 1064 nm, 2 kHz, 3.5 mJ/pulse; 100 ns, 532 nm, 10 kHz, 8 mJ/pulse	air	spherical (AVG 7 nm and 17 nm)	Fe, FeO, Fe_3O_4	[160]
Water	532 nm, 10 Hz, 100 mJ/pulse	Ar	spherical (AVG 20 nm)	α-Fe, $Fe_{0.89}O$	[161]
Water	9 ns, 1064 nm, 10 Hz, 10 J/cm^2	air	spherical (AVG (10±6) nm)	Fe, FeO, α-Fe_2O_3, Fe_3O_4	[162]
$[P_{8888}]$HCOO and $[P_{8888}]$TFSI ionic liquids	(5±2) ns, 532 nm, 5 Hz, 20 mJ/pulse	1 Pa at 60°C	spherical (AVG (7.1±3.5) nm)	Fe	[163]
Liquid N_2	200/5 ns, 1064/532 nm, 1500/10 Hz, 3 mJ/pulse, 75 J/cm^2	N_2	spherical and acicular	Fe_4N, $Fe_{16}N_2$	[164]
Ethanol	10 ns, 532 nm, 5 Hz, 100 mJ/pulse	magnetic field	spherical which assembly into microfibers	Fe_3C and Fe_5C_2	[165]
DMSO	9 ns, 1064 nm, 10 Hz, 5 J/cm^2	air	spherical (AVG (4.7±2.3) nm)	Fe	[166]
Water + GO-PEG	7 ns, 1064 nm, 15 Hz, 200 mJ/pulse	air	spherical (AVG ~6 nm)	γ-Fe_2O_3	[167]
Water + PVP (0.01 to 0.2 M)	10 ns, 1064 nm, 10 Hz, 80 mJ/pulse	air	spherical (AVG 45-5 nm)	FeO	[168]
Methanol	15/25 ns, 532/248 nm, 20 Hz, 120 mJ/pulse	air, annealing	nanowires, nanosheets	α-FeO(OH) → α-Fe_2O_3	[169]
Methanol + $NaBH_4$ + ascorbic acid	7 ns, 1064 nm, 10 Hz, 90 mJ/pulse	air	core-shell	Fe@C	[170]
Water + $NaBH_4$	7 ns, 1064 nm, 10 Hz, 90 mJ/pulse	air	spherical	α-Fe	[170]
Water	7 ns, 1064 nm, 10 Hz, 90 mJ/pulse	air	spherical	Fe, Fe_2O_3	[170]

a) DMSO, dimethylsulfoxide; PEG, polyethylene glycol; PVP, Polyvinylpyrrolidone; GO, graphene oxide.

droplets from the ablated substrate followed by the carbon precipitation on their surfaces. Amorphous Fe@C particles are achievable by fs-LAL [154] and ns-LAL [174] in organic solvents. Apart from amorphous Fe@C core-shell particles [154,170,173], Fe@FeO_x core-shell particles are most frequently produced by LAL in organic solvents, as confirmed by EDS (Figure 10(l)-(o)) and HRTEM (Figure 10(k)) (white rectangle) [154]. Fe@FeO_x particles are formed by the incomplete oxidation of Fe particles, which indicates that oxidants are produced during LAL of organic solvents unless gas purging is used to remove all dissolved oxygen gases. Fe_7C_3@FeO_x core-shell particles and a mixture of Fe_3O_4 and Fe_3C particles are producible by ps-LAL in acetone [175] and ethanol [158], respectively. Currently, why carbon can turn out to be carbon shells or carbides in different cases remains unclear. When liquid nitrogen is used as LAL liquid, spherical and acicular iron nitride nanomaterials such as Fe_4N and $Fe_{16}N_2$ are produced via metal nitridation reactions [164].

In most cases, the colloids obtained from LAL of Fe in liquids are spherical. However, Luo et al. [176] demonstrated the feasibility of synthesizing spherical and hexagonal nanostructures with a pure magnetite phase by LAL in water with the aid of a vortex fluidic device (VFD), which enables LAL in confined and continuous modes (Figure 11(a)-(d)). All nanostructures are very small with most of them close to 20 nm (Figure 11(e), (f)). The pure magnetite phase is identified from SAED analysis (Figure 11(g)). Owing to the small sizes, the colloids collected inside and outside the tube display superparamagnetic properties (Figure 11(h), (i))

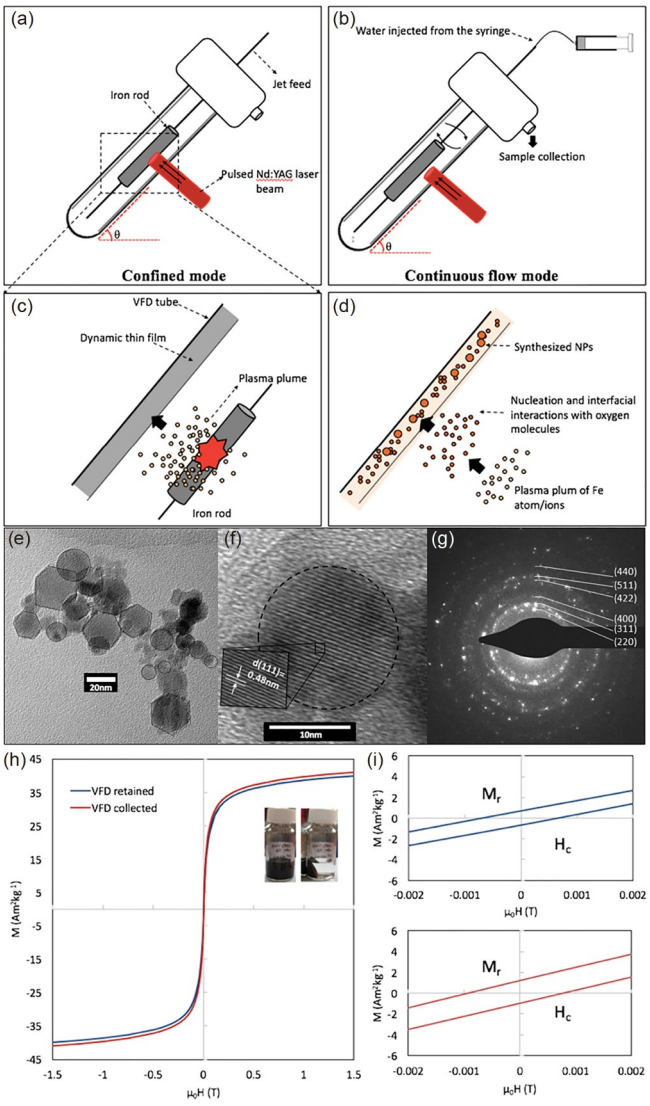

Figure 11 (Color online) (a)-(d) Schematic illustration of a vortex fluidic device (VFD) for LAL. (a) Confined mode LAL via lase irradiation on a static iron rod. (b) Laser beam irradiation of the device operated in continuous flow mode with an iron rod placed inside the VFD tube. (c) Plasma plume during the interaction of laser with iron rod. (d) Particle nucleation and formation scenario in the VFD device. (e)-(g) TEM, HRTEM, and SAED (magnetite) of Fe-colloid obtained by LAL at the flow mode with a rotational speed of 7500 r/min and a flow rate of 0.1 mL/min. (h) Magnetic hysteresis (*M-H*) curves of the colloids retained in the tube and collected outside the tube. (i) Low-field *M-H* curves for the two samples. Copied from ref. [176] with permission.

[177]. Henley et al. [169] reported the possibility to synthesize nonspherical nanostructures via LAL in methanol (laser wavelength of 248 nm, pulse duration of 25 nm). Increasing the pulse number from 6000 to 24000 shots causes the structure evolution from microbelts to nanowires, which is attributed to increased nuclei concentration, spontaneous self-assembly behavior, and photo-driven fragmentation of nanobelts. In other organic solvents such as ethanol and isopropanol, no 1D nanowire and 2D nanosheets are produced. Except for two reports [169,176] that demonstrated the feasibility to synthesize hexagonal nanostructures, spherical particles are commonly produced in batch, semi-batch and flow chambers, indicating the uniqueness of VFD for nanomaterial synthesis [178].

The blocking temperature (T_B) of LAL-synthesized iron oxide particles has been investigated as a good indicator of particle size. In general, the smaller the particle size, the lower the blocking temperature. According to the T_B values reported so far, the particle size follows the trend of fs-LAL (T_B=52 K, AVG 4-5 nm [154]) < ps-LAL (T_B=120 K, AVG 12 nm [158]) < ns-LAL (T_B=220 K, AVG 15 nm [179]). If aligned with the assistance of a magnetic field, the saturation magnetization can reach 261 emu/g at room temperature, exceeding that (212 emu/g) of bulky Fe [165]. The surface functionality of FeO_x particles by ligands makes them suitable for macrophage labeling and cell sorting/manipulation under a magnetic field [162]. Given their magnetism, LAL-synthesized iron oxide particles can also be used as antibacterial agents that can capture *Staphylococcus aureus* bacteria [180]. Richter et al. [181] reported that the synergistic effects of fibrin blending, LAL-Fe colloid embedment, serum protein coating can increase the endothelialization of alginate hydrogels because of the increased surface roughness, elastic modulus, and cellular adhesion. Successive LAL of Fe and Au allows the formation of Fe@Au core-shell particles ~64 nm in diameter [182]. Subsequent nanoformulation by curcumin (CU, antitumor drug) and folic acid (FA, target siting and enhancing cytotoxic effect of CU) makes Fe@Au composites suitable for cancer treatment, as evidenced by 85% apoptosis and decreased breast cancer viability (T-47D) and tumor size (*in vivo* measurement) overtime. Au coating on Fe is aimed to inhibit Fe oxidation and enhance the stability and dispersibility of Fe colloids.

Many studies focused on the catalytic applications of LAL-synthesized Fe-based products. For example, the mixture of FeO, Fe_3O_4, and Fe_2O_3 NPs synthesized by LAL in water can be integrated on TiO_2 nanotubes as adsorbents to enhance the photoelectrochemical performance of oxygen evolution reaction (OER) with the best 2.5 times as compared with pristine materials while bathing [183]. Zhang et al. [184] developed reduced graphene oxide (rGO)-supported Fe−N-doped carbon (Fe−N−C/rGO) catalysts by mixing LAL-FeO colloid with GO solution, adding pyrrole monomer and inducing polymerization and pyrolysis. Owing to synergistic effects, high specific surface area, fast mass transfer, and active site abundance, the oxygen reduction reaction (ORR) activities (characterized by onset potential and half-wave potential) of Fe−N−C/rGO catalysts are comparable to that of Pt/C catalysts in alkaline solutions, whereas their durability and tolerance against methanol crossover are superior to those of commercial Pt/C catalysts.

3.4 Co

Cobalt (Co) metal is a ductile and ferromagnetic metal that is stable at room temperature but becomes oxidized in air at temperatures above 300°C. Co is reactive during LAL and can be transformed into pure cobalt, cobalt oxide, cobalt hydroxide, cobalt nitride nanomaterials, and Metal Organic Framework (MOF) nanostructures by changing the liquid compositions and laser parameters, as shown in Table 5 [164,185-190]. In the presence of dissolved O_2 gases, LAL of Co in water produces CoO particles, which evolve into Co_3O_4 aggregates after 3-day aging in solution due to progressive oxidation [188]. The opposite transformation route from Co_3O_4 to defect-rich CoO particles can be realized via laser fragmentation, which is appealing for electrochemically catalytic applications such as OER [191,192]. In the absence of dissolved O_2 via N_2 purging, hexagonal β-$Co(OH)_2$ nanostructures are producible, which can completely evolve into Co_3O_4 after 3-day aging due to thermal decomposition and oxidation [188]. β-$Co(OH)_2$ nanostructures are positively charged, which can assemble onto negatively charged MoS_2 nanosheets via aging their mixed colloids at 70°C; during this process, β-$Co(OH)_2$ transits into Co_3O_4 particles with an average size of 5 nm [189]. In alkaline solutions at pH 13 and 14, Co_3O_4 nanorods can be produced, whose diameter increases with increasing pH [188]. Above the pH threshold of 12, such nonspherical nanostructures are merely achievable by 532 nm-LAL at low laser fluences less than 5 mJ/cm^2 but unachievable by 532 nm-LAL at high laser fluences or 1064 nm-LAL, in which cases spherical particles are produced, indicating the rigorous environment for the formation of Co_3O_4 nanorods.

Interestingly, LAL of bulk cobalt (hexagonal structure) in ethylene glycol (EG) produces hexagonal closely packed (hcp) α-Co and face-centered cubic (fcc) β-Co particles with an average size of 22 nm and surface plasmon resonance absorption peak at 510 nm [194]. The hcp α-Co and fcc β-Co are stable below and above the isomeric transformation temperature of ~427°C, respectively [195]. Retainment of the high-temperature phase of fcc β-Co after LAL quenching may be due to the annealing twinning of polycrystalline cobalt particles [196]. Regarding RLAL of Co, Co_3C@C core-shell NP chains have been produced by LAL in ethanol under a magnetic field, and the assembled ferromagnetic chains possess a magnetization of 232 emu/g, which is among the highest cobalt-based magnetic nanomaterials [190]. Zhang et al. [193] synthesized Co_3C@C core-shell particles by ns-LAL in acetone (Figure 12(a), (b)) and found that the carbon shells are onion-like with the thickest shell possessing 28 carbon layers (Figure 12(c)). Aside from onion-like carbon, amorphous carbon is also found among the particle aggregates (Figure 12(d)). Given the presence of carbon shells, other than the intrinsic superparamagnetic property from Co_3C cores, Co_3C@C particles also have excitation-wavelength-dependent PL originating from carbons [193]. In liquid nitrogen, nitridation can be triggered during LAL, resulting in the formation of Co_2N and Co_3N NPs [164].

With the precursor addition in the liquid and with the aid of a warm bath at 65°C for crystallization, LAL of Co in the mixed solution of 2-methylimidazole (Hmim) and KOH enables the formation of highly crystalline metal organic zeolitic imidazolate framework-67 (ZIF-67) structures with adjustable structural morphologies through changing the synthesis temperature and ablation duration [197]. To enrich the products, the authors added another salt of potassium tetra chloroplatinate(II) (K_2PtCl_4) in the solution for LAL and innovatively synthesized MOF-derived PtCo/Co_3O_4 nanocomposites in carbonaceous matrices, which display superior ORR performance, with their best 5-fold enhance-

Table 5 Summary of products obtained by LAL of Co in different liquids, gas environments and post treatments using different laser parameters

Liquid	Laser	Atmosphere + post-treatment	Shape	Phase	Ref.
Water	8 ns, 355 nm, 10 Hz, 30-210 mJ/pulse	air	spherical (1.4-4.5 nm)	Co_3O_4	[185]
Water, ethanol	1064 nm, 10 Hz, 30/40/50/60 mJ/pulse	air	spherical (AVG 5-15 nm, 20-40 nm)	Co_3O_4/CoO, Co	[186]
Mixed $Na_2S_2O_3$ and $Ni(NO_3)_2$ aqueous solution	10 ns, 1064 nm, 130 mJ/pulse	aging, annealing	nanosheet network	Co-doped $Ni(OH)_2$	[187]
Water	4 ns, 1064/532 nm, 10 Hz, 330/165 mJ/pulse	O_2/N_2, + ultrasonication + aging	sphere, hexagonal sheets	CoO → Co_3O_4, β-$Co(OH)_2$ → Co_3O_4	[188]
Water + KOH (pH 13, 14)	4 ns, 532 nm, 10 Hz, 1 J/cm^2	O_2/N_2 + ultrasonication + oxidation	nanorods	Co_3O_4	[188]
Water	6 ns, 1064 nm, 10 Hz, 150 mJ/pulse	air + mixed with MoS_2 solution and aging	spherical	β-$Co(OH)_2$, Co_3O_4 → Co_3O_4	[189]
Ethanol	10 ns, 532 nm, 10 Hz, 60 mJ/pulse	magnetic field	nanochains consisted of spheres (AVG 200-300 nm)	Co_3C	[190]
Liquid N_2	200/5 ns, 1064/532 nm, 1500/10 Hz, 3 mJ/pulse, 75 J/cm^2	N_2	spherical	Co_2N and Co_3N	[164]

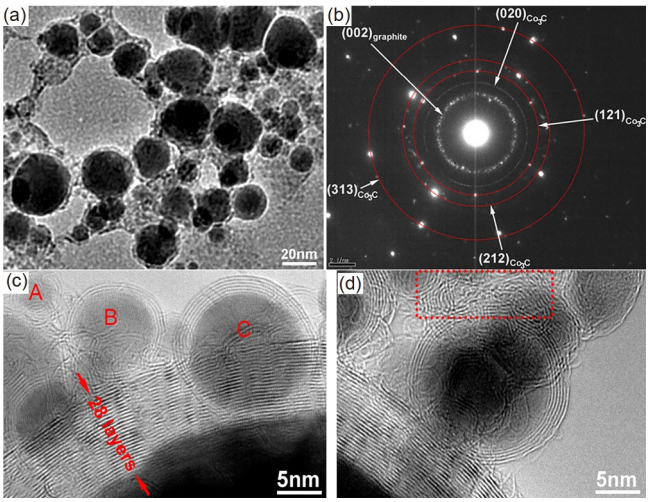

Figure 12 (Color online) (a) TEM image, (b) SAED, (c), (d) HRTEM images of Co_3C/OLC (onion-like carbon) NPs prepared by ns-LAL of Co in acetone. Copied from ref. [193] with permission.

ment in specific mass activities compared with commercial Pt catalysts [198].

The applications of Co particles synthesized by LAL are mainly within the scope of nonlinear optics and catalysis. Co-based particles synthesized in chloroform ($CHCl_3$) and chlorobenzene (C_6H_5Cl) are more suitable than colloids synthesized in carbon tetrachloride (CCl_4), benzene (C_6H_6), toluene ($C_6H_5CH_3$), ethanol (C_2H_5OH), and water for optical limiting applications because of their excellent two-photon absorption and nonlinear scattering [199]. Co-based particles synthesized by LAL in toluene are better candidates for optical limiting than fullerene C_{60} because of their nonlinear absorption, nonlinear scattering, and thermal nonlinear refraction properties [200]. Regarding the catalytic applications, Blakemore et al. [185] reported the extraordinary water oxidation performance of LAL-synthesized surfactant-free ultrasmall (<5 nm) Co_3O_4 NPs. LAL-synthesized Co@C core-shell particles can be embedded onto graphenes to be transformed into graphene-supported Co-based NPs encapsulated in nitrogen-doped graphitic layers (Co@NC/rGO) via hydrothermal treatment followed by pyrosis in N_2 environment [201]. Graphene-supported Co-based NPs are excellent catalysts for ORR (onset potential of 0.98 V, half-wave potential of 0.86 V in alkaline media) and are comparable to commercial Pt/C catalysts [201]. With the aid of a mixed aqueous solution containing 0.1 mol/L $Na_2S_2O_3$ and 0.02 mol/L $Ni(NO_3)_2$, ns-LAL of Co can produce Co-doped $Ni(OH)_2$ flower-like structures consisting of nanosheet networks [187]. Such hierarchical structures can be applied as pseudocapacitors, showing a specific capacitance of 1421 F/g at 6 A/g and 76% retention after 1000 cycles in 1 mol/L KOH aqueous solution. Subsequent annealing treatment can make them transform into Co-doped NiO nanosheets with a good heritage of structural morphology, which can significantly enhance the retention level to 92% with a compromise of specific capacitance down to 720 F/g [187]. This work shows that ablated Co colloids can be used as dopants to develop doped mesoporous metal oxides and hydroxides for applications such as catalysis in need of the high surface area.

3.5 Ni

Similar to Fe and Co, LAL also enables Ni to be transformed into different compounds with the main phases of metals, oxides, and nitrides, as shown in Table 6 [74,164,202-212]. In aqueous solutions, the main product is the NiO and Ni mixture because of the incomplete oxidation rate [207]. Through a theoretical calculation of the optical extinction spectroscopic features, Muñetón Arboleda et al. [203] reported the possibility to synthesize hollow nickel particles, Ni@NiO and NiO@Ni core-shell particles by LAL in water. In the presence of SDS surfactants to induce anisotropic growth, cubic [212] and dumbbell-shaped [213] NiO nanostructures can be produced. Hollow spherical Ni particles have also been synthesized in water [214] and acetone [32] through the generation of bubbles and the magnetic properties of small clusters to aggregate on the bubble interfaces. With respect to LAL-synthesized large Ni-based spherical particles with sizes of hundreds of nm, particle surface roughness can be either smooth or rugged (Figure 13(a)-(d)), which indicates their different formation/growth dynamics in different solutions [215]. Different solutions also alter LAL

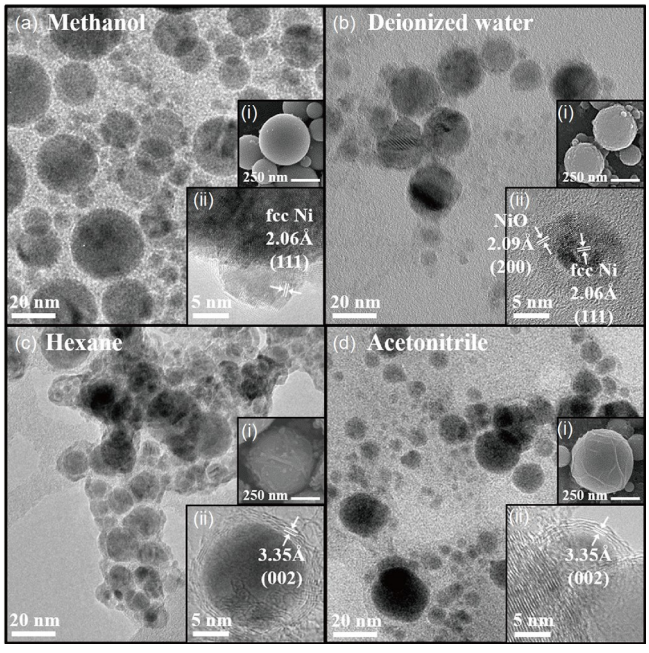

Figure 13 (a)-(d) TEM images of Ni-based NPs prepared by LAL in methanol, water, hexane, and acetonitrile, respectively. Insets: (i) SEM and (ii) HRTEM images of the corresponding samples. Copied from ref. [215] with permission.

Table 6 Summary of products obtained by LAL of Ni in different liquids, gas environments and post treatments using different laser parameters[a)]

Liquid	Laser	Atmosphere + post-treatment	Shape	Phase	Ref.
TEOS	240 s, 1064 nm, 10 Hz, 1000 mJ/pulse	air	spherical (20-80 nm)	Si-overdoped $Ni_{1-x}O$	[202]
n-Heptane	120 fs, 800 nm, 1 kHz, 100 μJ/pulse	air	spherical, hollow (bimodal, 2.5 and 7 nm by AFM)	Ni	[203]
Acetone	457 fs, 1045 nm, 100 kHz, 6 μJ/pulse	air	spherical, hollow (AVG 4.3 nm)	–	[204]
Methanol	7 ns, 1064 nm, 10 Hz, 80 mJ/pulse	air, laser irradiation	spherical (8.68 → 7.16 nm)	fcc Ni	[205]
Water	10 ns, 337 nm, 5 Hz, 50 J/cm^2	air	spherical (bimodal, peaks at 6/100 nm)	Ni@NiO	[206]
Water	7 ns, 1064 nm, 10 Hz, 80 mJ/pulse	air, laser irradiation	core-shell	Ni, NiO	[205]
Hexane	7 ns, 1064 nm, 10 Hz, 80 mJ/pulse	air, laser irradiation	spherical (7.08 nm → 6.62 nm)	fcc-/hcp-Ni → fcc-Ni	[205]
Acetonitrile	7 ns, 1064 nm, 10 Hz, 80 mJ/pulse	air, laser irradiation	spherical (6.32 nm → 5.32 nm)	fcc-/hcp-Ni → hcp-Ni	[205]
Water, ethanol	15 ns, 1064/532/355 nm, 10 Hz, 2.9-5.6 J/cm^2	air, magnetic field	spherical (4.9 in ethanol, 6.3/4/3 in water)	Ni, NiO	[207]
Water	120 fs, 800 nm, 1 kHz, 100 μJ/pulse	air	spherical (bimodal: 7.8/20.6 nm)	Ni, NiO	[203]
Water + SDS	3-6 ns, 532 nm, 10 Hz, 3.2/10.5/19.9 J/cm^2	air	spherical (1.8, 2.9, 10.8 nm)	NiO	[208]
Water	7 ns, 1064 nm, 10 Hz, 50-150 mJ/pulse	air	sphere (35, 47, 61 nm)	NiO	[209]
Water + GO	10 ns, 1064 nm, 60 mJ/pulse	air, addition of hydrazine hydrate and aging for 20 h	spherical (2.3 nm)	NiO_x → Ni	[210]
Water	1 ms, 1064 nm, 20 Hz, 10^6 W/cm^2	air	cube	NiO	[74]
Liquid N_2	200/5 ns, 1064/532 nm, 1500/10 Hz, 3 mJ/pulse, 75 J/cm^2	N_2	spherical	Ni_4N, Ni_8N	[164]
Liquid CO_2	8 ns, 1064 nm, 10 Hz, 2.64 mJ/pulse	17°C, 5.2 MPa	core-shell (5-350 nm)	NiO_x@C	[211]
Water + SDS (0.1, 0.01, 0.001 mol/L)	1070 nm, continuous, ~250 W	air	spherical, cube (AVG 10-13 nm)	NiO	[212]

a) TEOS, tetraethyl orthosilicate.

productivities and Ni/NiO particle sizes, both of which affect their magnetic-field-assisted assembly capacities into different lengths of 1D microstructures [207]. Regarding RLAL of Ni, Ni_4N and Ni_8N particles form in liquid N_2 [164], whereas Ni/Ni_3C@C particles are produced in acetone [101]. When the carbon-encapsulated particles are less than 200 nm, the number of carbon shells increases almost linearly with the particle size [215]. The carbon shell thickness reaches a plateau when the Ni particles are in the range of 200-500 nm [215]. Benefiting from solvent decomposition and *in situ* doping during particle nucleation/growth, Si-overdoped $Ni_{1-x}O$ nanocondensates/particulates with novel superstructures have been synthesized by LAL of Ni in TEOS [202]. In the liquid CO_2, the resultant particles of LAL are composed of 99% C without nickel, which suggests that Ni is a good catalyst for the formation of carbon spheres by LAL [211]. However, what becomes from the ablated Ni materials remains unclear.

Ni crystal structures can be divided into three types: fcc, body-centered cubic (bcc), and hcp, with fcc being the most thermodynamically stable and bcc and hcp structures as metastable phases [205]. Solvent-dependent production of fcc and hcp-Ni using two steps of LAL is shown in Figure 14(a)-(f) [205]. The first (primary) step is LAL of Ni. The second step is LAL of the colloids synthesized by the first-step LAL. Figure 14(a)-(d) display the particle morphologies after the first and secondary LAL in methanol and acetonitrile and their corresponding size histograms. Primary LAL of Ni in water, methanol, hexane, and acetonitrile produces fcc-Ni/NiO, fcc-Ni, fcc-/hcp-Ni, and fcc-/hcp-Ni particles, respectively (Figure 14(e)). After secondary LAL, the product phases in water, methanol, and hexane remain the same, whereas the colloid in acetonitrile transforms into pure hcp-Ni particles (Figure 14(f)). Regardless of the solvent used, the particle size diminishes after the secondary LAL, about 1-2 nm downsize, thereby triggering fragmentation and the high-pressure impact of the colloids. Hence, the solvent should significantly influence the plasma phase that governs the nucleation of particles to induce the formation of different phases. The initial colloid particles are very small and difficult to further be decreased. If much larger particles are treated for secondary LAL, the difference in particle size

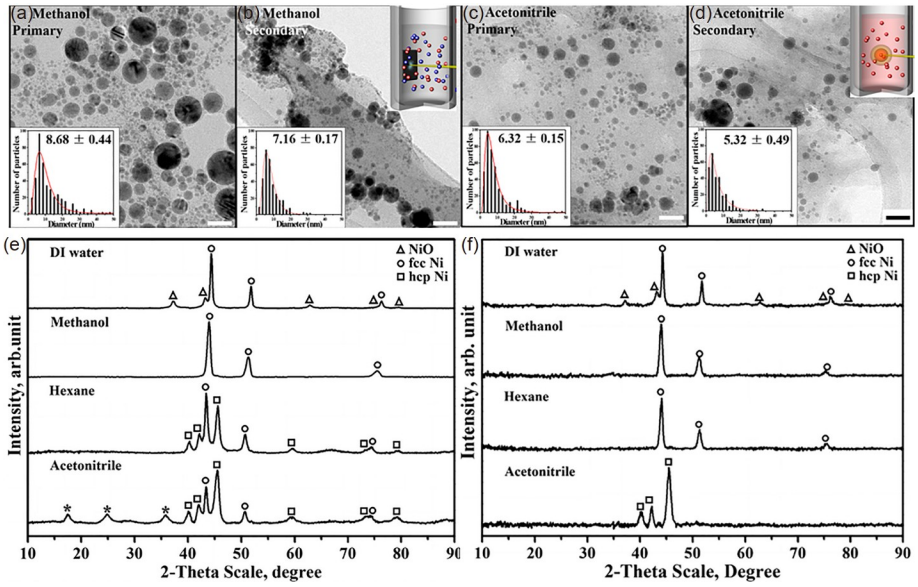

Figure 14 (Color online) TEM images of the primary (a), (c) and secondary ablated (b), (d) Ni nanoparticles in methanol (a), (b) and acetonitrile (c), (d) (scale bar = 40 nm) and corresponding size distribution histograms. XRD patterns of NPs synthesized by primary and secondary LAL in water, methanol, hexane, acetonitrile with fcc Ni, hcp Ni and NiO marked by circles, squares, and triangles. Copied from ref. [205] with permission.

between the first and secondary LAL should be in great discrepant. This work, to some extent, is similar to the result of LAL of Co [194], but it is another milestone by showing the possibility to produce pure metastable Ni phase colloids rather than mixed phases.

LAL-synthesized Ni-based particles can be directly used as catalysts [216] or as adsorbents on support materials to build composite catalysts. The latter is a popular strategy to develop excellent composite catalysts. LAL of Ni in GO-containing solution followed by N_2H_4 reduction yields fine Ni/rGO composites [210]. Electrostatic adsorption of positively charged NiO_x particles ensures fine anchoring of NiO_x on GO sheets. NiO particles and Ni@NiO core-shell particles are both identified from HRTEM analysis of the crystal planes. After reduction, the NiO phase transforms into Ni and the particles located on rGO sheets are as small as 2-3 nm. The as-prepared Ni/rGO composites are so far the best Ni-based catalysts for methanol oxidation reaction (MOR) at a methanol concentration of 4 mol/L, with a higher catalytic activity of 1600 mA/mg and higher stability (63.75% remaining after 1000 cycles) [210] than commercial Pt/C composites. Size-dependent antibacterial performance has been confirmed for LAL-NiO particles: the smaller the particle size, the higher antibacterial performance they possess [209]. In addition, it is found that NiO particles are more effective against gram-negative bacteria (i.e., *Escherichia coli* and *Candida albicans*) than gram-positive bacteria (i.e., *Streptococcus aureus* and *Bacillus subtilis*) [209]. However, NiO compounds are commonly toxic, and thus they should be carefully evaluated before biomedical applications.

3.6 Cu

The interest in LAL of Cu lies in the production of multiple shapes of Cu-related nanostructures and corresponding mechanisms, as shown in Table 7 [74,101,217-229]. To understand how morphologies and phases change with liquids for LAL of pure Cu, Begildayeva et al. [220,230] performed a series of experiments using ten solvents and their results are shown in Figures 15 and 16. Figure 15(a)-(h) and (i) show the SEM images and XRD spectra of the nanomaterials obtained by LAL of Cu in water, methanol, ethanol, 1-propanol, butanol, EG, hexane, and acetonitrile under the same conditions [220]. Water induces the formation of Cu@Cu_2O core-shell particles upon LAL (Figure 15(a), (i), (j)), whereas organic solvents such as ethanol (Figure 15(c)), 1-propanol (Figure 15(d)), butanol (Figure 15(e)), EG (Figure 15(f)), and hexane (Figure 15(g)) produce Cu@C core-shell particles [220]. Rod-like CuO nanostructures 400-500 nm in length and 30-50 nm in thickness are produced in methanol (Figure 15(b), (i)), which may benefit from the generation of copper(II) hydroxide ($Cu(OH)_2$) intermediates through the interaction between Cu^{2+} ions and OH groups coming from LAL-induced methanol decomposition [220]. Such speculation is in accordance with the report by Goncharova et al. [231] who found that CuO nanofibers can be produced in H_2O_2 and NaOH with rich OH radicals. During methanol decomposition, OH groups are released due to C–O bond breaking, whereas C–C rather than C–O dissociates during LAL in ethanol, 1-propanol, and butanol because of the lower binding energy of C–C bond than C–O bond. In consequence, oxidation occurs in methanol, whereas carboni-

Table 7 Summary of products obtained by LAL of Cu in different liquids, gas environments and post treatments using different laser parameters

Liquid	Laser	Atmosphere	Shape	Phase	Ref.
Methanol, 2-propanol	7 ns, 532 nm, 10 Hz, 10 J/cm^2, 15/30/60 min	air	spherical (7/15/19 nm in methanol, 9/12/17 in 2-propanol)	Cu, CuO, Cu_2O	[217]
Methanol	1064 nm, 10 Hz, 0.1 J/pulse, 12.7 J/cm^2	Ar	spherical (bimodal: 21/55 nm)	Cu	[218]
Water, methyl alcohol	14 ns, 532 nm, 20 kHz, 0.26 mJ/pulse; 1064 nm, 0.8 ns, 200 kHz, 0.03 mJ/pulse	air	spherical (3-9 nm)	Cu, Cu_2O, CuO	[219]
Methanol	7 ns, 1064 nm, 0.08 J/pulse	air	rod-like	CuO	[220]
Acetonitrile	7 ns, 1064 nm, 0.08 J/pulse	air	microcube and spherical	CuCN, Cu@C	[220]
Dimethyl sulfoxide (DMSO)	7 ns, 1064 nm, 10 Hz, 0.5, 2, 3.5, 5 J/cm^2	air	spherical (AVG 17-75 nm)	CuS	[221]
1-Dodecanethiol	1 ms, 1064 nm, 20 Hz, 10^6 W/cm^2	air	nanowires	CuS	[74]
Ethanol, 1-propanol, butanol, ethylene glycol, hexane	7 ns, 1064 nm, 0.08 J/pulse	air	spherical	Cu	[220]
Acetone	40 ns, 1064 nm, 5 kHz, 5.5 mJ/pulse	air	spherical (~3 nm)	Cu	[222]
Acetone	7 ns, 1064 nm, 100 mJ/pulse	air	spherical (17.1 nm)	Cu	[101]
Water-alcohol	7 ns, 1064 nm, 20 Hz, 150 mJ/pulse	air + aging	spherical (10-40 nm) → anisotropic (100-500 nm long and 100-400 nm wide), lenticular-like (150-550 nm)	Cu, Cu_2O → CuO	[223]
Water	10 ns, 1064 nm, 10 Hz, 100 mJ/pulse	air	nanowire (15-30 nm wide, 200-600 nm long)	Cu, Cu_2O	[224]
Water	7 ns, 532 nm, 10 Hz, 30/50/70 mJ/pulse	air	spherical (AVG 7-20 nm)	Cu, Cu_xO	[225]
Water	6 ns, 532 nm, 1 Hz, 184-210 mJ/pulse	air	rugged structures (1-9 μm)	Cu_4O_3	[226]
Water	40 ns, 1064 nm, 5 kHz, 5.5 mJ/pulse	air	needle-like	Cu, Cu_2O, CuO	[222]
Water	40 ns, 1064 nm, 5 kHz, 5.5 mJ/pulse	argon	rectangle-like	Cu, Cu_2O	[222]
Water	5 ns, 1064/355 nm, 10 Hz, 54 mJ/pulse; 800 nm, 200 ps, 1 kHz, 0.56 mJ/pulse; 800 nm, 30 fs, 1 kHz, 0.56 mJ/pulse	air	spindle-like	CuO, Cu_2O	[227]
Water	10 ns, 532 nm, 5 Hz, 100 mJ/pulse	air, electrical field	spindle-like	CuO	[228]
Water + 0.01/0.02 mol/L PVP	8 ns, 1064 nm, 10 Hz, 50 mJ/pulse	air	core-shell, spherical (AVG 13, 5, 4 nm)	Cu@Cu_2O, Cu	[229]

zation occurs in ethanol, 1-propanol, and butanol. Large microcubes are produced in acetonitrile because of the formation of Cu(I) cyanide (CuCN) [220,230], as shown in Figure 16(a). Similarly, CN^- bond dissociates from acetonitrile during LAL because of the cleavage of C–C (Figure 16(b)) (binding energies of C–C and C≡N are 530.78 and 1167.64 kJ/mol), which interact with Cu-ions to form cubic CuCN structures. By contrast, free carbon atoms are generated from propionitrile and butyronitrile solvents, which aggregate on the Cu particles, leading to the formation of Cu@C particles [220].

In water, the dominant products are the mixture of Cu and Cu_xO (Cu_2O and CuO) or the mixture of CuO and Cu_2O, as shown in Table 7. When using argon gas to inhibit oxidation rate by removing the dissolved oxygen, rectangle-like nanostructures consisting of Cu and Cu_2O phases are attainable by LAL of Cu in water [222]. Need-like nanostructures composed of Cu, Cu_2O, and CuO are producible by LAL in the air while keeping other processing conditions constant [222]. Thus, rectangle-like structures are preferable to be generated under OH^- concentrations lower than those required for needle-like structure formation, which is in accordance with the trend of CuO synthesized by the wet-chemical method [232] in need of thermal treatment at 80°C for a certain period. Hence, it is estimated that LAL of Cu for nonspherical nanostructures production is a wet chemical process with *in situ* hot-water thermal treatment. This finding is in line with the fact that most nonspherical Cu/CuO_x nanostructures are generated by ns-LAL, during which the thermal effect dominates. At a very high fluence of 80 J/cm^2,

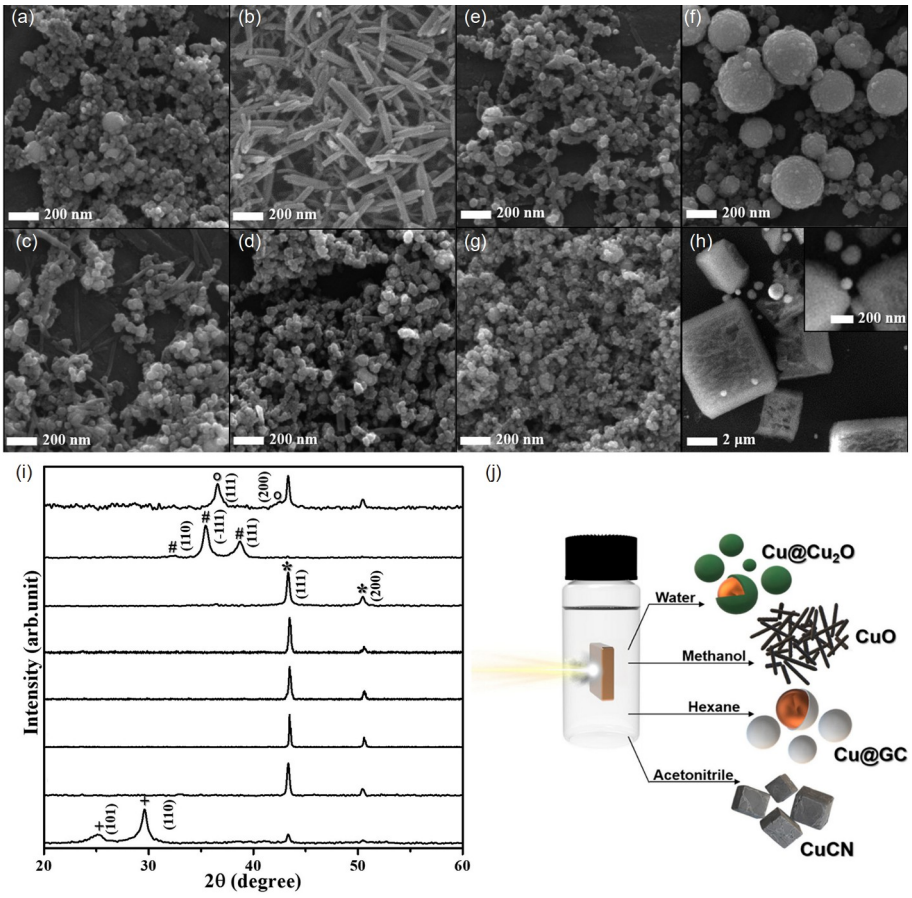

Figure 15 (Color online) Solvent-dependent Cu-based nanomaterials prepared by LAL. SEM images of nanomaterials produced by LAL of Cu in (a) water, (b) methanol, (c) ethanol, (d) 1-propanol, (e) butanol, (f) ethylene glycol, (g) hexane, and (h) acetonitrile, respectively. The inset image in (h) indicates the formation of spherical NPs and microcubes. (i) XRD patterns of as-prepared nanomaterials in the abovementioned solvents. Featured patterns of Cu NPs (JCPDS #01-085-1326) are denoted as *, Cu_2O (JCPDS #01-077-0199) and CuO (JCPDS # 00-048-1548) are marked as ° and #, respectively, while peaks of CuCN (JCPDS #96-110-1019) are indicated by +. (j) Schematic illustration of the products produced by LAL of Cu in different solvents. Copied from ref. [220] with permission.

a large amount of H_2 gases are generated, enabling the formation of hollow CuO_x structures [233]. Fs laser ablation is a "cold" process because of the insufficient electron-phonon relaxation [234], which can significantly inhibit the thermal effect. Picosecond (ps) laser ablation generally induces a gentle thermal effect between ns laser and fs laser. Hence, the growth rate should follow the sequence of ns-LAL > ps-LAL > fs-LAL if the seed difference caused by different laser systems is neglected. This finding has been verified by CuO/Cu_2O spindle-like structures produced via ns/ps/fs-LAL of Cu in water [227].

Aging LAL-synthesized CuO_x colloids often induce structural evolution into spindle/bundle-like structures [72,231,235], accompanied by the phase change from Cu_2O to CuO through a completely progressive oxidation process. Owing to good electrical conductivity and adsorption capacity, they can be used to construct gas sensors for ppm-level ethanol gas detection [235]. The thermal conductivity of EG solvent can be enhanced ~24% by introducing Cu@C colloids after 30 min-LAL of Cu [236], making the colloid suitable as nanofluids. CuO_x/GO composites synthesized by *in situ* LAL can be transformed into high-performance Cu/rGO composite catalysts via $NaBH_4$ reduction [237]. LAL-synthesized Cu NPs, either in the form of Cu@C or CuNPs@polymer composite, are good antibacterial agents against Gram-negative *Pseudomonas* spp. bacteria, making them appropriate for food packages [238,239] or food preservation [240]. Once LAL-synthesized CuO NPs are conjugated on GO nanosheets, the antibacterial performance of GO nanosheets toward *E. coli* bacterial can be further enhanced [241], indicating the efficacy of CuO NPs for antibacterial applications. LAL-Cu colloid also exerts an antibacterial effect on textile, such as cotton fabric [242].

3.7 Zn

Zn metal, upon LAL treatment, most frequently transforms into ZnO_2 [243], Zn@ZnO [244], or ZnO [245-247] nanomaterials. Water is the dominant oxidant for LAL-induced Zn oxidation. Soliman et al. [248] showed the feasibility of

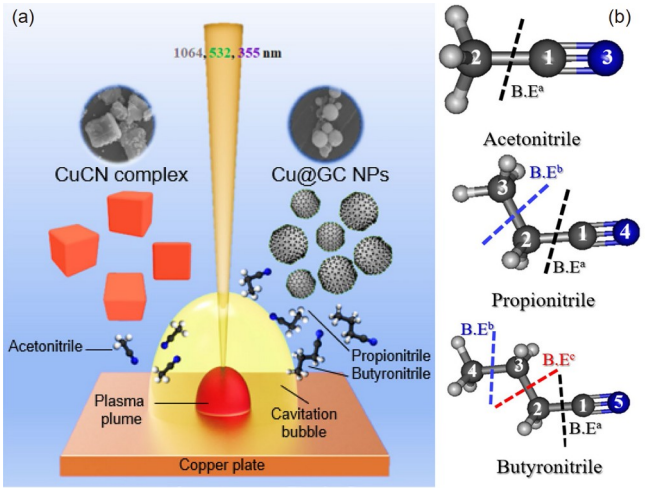

Figure 16 (Color online) (a) LAL of Cu in nitrile solvents (acetonitrile, propionitrile, or butyronitrile) at laser wavelengths of 1064, 532, and 355 nm with cubic CuCN and spherical Cu@GC (GC, graphene carbon) as products. (b) Separated bonds for different organic nitrile solvents because of different binding energy (BE) in different positions. Copied from ref. [230] with permission.

altering morphology, crystallinity, and size of ZnO using 30 MPa pressurized water. During LAL, Zn particles first undergo fast defect-free oxidation in the plasma phase and then experience slow defect-endowment oxidation through water diffusion in the liquid phase [249]. Taking advantage of X-ray spectroscopy, Reich et al. [250] quantified Zn-to-ZnO transition within the initial 10 min period and revealed the subsequently slower reaction route into hydrozincite. The plasmonic peak of Zn and defect/exciton emission of ZnO can be used as indicators for the formation of Zn and ZnO phases, respectively [249]. At extreme conditions induced by high-power LAL of Zn in water (e.g., 1.7×10^{11} W/cm^2 at λ=1064 nm and 8.3×10^{10} W/cm^2 at λ=532 nm excitation), the high-pressure phase of W-ZnO and ε-$Zn(OH)_2$ composite nanocondensates is producible [251]. Summary of products obtained by LAL of Zn is shown in Table 8 [71,72,101,243,251-267].

Ishikawa et al. [254] reported that the growth of ZnO particles into columnar structures starts at temperatures higher than 60°C and becomes finely crystalized at 80°C. Aging the synthesized particles by LAL of Zn in water leads to the shape transition into larger cubic and polyhedral structures, irrespective of the sizes of initial particles but dependent on the pulse durations of laser systems and correspondingly different thermal effects [71]. Columnar ZnO structures form via surfactant adsorption, such as lauryl dimethylaminoacetic acid (LDA), an amphoteric surfactant with an anionic part at the end. Adding SDS surfactant, a template that facilitates the formation of lamellar nanostructure [268] in the ethanol-water mixture at a volume ratio of 1:4 produces nanolayer self-assembled zinc hydroxide/dodecyl sulfate ($Zn(OH)_2$/DS) nanostructures [259]. The concentration of SDS should be optimized because Zn@ZnO core-shell particles rather than $Zn(OH)_2$/DS will be produced at a much lower concentration of 10 mmol/L [260]. At the same SDS concentration of 10 mmol/L, Zeng et al. [262] produced a mixture of layered structures and particles with a pure phase of ZnO. Results indicate that ethanol facilitates the heterogeneous nucleation of $Zn(OH)_2$ nanolayers and their further assembly into 3D flower-like nanostructures [259].

If SDS does not participate in the reaction, it will act as a size inhibitor and phase manipulator, offering the possibility for both size and phase control. In pure water, a mixture of Zn and ZnO is produced, with ZnO dominating the product [262]. SDS with concentrations (i.e., 0.0001 and 0.001 mol/L) less than its CMC (0.008 mol/L) leads to the formation of pure ZnO nanostructures despite the difference in the absence/presence of nanolayers, whereas concentrations of 0.01 and 0.05 mol/L facilitate the formation of Zn@ZnO core-shell particles [262]. LAL of Zn at the SDS concentration of 0.1 mol/L produces core-shell particles with Zn as the core and ZnO/$Zn(OH)_2$ as the thin shell. This result indicates that a high concentration of SDS surfactants can efficiently depress the oxidation of Zn into ZnO and the dehydration of $Zn(OH)_2$ into ZnO. Cationic surfactant CTAB displays a weak adsorption capacity toward ZnO NPs; thus, surfactant-dependent structure evolution is normally unachievable. ZnO particles generated by LAL are often positively charged; hence, increasing CTAB concentration enhances the electrostatic repulsive force between ZnO NPs so their size and crystallinity can be increased and elevated,

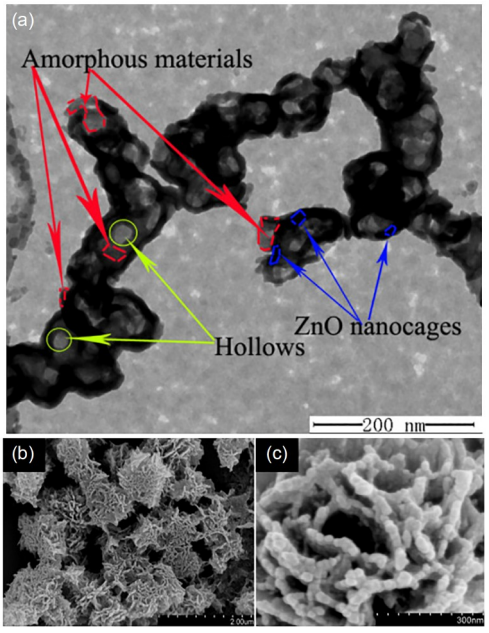

Figure 17 (Color online) TEM image (a) and SEM images (b), (c) of interconnect ZnO nano-cages generated by LAL of Zn metal in water-ammonia mixture with a volume ratio of 5:1. Scale bars are 200 nm in (b), (c). Copied from ref. [257] with permission.

Table 8 Summary of products obtained by LAL of Zn in different liquids, gas environments and post treatments using different laser parameters[a)]

Liquid	Laser	Atmosphere + post-treatment	Shape	Phase	Ref.
DMF+BDC	7 ns, 1064 nm, 5 Hz, 0.8-1 J/cm^2	air	cube, particle (0.8-1 μm)	MOF-5	[252]
Water	5 ns, 1064 nm; 200 ps, 30 fs, 800 nm	air, aging	cube (150-300 nm)	–	[72]
Water	0.5/1/2 ms, 1064 nm, 1/5 kW	air	nanorods	ZnO, Zn/ZnO	[253]
Water	7 ns, 355 nm, 10 Hz, 3.2 J/cm^2	40/60/80°C	spherical→columnar	ZnO	[254]
P. Pinnata leaf extract with 0% (pure water), 20%-40% ethanol-water concentration	6 ns, 1064 nm, 10 Hz, 530 J/cm^2	air	particles/rods mixture → spherical particles	ZnO (water), Zn/ZnO (other conditions)	[255]
Water + chloroauricacid ($HAuCl_4{\cdot}3H_2O$)	7 ns, 1064 nm, 10 Hz, 60 mJ/pulse	air	core-shell	Au@ZnO (speculated)	[256]
3% H_2O_2 water	8 ns, 355 nm, 10 Hz, 300 mJ/pulse	air	–	ZnO_2	[243]
Water + ammonia (V5:1)	10 ns, 1064 nm, 10 Hz, 8 GW/cm^2	air	flower-like, porous nano-cages	ZnO	[257]
Water	1064/532 nm, 800 mJ, $1.7\times10^{11}/8.3\times10^{10}$ W/cm^2	air	spherical, particulates, nanorod, nanoplate	Wurtzite-type (W)-ZnO and ε-$Zn(OH)_2$	[251]
TEOS	240 μs, 1064 nm, 10 Hz, 1000 mJ/pulse	air	core-shell	Zn/W-ZnO	[258]
Water + SDS (0.04 mol/L)	30 ns, 248 nm, 10 Hz, 4.3 J/cm^2	air	nanolayer	β-$Zn(OH)_2$/DS	[259]
Water + SDS (10 mmol/L)	10 ns, 1064 nm, 10 Hz, 35 mJ/pulse	air	elongated core-shell (500 nm long, 300 nm wide)	Zn@ZnO	[260]
Water + SDS (0.05 mmol/L)	532 nm, 10 Hz, 60 mJ/pulse	O_2	spherical (AVG 13.7 nm)	ZnO with possible ZnOOH	[261]
Water + SDS (0.0001, 0.001, 0.01, 0.05, and 0.1 mol/L)	10 ns, 1064 nm, 10 Hz, 70 mJ/pulse	air	core-shell (AVG 18.1-44.5 nm)	Zn@ZnO, Zn@$Zn(OH)_2$	[262]
Water + chitosan (20 g/L)	10 ns, 532 nm, 10 Hz, 60 mJ/pulse	air	spherical (AVG 5-9.4 nm)	ZnO	[263]
Water + CTAB (1 mmol/L)	130 fs, 800 nm, 1 kHz, 0.05/1.11/1.15 mJ/pulse	air	spherical	ZnO	[264]
Acetone	7 ns, 1064 nm, 100 mJ/pulse	air	core-shell (AVG 4.6 nm)	Zn, ZnO	[101]
Ethanol	10 ns, 532 nm, 10 Hz, 2.45-3.89 J/cm^2	air	spherical and hexagonal mixture (AVG 65-75 nm)	ZnO	[265]
Ethanol/water (vol ratio 1:4 or 1:3) + SDS (0.04 mol/L)	30 ns, 248 nm, 10 Hz, 4.3 J/cm^2	air	flower-like	β-$Zn(OH)_2$/DS, ZnO	[259]
Water + with different concentrations	7 ns, 1064 nm, 10 Hz, 100 mJ/pulse	air	spherical (AVG 25 nm)	ZnO	[266]
Cotton fabric aqueous solution	7 ns, 1064 nm, 10 Hz,	air	spherical (10-700 nm)	ZnO	[267]
Water	200 ps, 800 nm, 1 kHz, 0.54 mJ/pulse; 5 ns, 1064 nm, 10 Hz, 102 mJ/pulse; 60 fs, 800 nm, 1 kHz, 0.87 mJ/pulse	air, aging	spherical → cubic and rectangular	Zn, ZnO	[71]

a) BTC, benzene-1,3,5-tricarboxylic acid; MeOH, with methanol; DMF, dimethylformamide.

respectively [269].

Many shapes of ZnO nanomaterials have been prepared by LAL via varying liquid compositions, laser parameters, and environmental conditions. For example, novel ZnO nanocages (Figure 17(a)) displaying flower-like (Figure 17(b), (c)) morphologies under SEM observation have been prepared by LAL of Zn in a mixture of water and ammonia with the volume ratio of 5:1 [257]. Hollow structures form through the generation of NH_3. ZnO nanocages assemble into flower-like aggregate structures, with each flower-like nanosheet consisting of numerous NPs (Figure 17(b), (c)). Zn species may also react with $(NH_3)_4^{2+}$ to form $Zn(NH_3)_4^{2+}$ clusters to be embedded in nanocages [257]. Interestingly, ms-LAL of Zn in water and water-ethanol mixture produces nanorods, whose dimensions can be tuned by changing pulse duration and laser power [253]. The longest nanorods with a length of 225 nm and an aspect ratio of 6 are obtained at 1 ms and 1 kW, and nanorods with 200 nm length and an aspect ratio of 1.6 are obtained by 0.5 ms and 5 kW. Pure ethanol only allows the achievement of spherical particles irrespective of pulse durations, whereas ethanol-water mixture with a volume ratio of 9:1 enables the synthesis of ZnO nanorods, which indicates the essential existence of water for the synthesis of ZnO nanorods. This finding means that the

amount of OH groups decomposed during LAL in aqueous solutions is crucial for the synthesis of ZnO nanorods via dehydration of $Zn(OH)_2$.

Natural resources are attaining increasing attention because of their bioaffinity and environmental friendliness. Yudasari et al. [255] performed LAL of Zn in *Pometia pinnata* leaf extract (PPLE) solution and found that ZnO nanorods prepared in pure water transformed into smaller Zn/ZnO spherical particles after adding PPLE, indicating the reduction and capping capacities of PPLE. Pure Zn NPs are obtainable in aqueous solutions containing chitosan biomolecules to inhibit oxidation [263]. With the aid of polymer conjugation, the colloidal stability is much higher than that produced in water [263]. In a less oxidative environment provided by H_2O_2 (3%), ZnO_2 nanomaterials are produced [243]. Annealing of ZnO_2 for several hours at hundreds of °C (i.e., 200°C-600°C) allows a complete phase conversion from ZnO_2 to ZnO [243].

Ns-LAL of Zn in acetone produces a mixture of Zn and ZnO [101], whereas ms-LAL of Zn in ethanol produces pure Zn particles [253], which indicates the advantage of ms-LAL in synthesizing abnormal nanomaterials aside from nonspherical ZnO nanostructures [270]. In heptane, the products are $ZnO/Zn(OH)_2/ZnO_2$ nanocomposites with ZnO as the main phase [271], indicating the complexity of solvent-dependent ablation dynamics and chemical reactions. The common difference between colloids synthesized in organic solvents compared with those synthesized in water is their encapsulation by carbon shells and incapability to grow into nonspherical nanostructures because of the existence of carbon shells. In TEOS, high-pressure products, such as Zn@ZnO core-shell NPs with 1D commensurate (0001) Zn superstructure and wurtzite-type ZnO shell, can be obtained [258].

ZnO is a type of n-type II-VI semiconductor with broad applications, such as gas sensing [272], antibacterial [273], and photocatalysis [274]. Besides the direct application of LAL-synthesized ZnO colloids for photocatalysis [275], chemical etching of the Zn core of LAL-synthesized Zn@ZnO particles allows the formation of hollow ZnO photocatalysts [276]. Further enhancement of hollow ZnO particles for photocatalytic application can be realized by surface coating of Pt particles to construct ZnO/Pt composites [276]. Thermal treatment of LAL-synthesized ZnO and FeO_x colloids allows the synthesis of ternary oxide (i.e., $ZnFe_2O_4$) photocatalysts [277]. Benefiting from photocatalytic capacity, reactive oxygen species (ROS) generation, and internalization, LAL-synthesized ZnO [255], Zn/ZnO [255], and Zn@ZnO [255] colloids are also suitable for antibacterial applications. Successive LAL of Zn and Fe targets offers a good strategy to prepare antibacterial Fe-doped ZnO composites with a better performance than pure ZnO [278]. Along this route, Ag-ZnO [279] or Ag@ZnO [280] or Au-ZnO [281] composites with anticancer, photoluminescent, and gas-sensing capacities have also been developed.

3.8 Ru, Rh

Ru is a type of rare transition metal belonging to the iron group metal, which becomes oxidized in air at 800°C. Ru is thermodynamically stable as an hcp structure, but it has a metastable phase of fcc structure stable above 1819 K at ambient pressure [282]. Owing to LAL-induced high-temperature and high-pressure environment and ultrafast quenching, LAL offers a possibility to synthesize fcc-Ru NPs in organic solvents, including methanol, ethanol, and acetone, as shown in Figure 18(b)-(d) [283]. The products synthesized in pure water are shown in Figure 18(a) for comparison. In water, pure thermodynamically stable hcp Ru NPs are generated at 100 mJ. Increasing pulse energy to 200 mJ leads to certain oxidation of Ru particles to form RuO_2. Pure fcc-Ru particles are achievable by LAL in methanol (Figure 18(b)) and ethanol (Figure 18(c)) at 16 mJ/pulse. LAL in methanol and ethanol at other pulse energies of 50, 100, 150, and 200 mJ/pulse and LAL in acetone merely produces a mixture of fcc and hcp Ru particles. Normally, post irradiation must occur at high pulse energies. Hence, the phase transition from fcc Ru to hcp Ru phase through secondary irradiation is indispensable, which may explain the formation of mixed phases. Fcc metastable phase can also be obtained by annealing hcp Ru at 1819 K [283]. The higher the pulse energy, the higher the temperature can be induced. In this regard, fcc Ru would dominate the product synthesized by LAL at high pulse energies rather than low energies. Hence, another mechanism, such as the formation of fcc-carbon alloy [284], may be involved for its stability

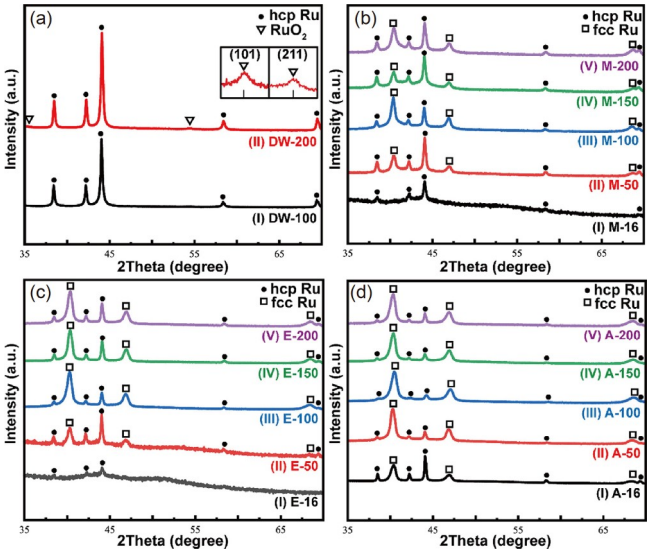

Figure 18 (Color online) XRD patterns of fcc Ru and hcp Ru NPs produced by LAL in different liquids at different pulse energies. (a) Water with 100 and 200 mJ/pulse. Methanol (b), ethanol (c) and acetone (d) with 16, 50, 100, 150 and 200 mJ/pulse. Copied from ref. [283] with permission.

after synthesis at room temperature. This work reveals the favorable condition for fcc-Ru production, which is helpful to develop fcc-Ru-based high-performance catalysts [285].

Rh is another rare noble metal with great potential to be applied as catalysts after downsizing its dimension to nanoscale [286]. Volpato et al. [287] produced Rh particles by LAL of Rh in water and ethanol using the experimental setup shown in Figure 19(a). Figure 19(b), (c) show the TEM images, size histograms, and SAED patterns of the particles synthesized in water and ethanol (termed as W-Rh-NPs and E-Rh-NPs), respectively. The particles synthesized in water are much larger than those synthesized in ethanol: (28±14) vs. (14±11) nm. SAED analysis of the colloids synthesized in water and ethanol indicates the formation of pure Rh NPs. XPS spectra in Figure 19(d) reveal that Rh colloids synthesized in water and ethanol are both subjected to surface oxidation with 73% and 84% Rh(0), respectively. Due to the absence of carbon coatings, Rh particles synthesized in water exhibit higher electrochemical performances than those synthesized in ethanol, as indicated by lower overpotential values, higher specific activity (SA, 1.69 vs. 0.70 mA cm^{-2}), mass activity (MA, 0.39 vs. 0.13 mA μg^{-1}) and turnover frequency (TOF, 0.21 vs. 0.07 s^{-1}), as shown in Figure 19(e). Different from the report from Volpato et al. [287], Fazio et al. [288] showed the possibility to synthesize Rh_2O_3 particles with sizes in the range of 2-12 nm via ns-LAL of Rh in water. The oxidation may be due to the shorter wavelength of 532 nm and longer ablation period of 40 min. After annealing the colloids at 200°C for 2 h, most colloids evolve into the RhO_2 phase, which can be further reversibly transformed into the Rh metal phase by thermal treatment in an H_2 environment. Regarding the application, LAL-Rh_xO_y colloids possess excellent gas-sensing selectivity for H_2 gas among all tested H_2, CO, CO_2, NO_2, and O_2 gases [288].

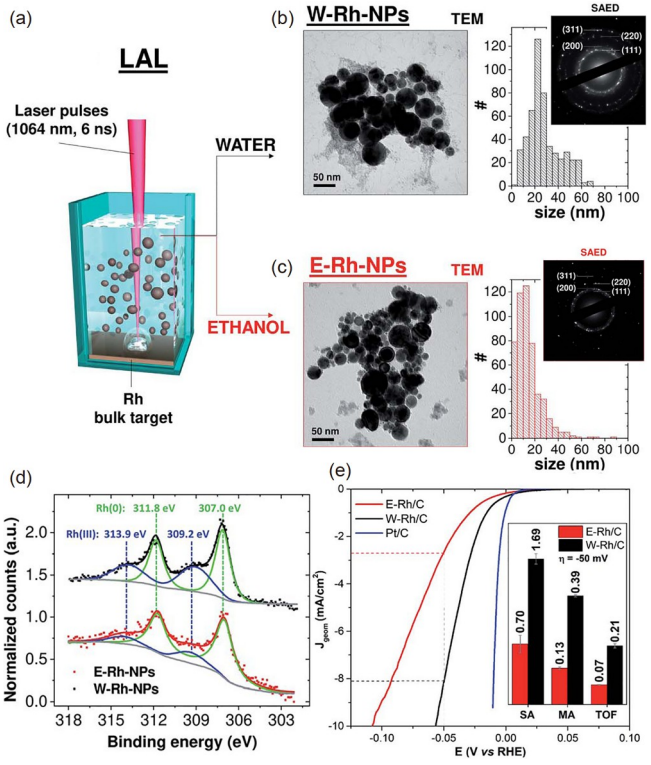

Figure 19 (Color online) LAL synthesis of Rh particles and electrochemical application. (a) Schematic illustration of LAL of Ru in water and ethanol using an ns laser (1064 nm, 6 ns). (b), (c) TEM images, SAED patterns, and size histograms of the W-Rh-NPs (water liquid) and E-Rh-NPs (ethanol). (d) XPS spectra of as-prepared Rh NPs. (e) Electrochemical performance (linear sweep voltammograms) of Rh/C NPs and commercial Pt/C at fixed metal loading (20 $\mu g_M\ cm^{-2}$) on GCE (0.196 cm^2), (2 mV s^{-1} IR compensated) in 0.1 mol/L H_2SO_4. Inset: specific activities (SA, expressed in mA cm_M^{-2}), mass activities (MA, mA μg_M^{-1}) and turnover frequencies (TOF, s^{-1}) at −50 mV of overpotential for W-Rh/C and E-Rh/C. Copied from ref. [287] with permission.

3.9 Pt

Pt-based NPs are important catalysts. The smaller the Pt NPs, the higher densities of active sites can be exposed to reactants, which is beneficial to promote catalytic performances [289]. The synthesis of atom catalysts is a research hotspot [290]. The activity and durability of Pt-based catalysts are closely related to their structural morphology [291]. Hence, size control and morphology manipulation of Pt NPs are important in LAL. Ns-LAL of Pt in water and SDS using a KrF excimer laser (wavelength 248 nm, frequency 10 Hz, pulse width 30 ns) yields microscale spherical and oval-shaped hollow particles because of the coalescence of small Pt NPs on the interface of cavitation bubbles [292]. Other reports based on fs [204], ps [293], and ns [101] lasers merely showed the possibility of producing solid Pt particles. Hence, this rare case [292] should be associated with a very strong thermal effect, which can anneal small Pt particles on the bubble interfaces. The amplitude of thermal effect depends on the pulse duration of lasers; a long pulse duration in the order of tens of ns facilitates the formation of large hollow structures, whereas a laser with a short pulse duration (5 ns) only produces small solid Pt particles with a bimodal size distribution (1-4 and 6-8 nm) [294].

Given that the instinct absorption peak of Pt colloids is approximately 150 nm, the fourth and third harmonic lasers can be adopted to induce the aggregation of LAL-synthesized Pt particles and melt them into submicrospheres [295]. Surfactants such as SDS are available to tune the size of Pt NPs in the range of 2-7 nm, but the concentration of SDS must be optimized to synthesize stable Pt colloids [296]. Stable Pt colloids are only achievable at the concentration of 0.01 mol/L [296]. Pt particles synthesized in water are much larger than those prepared in organic solvents because of the lack of the capping effect to inhibit particle growth [101] unless a strong fragmentation is induced. For example, the sizes of Pt NPs on GO nanosheets obtained via *in situ* LAL are 22, 18, 15, and 12 nm when the ablation periods are 5, 10,

15, and 20 min, respectively, indicating the fragmentation behavior of Pt during a long-period of LAL [297]. Installing an electric field is helpful to reduce the particle size because of its impact on the plasma plume, which is full of charged clusters and nuclei [62]. The particle size is proportional to the applied electric field, allowing the manipulation of colloid size from 20 to 9 nm within the electric field range of 0-20 V/cm [298].

Fragmentation is often performed using second (532 nm) and third (355 nm) harmonic lasers at high fluences [28]. Hence, in the synthesis of small Pt particles, LAL at high fluences using 532/355 nm-lasers can trigger *in situ* LFL, thus allowing the generation of Pt NPs dominated by small particles less than 3 nm. At the same fluence (i.e., 14 J/cm^2), large particles populated in the range of 5-15 nm make another modal size distribution because of the increase in the explosive boiling effect [299]. Under optimized conditions, LFL of Pt colloids by 355 nm laser irradiation can reduce the size to ~1.5 nm [300]. Other than melting and fragmentation, Pt alloying offers another methodology to upgrade Pt-based catalysts [301]. Taking advantage of short-wavelength (355 and 532 nm) lasers to irradiate Pt and other metallic (e.g., Au) mixed colloids paves the way to produce Pt-metal alloy particles with a composition manipulatable by the educt ratios [302].

In the cases of ns-LAL in organic solvents, such as acetone, ethanol, and methanol, aside from Pt NPs with sizes of tens of nm, a large amount of ultrasmall Pt NPs with sizes of 1-2 nm are normally generated [303], and their appearance is independent of laser parameters [101,303]. This phenomenon is abnormal because ultrasmall particles have not been generated from Au, Ag, and Cu colloids synthesized under the same conditions [101]. Taking the use of Pt particles synthesized by LAL of Pt in water as the study target (Figure 20(a), (b)), Zhang et al. [101] post-irradiated the colloid in acetone and unveiled the redispersion behavior of ultrasmall Pt NPs from the irradiated Pt particles, as shown in Figure 20(c)-(f). Originally, the Pt particles do not have small particles with sizes of 1-2 nm. After 15 min irradiation, the particle size slightly increases (Figure 20(c)) and carbon shells turn out, where many small 1-2 nm Pt particles can be found on the carbon shells (Figure 20(d)). After 60-min irradiation, particle size significantly increases (Figure 20(e)) but tiny Pt particles can still be found on the carbon shells (Figure 20(f)), which indicates that their appearance is independent of educt particle size. XPS analysis of Pt educt particles synthesized in water and 60 min-irradiated Pt particles in acetone reveals enhanced oxidation rates for the particles (Pt(II) peaks at 72.7 and 76.6 eV, Figure 20(g)) because of the redispersion effect caused by laser irradiation in acetone (Figure 20(i)). When the molten Pt is irradiated, many carbon species dissolute in Pt NPs because of the high solubility of carbon in

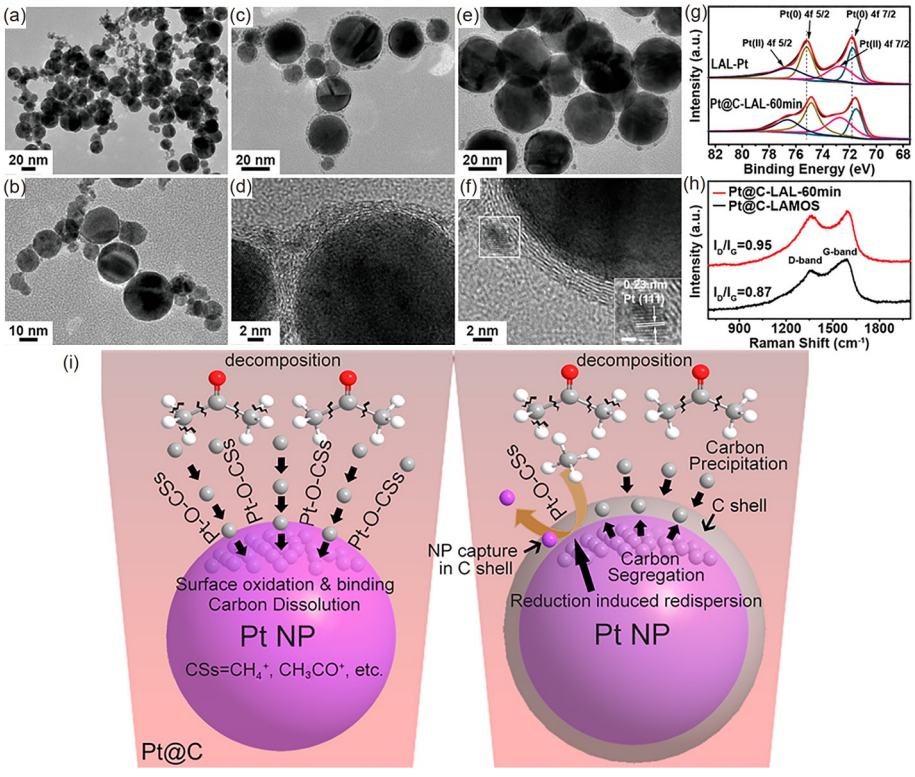

Figure 20 (Color online) TEM images of LAL-Pt NPs synthesized by laser ablation in water for 30 min (a), (b), and post-irradiation of LAL-Pt NPs in acetone for 15 min (c), (d) and 60 min (e), (f). XPS spectra of LAL-Pt NPs (generated in water) and Pt@C-LML-60 min NPs (g). Raman spectra of Pt@C-LML-60 min and Pt@C-LAMOS NPs (h). Pt tiny particles redispersion due to the sequential oxidation and reduction processes and carbon shell formation due to carbon precipitation and segregation (i). Copied from ref. [101] with permission.

Pt. In consequence, many byproducts from acetone decomposition are brought into Pt to induce the binding of Pt-O-CSs (CSs=CH^{4+}, CH_3CO^+, etc.), as illustrated in Figure 20(i). When Pt NPs cool down without irradiation, carbon solubility significantly decreases. In consequence, carbon segregates from Pt particles, during which a series of oxidation and reduction reactions occur, leading to the redispersion of 1-2 nm Pt NPs. This process can promise a continuous supply of ultrasmall Pt NPs. Compared with Pt@C NPs obtained by laser ablation of Pt in acetone, graphitization ratio of the onion-like carbon shells on Pt@C-LML-60 min NPs is much higher, as confirmed by the lower I_D/I_G value shown in the Raman spectra (Figure 20(h)), indicating the favorable long-lasting high-temperature environment induced by LML for carbon-shell graphitization. Jendrzej et al. [304] performed LFL of LAL-synthesized Pt colloids and studied their growth routes. The fragmented particles are broadly distributed with sizes in the range of 1-10 nm with an average diameter of (3.6±0.3) nm, larger than redispersed Pt NPs. This result indicates that redispersion is a better method than LFL for the generation of ultrasmall Pt NPs. However, ns laser irradiation of Pt particles induces the aggregation and fusion of small particles into large ones (Figure 20(e)). Hence, the combination of LFL in water and laser post-irradiation in organic solvents can be used to produce tiny Pt NPs continuously. Another factor that should be considered is the activity of ultrasmall particles, which can spontaneously grow into large particles or nanowires via ripening and coalescence mechanisms. For example, after 7-day aging of LFL-Pt colloids, the concentration of Pt particles larger than 8 nm significantly increases [304]. Elements in the solvent molecules may serve as dopants and reactants; for instance, LAL of bulk Pt in TEOS yields C-doped Pt and $Pt_{16}Si_7C_1$ [305].

The productivity of NPs has reached 4 g/h when a high-power ps laser system is used, and a polygon scanner is employed to perform a high-speed (500 m/s) scanning for bypassing cavitation bubbles [293]. This value is sufficient for practical applications. With the aid of a newly developed continuously operating tubular bowl centrifuge connected to the ablation chamber, desirable small Pt particles less than 10 nm can be collected directly after LAL [306]. This approach makes these particles convenient to be applied and helps to screen desirable Pt NPs without an additional centrifugation treatment. The surfaces of LAL-synthesized Pt NPs are partially oxidized, which differ in different reports, such as 64% metallic Pt, 28.2%±5% and 7.5%±5% of Pt^{2+} and Pt^{4+}, respectively in ref. [307], and 22% surface oxidation (10.8% of Pt^{2+}, 11.6% of Pt^{4+}) in ref. [308]. These surface charges make Pt particles highly stable with a ζ-potential value of (−58±3) mV [308]. LAL-synthesized negatively charged Pt particles [309,310] can be directly used for electrophoretic deposition (EPD) on neural electrodes [311] or conjugated on positively charged supports (e.g., graphene [312,313], rGO [309], TiO_2 [314,315], CeO_x [316], AlO_x [317,318]) via *in situ* or *ex situ* LAL for catalytic applications such as CO oxidation, NO oxidation, OER, and Li-air battery. Successive LAL of Pt and other easily oxidized metal targets such as Ti in water provides a methodology to construct metal/metal-oxide composite photocatalysts [114]. The amount of Pt particles on adsorbents is adjustable by changing the ablation period or adsorbent amount/mass in the liquids. The drawback is the difficulty in controlling the properties of the adsorbents and adsorbates. Despite having a larger dimension (6.6 vs. 3.8 nm) compared with the Pt NPs of commercial Pt/C catalysts, the mass-specific power density of carbonic-Vulcan supported laser-generated Pt composite catalysts is ~20% higher than that of commercial Pt/C catalysts [307]. The reduced dissolution rate of Pt NPs may induce their high stability for proton exchange membrane fuel cell (PEMFC) than the commercial Pt/C reference catalysts, with 88.4% and 72.2% retention of initial electrochemical active surface area (ECSA) after aging [307]. The optical (nonlinearity) and thermal (diffusivity and effusivity) properties of GO nanosheets can be enhanced by conjugating Pt NPs on them via *in situ* LAL [297].

LAL-Pt particles are efficient not only in inhibiting the growth of cancer cell lines [319] but also selectively efficient in killing most common drug resistant bacteria (*P. aeruginosa*) and less efficient toward *S. aureus*, *E. coli*, and *C. albicans* [319]. The antibacterial performance of LAL-Pt NPs toward dental-related bacteria (*Streptococcus mutans*; *Enterococcus faecalis*, *caries*; *Porphyromonas gingivalis*, and *endodontic* and *periodontal lesions*) has also been reported [320]. Although the plasmonic effect of Pt colloids is much lower or less distinguishable than that of Au colloids, Pt particles can still be assembled as photoactive films for applications in laser desorption ionization (LDI), Raman scattering (SERS), and infrared absorption (SEIRA) [294,321].

3.10 Pd

In analogy to Pt, palladium (Pd) is also a high-density silvery precious metal. Pd-based nanomaterials can be extensively applied for diverse purposes, such as hydrogen storage, fuel cell, and environmental remediation [322,323]. Given its similarity to Pt, the progress of LAL-Pd is briefly introduced, focusing on the differences as a supplement. Navas and Soni [324] showed that KBr ions and CTAB surfactants guide Pd particles to grow into nanocubes and decahedron/icosahedron Pd nanocrystals, incapable by SDS or in pure water [324]. Nishi et al. [325] found that the size of Pd NPs synthesized by LAL in heavy water is smaller (primary 8 nm) than that (primary 16 nm) synthesized in light water and that the as-prepared Pd NPs are superparamagnetic. Benefiting

from fragmentation and gently thermal effects caused by the second (532 nm) and third (355 nm) harmonic lasers, thin Pd nanowires are produced via LAL in water at a low fluence of 8.9 J/cm^2 [326,327]. Similar to the finding with respect to Pt [101], ns-LAL of Pd in organic solvents such as acetone, ethanol, 2-propanol, toluene, and *n*-hexane, yields a large number of small particles 1-2 nm in size because of the redispersion effect [328]. Thus, optimization of organic solvents and laser parameters for 532 nm-LAL paves the way for the synthesis of ultrasmall Pd particles with most of them within 1-2 nm, such as ps-LAL of Pd in 2-propanol at the fluence of 0.5 J/cm^2 [329]. In non-polar solvents such as toluene and *n*-hexane, Pd particles are unstable because of the lack of adsorbed anionic species, whereas Pd particles synthesized in acetone and alcohols are stable due to the presence of adsorbed anions such as enolates or alcoholates [328]. Stabilizers such as tetraoctylammonium bromide (TC_8ABr) ionic micelles can be added to organic solvents to ensure a high colloidal stability and to synthesize small particles [330]. The surfaces of Pd particles synthesized in organic solvents are partially oxidized depending on the composition of organic solvents, with the oxidation ratios of ~29% and 20% obtained in acetone and ethanol, respectively [328].

Post irradiation of Pd colloids with H_2PtCl_6 addition allows the generation of PdPt alloy particles, which can be used as adsorbates on CdS nanorods [326]. LAL of Pd in a $CuCl_2$ solution yields PdCu alloy particles possessing a synergistic effect to significantly enhance catalytic performance: 5.91 times kinetic rate increase for the catalytic hydrogenation of 4-nitrophenol to 4-aminophenol compared with that of monometallic Pd particles [331]. Through a model reduction of nitrobenzene to aniline by an excess amount of $NaBH_4$ and using Pd@C particles prepared by LAL in acetonitrile, Kim et al. [332] reported that carbon shells have the merits of increasing the adsorption rate and surface area, enlarging the electron concentration, and preventing particle aggregation; thus, Pd@C particles have a higher conversion efficiency than bare Pd counterparts.

Recently, Zhang et al. [333] synthesized Pd-aerogel composite catalysts and revealed their advantages of compressive strains to boost their applications for formate and ethanol electrooxidation. Figure 21(a) displays the synthesis procedures including *in situ* LAL in the presence of trisodium citrate (NaCA), *ex situ* addition of ascorbic acid (AA), and colloid aging. The aging period determines the colloid morphology. LAL of Pd in 35 mmol/L NaCA produces small Pd NPs with an average diameter of (3.1±0.6) nm (Figure 21(b)). After the addition of AA in LAL-Pd colloids to initiate gelation, particles start to connect and fuse, accompanied by an increase in the particle size (Figure 21(c), (d)). After 4 h aging, Pd nanowires form with an average diameter of 4.2 nm (Figure 21(e)). NaCA salts inhibit the aggregation of Pd particles preventing their fast growth. Without citrates, the size of Pd particles is as large as 11.3 nm. Given their higher specific surface area and the existence of compressive strains, Pd aerogel is more active than Pd/C for formate electrooxidation with mass and specific activities 2.26/1.99 times higher than those of commercial Pd/C catalysts [333]. Supported Pd composite catalysts have been prepared by *in situ* LAL in MWCNTs-containing solutions [334] and *ex situ* mixing of a biowaste extraction of calcium lignosulfonate for catalytic energy storage [335]. High-temperature calcination of the mixed colloids at temperatures of hundreds of °C is helpful to promote partial dissolution, facilitating the construction of heterogeneous catalysts. For example, the mixed Pd and CeO_x colloids cannot initiate low-temperature CO oxidation; however, Pd/CeO_2 (synthesized by LAL in alcohol) composites possess a high low-temperature activity after calcination [336].

4 Main group metal (Al)

Pure aluminum (Al) is an energetic material with a high negative enthalpy (ΔHB) of combustion. Downsizing bulky Al into nanoscale can significantly lower the enthalpy of Al

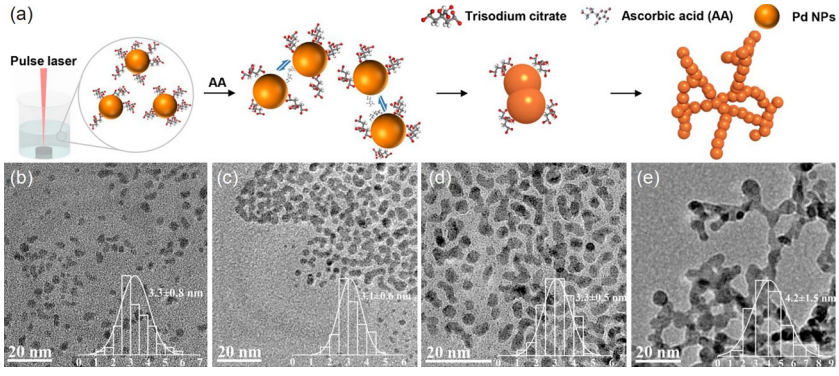

Figure 21 (Color online) *In situ* and *ex situ* LAL synthesis of Pd-aerogel composite. (a) Schematic illustration for composite synthesis procedure including *in situ* LAL in the presence of 35 mmol/L trisodium citrate (NaCA), post-addition of ascorbic acid (AA) in the Pd colloid after LAL and aging the mixed colloid. (b)-(e) TEM images of LAL-synthesized Pd NPs and Pd-aerogel composites after different periods of aging. Insets in (b)-(e) are size histograms. Copied from ref. [333] with permission.

materials from −1675 kJ/mol (bulky Al) to −2324 kJ/mol for a single Al atom. Thus, much attention is paid to applying them as rocket propellants, explosives, and pyrotechnics [337]. Small Al NPs less than 100 nm are highly reactive and favorable for these applications because propellant formulation can get access to an enhanced propellant burning rate than micron-sized particles after the addition of Al NPs. Al is susceptible to surface oxidation to form oxides, which is the "dead weight" for combustion; thus, active Al particles are often coated with silica [338] or carbon shells [339] to produce pure Al NPs to fully use their energy for combustion. Carbon coating is also appropriate for combustion applications because carbon evolves into CO_2/CO gases without the risk of causing ash residue' blocking on the active sites of Al surfaces. Davari et al. [337] successfully prepared A1@C core-shell particles by LAL of Al in acetone and toluene, as shown in Figure 22(a), (b). The carbon matrix was identified by HRTEM, Raman, and electron energy-loss spectroscopy. Al particles synthesized in acetone and toluene are unimodally (peak at 15.7 nm) and bimodally distributed (25 and 77.2 nm), both of which are smaller than 100 nm, suitable for combustion applications. The energetic properties of LAL-synthesized Al@C particles and commercial Al NPs (80 nm) were evaluated by laser-induced air shock from energetic materials to investigate their energetic properties [340]. Because of the smaller particle size and narrower size distribution, Al@C particles prepared in acetone have the highest laser-induced shock velocities (>755 m/s) than those prepared in toluene and commercial Al powders and the blank tape without any Al particles (Figure 22(c)). Results of thermo-gravimetric analysis in Figure 22(d) indicate the

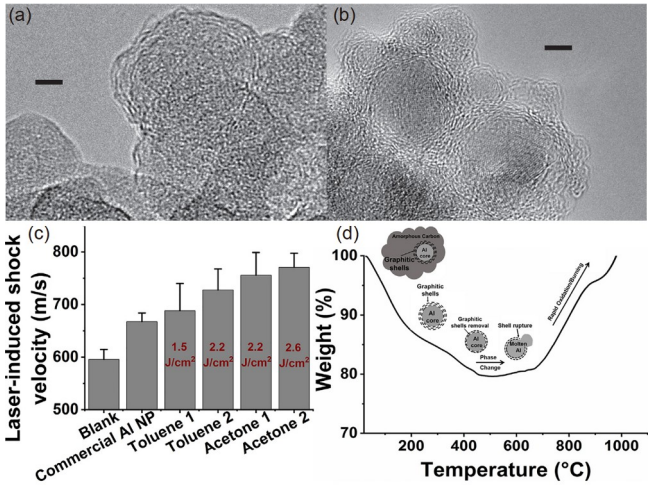

Figure 22 (Color online) Al@C core-shell particle synthesis by LAL and its combustion application. (a) HRTEM images of Al@C NPs prepared by LAL in (a) acetone and (b) toluene. Scale bars in (a), (b) are 3 and 5 nm, respectively. (c) Laser-induced shock velocities measured from LASEM technique for blank, commercial Al NPs, Al@C NPs prepared by LAL in acetone and toluene at different laser fluences. (d) TGA analysis of Al@C NPs synthesized by LAL in acetone at 2.6 J/cm^2. Copied from ref. [337] with permission.

oxidation behaviors of LAL-synthesized Al@C particles upon increasing temperature. The weight first gradually decreases until ~470°C because of carbon transition into CO_2 and CO, slightly changes due to the solid-to-liquid phase transition, and then dramatically increases due to oxidation. Such data suggest that LAL-produced Al@C particles are slightly oxidized. The demonstration of successful synthesis of Al@C particles via LAL and its attempt to be used for combustion may extend the application scope of LAL-synthesized nanomaterials, but the productivity should be a challenging issue because it is currently in the mg/h scale for LAL in organic solvents [341]. Increasing the pulse energy for LAL of Al in organic solvents is risky to ignite organic solvents, especially when using ns or ms lasers. LAL in organic solvents is accompanied by the decomposition of organic solvents, which significantly reduces LAL productivity [11] to a level much lower than the case of LAL in water (i.e., g/h) [293]. The size of Al particles is greatly influenced by the ablation period because of fragmentation and is strongly dependent on the employed organic solvents because of possibly varying ablation dynamics [341]. Oxide phases are also producible in organic solvents. For example, γ-Al_2O_3 particles are generated by LAL of Al in ethanol, and post-treatment by means of laser irradiation can only change the particle size, incapable of altering the phases [342], as shown in Table 9 [343-351].

Table 9 lists the products that have been generated by LAL of Al in different liquids under different conditions, where diverse shapes and phases of nanomaterials deserve special attention. Hollow particles are producible by LAL of Al in organic solvents. For example, LAL of Al in ethanol with saturated H_2 gases leads to the formation of hollow core-shell particles with Al_2O_3 as the outmost shell, amorphous Al as the intermediate layers, and fcc Al and cavities as the innermost parts, as shown in Figure 23(a) and (b) [343]. The formation of such abnormal nanostructures benefits from the faster cooling rate in the outmost part than in the inner part, which gives birth to the formation of an amorphous structure. Fast solidification rate originates from the ultrafast temperature quenching rate of ultrafast laser ablation, in the order of 10^{10}-10^{12} K/s. Crystallization into fcc Al in the cores may be facilitated by the high pressure of its surrounding hydrogen. Dissolved H_2 gases in liquid may participate in the nucleation and coalescence of Al particles through the formation of liquid Al hydrides (AlH_x). However, hydrogen uptake of AlH_3 is almost completely irreversible [352]. Thus, the mechanism proposed by the authors still needs verification. Gaseous H_2 may be captured by the solidified Al layers, which prevent the gas diffusion outside the NPs. Hollow Al-based spheres are also producible by LAL in the mixture of water-ethanol without H_2 gas purging [93]. The hollow structures in the microscale are amorphous with smooth surfaces (Figure 23(c)-(e)). After annealing at 800°C and

Table 9 Summary of products obtained by laser ablation of Al in different liquids, gas environments under different laser conditions

Liquid	Laser	Atmosphere	Post treatment	Shape	Phase	Ref.
Acetone or toluene	4 ns, 1064 nm, 10 Hz, 2.6 J/cm^2	air	–	spherical (15.7 nm in acetone, 25/77.2 nm in toluene)	Al@C	[337]
Ethanol	30 ps, 1.06 μm, 10 Hz, 4 J/cm^2	H_2	–	hollow (AVG 30 nm)	Al	[343]
Methanol + ascorbic acid	7 ns, 1064 nm, 10 Hz, 140 mJ/pusle	Ar	–	core-shell (20-30 nm)	Al-Al_2O_3@C	[344]
White vinegar	6 ns, 532 nm, 10 Hz, 2 W	air	–	spherical (AVG 12±9 nm)	Al@C and γ-Al_2O_3	[345]
Water	8 ns, 1064 nm, 10 Hz, 20/55 J/cm^2	air	–	spherical (peaks at 25, 28 nm)	Al and Al_2O_3	[346]
Water	6-7 ns, 1064 nm, 10 Hz, 120 mJ/pulse	air	–	spherical (3-14 nm)	α-Al_2O_3	[347]
Water	1064 nm, 2 Hz, 1/3/5 J/pulse	air	–	spherical (AVG 26/38/53 nm)	γ-Al_2O_3	[348]
Water + NaOH	16 ns, 1064 nm, 10 Hz, 850 mJ/pulse	air	–	spherical, microplates	γ-Al_2O_3 and β-$NaAlO_2$	[349]
Ethanol	7 ns, 1064 nm, 10 Hz, 7500 J/cm^2	air	laser irradiation (80 mJ/pulse, 0/20/40 min)	spherical (AVG 65/42/23 nm)	γ-Al_2O_3	[342]
Water-ethanol mixture	30 ns, 248 nm, 10 Hz, 5.9 J/cm^2, 30 min; 2.3 J/cm^2, 5 min	air	air + annealing; air	hollow	Amorphous → γ-Al_2O_3 → θ-Al_2O_3, γ-Al_2O_3 and α-Al_2O_3; amorphous and cubic Al mixture	[93,350]
Water	5 ns, 1064/355 nm, 10 Hz, 48 mJ/pulse, 30 min	air	aging	spherical	Al, Al_2O_3, $Al(OH)_3$	[351]
Water	200 ps, 800 nm, 1 kHz, 0.56 mJ/pulse, 30 min	air	aging	conical, bow-tie	Al_2O_3 $3H_2O$, $Al(OH)_3$	[351]
Water	30 fs, 800 nm, 1 kHz, 0.68 mJ/pulse, 30 min	air	aging	polygonal	Al, Al_2O_3	[351]

1100°C, pure γ-Al_2O_3 crystals (Figure 23(f)-(h)) and mixed phases of γ-/θ-/α-Al_2O_3 crystals (Figure 23(i)-(k)) grow on the shell structures, respectively. Results of this experiment suggest that θ-/α-Al_2O_3 forms at high temperatures, whereas γ-Al_2O_3 forms at relatively low temperatures. Alumina has four typical phases, including γ-, δ-, θ-, and α-Al_2O_3, with the phase transition following the order of γ-Al_2O_3 → δ-Al_2O_3 → θ-Al_2O_3 → α-Al_2O_3 [353]. γ-Al_2O_3 transforms into δ-Al_2O_3 upon heating at 800°C, which further evolves into θ-Al_2O_3 upon increasing heating temperature. α-Al_2O_3 forms when the heating temperature is above 1200°C.

White vinegar consisting of 4%-7% acetic acid and 93%-96% water is another mixture of water and organic solvent that has been used for LAL of Al, which produces a mixture of Al@C and γ-Al_2O_3 with an average diameter of (12±9) nm and size span of 2-50 nm when adopted as LAL liquid [345]. The presence of water may facilitate the formation of γ-Al_2O_3 particles, which agrees with the report by Piriyawong et al. [348]. Target inclination and pH adjustment of aqueous solutions offer two methodologies to tune the sizes and phases of nanomaterials synthesized by LAL of Al. Inclined targets may cause less coalescence of ejected particles because the laser cannot irradiate them during their release at the moment of bubble collapse [354]. Acid HCl and alkaline NH_4OH, which can introduce different concentrations of H^+ and OH^- radicals, are helpful to tune the agglomerate state in the bubble phase [354]. pH=11.0 facilitates the formation of small particles with a narrow size distribution. Simultaneous adjustment of pH and 45°-inclination of the ablated sample allows further reduction of particle size and size distribution [354]. Acid and alkaline additives may interact with metal species to form abnormal phases. For example, aside from γ-Al_2O_3 and α-Al_2O_3, diaspore [α-AlO(OH)] (a hydrated polymorph of α-Al_2O_3) and boehmite [γ-AlO(OH)] (a hydrated polymorph of γ-Al_2O_3) are generated at pH of 2.5 and 10.0 but unachievable at pH of 3.0 and 11.0 [354].

Aside from temperature-dependent phase transition, the thermodynamic stability of α-phase and γ-phase is also correlated with particle size. γ-Al_2O_3 particles are energetically stable when their surface area is larger than 125 $m^2 g^{-1}$ at room temperature [338], corresponding spheres with a diameter less than 12 nm, above which threshold α-phase prevails. However, Riahi et al. [347] synthesized α-Al_2O_3 NPs with diameters of 3-14 nm. Piriyawong et al. [348] prepared γ-Al_2O_3 particles of tens of nm in diameter, just opposite the trend of theoretically calculated size-governed thermodynamic stability [338]. Temperature possibly governs the formation of α-Al_2O_3 and γ-Al_2O_3 phases. Under hydrothermal conditions of 320°C-400°C and 1.5-10 MPa, α-Al_2O_3 can be formed, whereas γ-Al_2O_3 formation needs almost the same pressure but requires a high temperature above 400°C [355]. The reason why pure stable

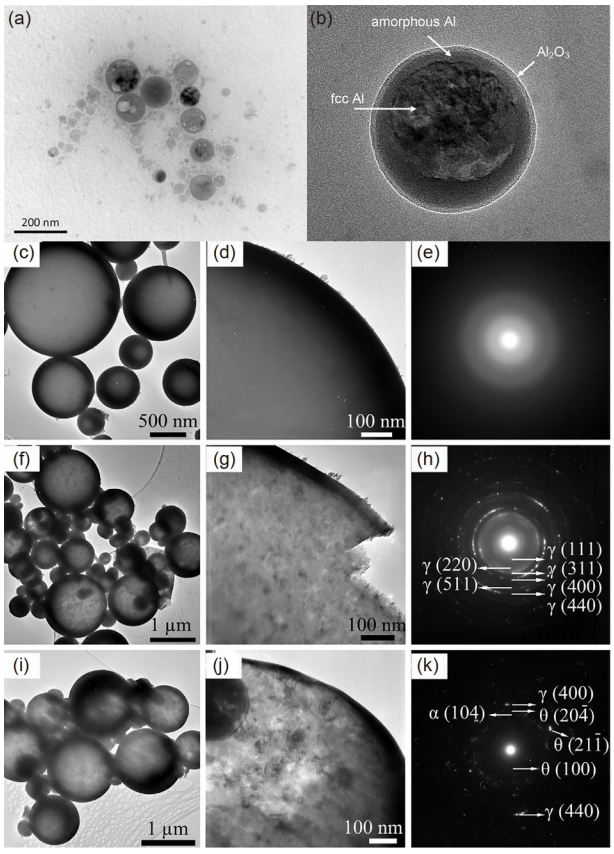

Figure 23 (a), (b) TEM images of particles prepared by LAL of Al in ethanol saturated with H_2 gases. Reprinted from ref. [344], copyright 2010 Elsevier. (c)-(e), (f)-(h), (i)-(k) TEM images and SEAD patterns of amorphous particles prepared by LAL of Al in a water-ethanol mixed solution with their volume ratio of 3:1, the particles annealed at 800°C and 1100°C, respectively. Copied from ref. [93] with permission.

α-Al_2O_3 and γ-Al_2O_3 particles with abnormal sizes can be produced by LAL is still a challenge to be addressed.

In aqueous solutions including water, γ-, δ-, θ-, and α-Al_2O_3 are producible with additional products of H^+/Al^{2+} co-doped alumina [356] and β-$NaAlO_2$ [349]. In view that the four phases of Al_2O_3 correspond to different synthesis conditions, LAL of Al with varying laser parameters can produce different high-temperature and high-pressure environments, which complex the products, and arouse the formation of many metastable phases. XRD characterization is often used to identify the phases of LAL-products, which may omit metastable phases that exist merely in a few particles. Hence, HRTEM and SAED analyses of LAL products are recommended to integrate with XRD characterization to see how crystals transform from the crystallographic perspective.

Aging-induced morphology transition also occurs to LAL-synthesized alumina particles with the evolution routes strongly dependent on the adopted laser parameters (pulse duration and wavelength). Particles synthesized by ns-LAL, ps-LAL, and fs-LAL can evolve into large spheres, conical/bow-tie, and polygonal structures, respectively [351]. For ns-LAL, laser wavelength greatly influences the size of evolved structures. Third harmonic (355 nm) laser enables the formation of large spheres after 60-day aging than the first harmonic laser (1064 nm), which may be because of the high aggregation rates and difference in particle compositions [351]. Ns-LAL at 1064 and 355 nm produces a mixture of Al, Al_2O_3, and $Al(OH)_3$, but the latter has a higher density of $Al(OH)_3$ crystals. Fs-LAL and ps-LAL induce the formation of Al/Al_2O_3 and $Al/Al_2O_3/Al_2O_3 3H_2O/Al(OH)_3$ mixtures [351]. LAL of Al in methanol containing ascorbic acid under Ar gas environment (Figure 24(a)) yields Al-Al_2O_3@C core-shell NPs (C shell thickness is 4.5 nm, Figure 24(b)) with a featured absorption peak adjustable in the range of 244.2-251.4 nm (Figures 24(c), (e)) by changing the ablation period due to the variation in the colloid sizes (Figure 24(f), (g)) [344]. Alteration of liquid composition can help to tune the structural morphology. For instance, core-shell and spindle-like structures are produced in toluene with ascorbic acid and in pure water, respectively [344]. The deep-ultraviolet localized surface plasmon resonance of Al@C parti-

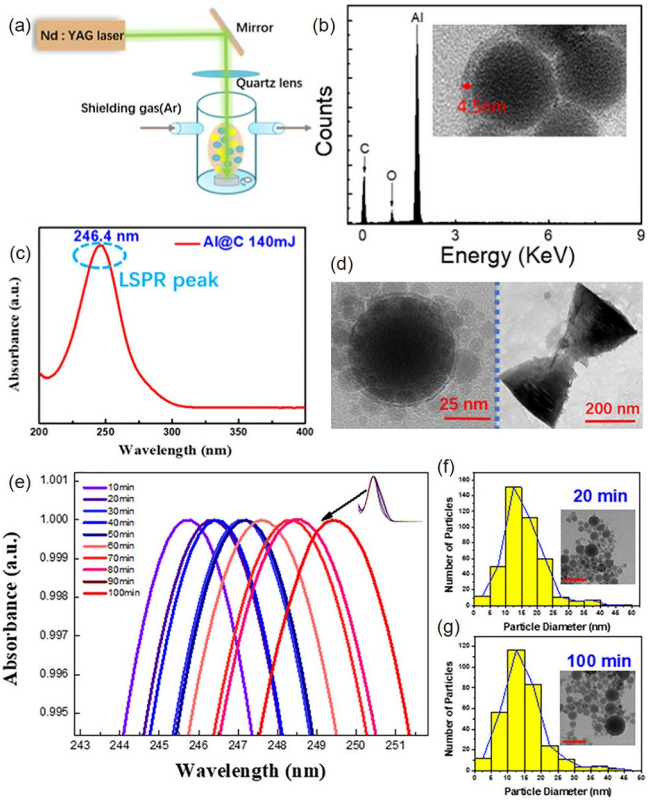

Figure 24 (Color online) LAL synthesis of plasmonic A1@C particles. (a) Experiment setup with saturated shielding Ar gas. (b) TEM image and EDS spectrum of Al@C NPs prepared by LAL in methanol and ascorbic acid mixed solvents. (c) Absorbance of Al@C NPs in methanol. (d) TEM images of Al NPs generated in toluene with ascorbic acid and in pure water, respectively. (a) Absorbance of Al@C NPs fabricated by LAL in methanol and ascorbic acid mixed solvents under different laser exposure times. (f), (g) Size histograms and TEM images of Al@C NPs prepared by 20 and 100 min LAL, respectively (scale bar: 50 nm). Copied from ref. [345] with permission.

cles can be used to enhance the PL emission of $CsPbBr_{3-x}Cl_x$ crystals when they are closely placed. Alumina particles synthesized by LAL can also be used as an antireflective coating to enhance the sensitivity of silicon photodiodes [357] or as aqueous nanofluids to enhance their thermal conductivity [347].

5 Summary

This review emphasizes the manipulation of phases, sizes, and morphologies of nanomaterials prepared by LAL. The lists of products produced under various conditions with almost infinite combinations. RLAL is a ubiquitous phenomenon that occurs in non-noble materials, such as Mg, Mn, Fe, Co, Ni, Cu, and Zn, leading to the formation of oxides, carbides, nitrides, and hydroxides. Under optimized conditions such as removal of dissolved oxygen or with the protection of polymer molecules or carbon shells, pure metal nanomaterials are producible, even for very reactive metals such as Mg. Redispersion of 1-2 nm particles occur to both Pd and Pt NPs during LAL or laser irradiation in organic solvents [101] and renders the possibility to break the limitation of laser parameters, such as pulse duration to synthesize ultrasmall Pd/Pt particles with high specific surface areas for catalytic applications.

A large variety of nonspherical nanomaterials have been produced by LAL of metals (Tables 1-9) following the six mechanisms proposed in ref. [34]. This review only displays a glimpse at the diversity of liquids, targets, and products with respect to limited selective metals, which may serve as a guide for a better design and control of desirable nanomaterials. However, under the same processing condition, reactions occurring to different metals may be very different. Thus, the empirical conclusions from the discussed results may not be applicable to other metals. In addition, LAL contains many processes [28], most of which are like "black box" to be explored. Although decades of efforts have been dedicated to the synthesis of nanomaterials and a significant advance has been witnessed, many challenging issues still need to be addressed, such as

(1) The reason why different shapes of nanostructures are produced for LAL of a defined metal target using different laser systems, which is of great importance for an accurate control of nucleation, growth routes, and growth rates.

(2) The mechanism of how solvents become decomposed during LAL and how these newly generated reactants react with the active species released from the ablated targets from the atomic or molecular viewpoint.

(3) Experimental recording of the nucleation and growth process to clarify the roles of additives (i.e., surfactant, polymer, salt, support materials, or other colloids) or by-products on the growth dynamics.

(4) Experimental measurement of the pressures and temperatures within the whole process of ablation, which lays the foundation to explain the formation of metastable phases.

(5) Quantification of atoms, ions and clusters ejected from targets and those generated from decomposed liquid molecules, which is crucial to interpret the formation of non-stoichiometric oxide and doped materials.

1 H. Kamyab, J. J. Klemeš, Y. V. Fan, and C. T. Lee, Energy **207**, 118104 (2020).
2 M. Khalil, G. T. M. Kadja, and M. M. Ilmi, J. Ind. Eng. Chem. **93**, 78 (2021).
3 J. Park, J. C. Hwang, G. G. Kim, and J. U. Park, InfoMat **2**, 33 (2020).
4 X. Wang, L. Chen, L. Wang, Q. Fan, D. Pan, J. Li, F. Chi, Y. Xie, S. Yu, C. Xiao, F. Luo, J. Wang, X. Wang, C. Chen, W. Wu, W. Shi, S. Wang, and X. Wang, Sci. China Chem. **62**, 933 (2019).
5 Y. Wu, H. Pang, Y. Liu, X. Wang, S. Yu, D. Fu, J. Chen, and X. Wang, Environ. Pollut. **246**, 608 (2019).
6 J. Chen, C. Ning, Z. Zhou, P. Yu, Y. Zhu, G. Tan, and C. Mao, Prog. Mater. Sci. **99**, 1 (2019).
7 Z. Guo, Y. Chen, Y. Wang, H. Jiang, and X. Wang, J. Mater. Chem. B **8**, 4764 (2020).
8 S. Hassan, G. Prakash, A. Bal Ozturk, S. Saghazadeh, M. Farhan Sohail, J. Seo, M. Remzi Dokmeci, Y. S. Zhang, and A. Khademhosseini, Nano Today **15**, 91 (2017).
9 N. Baig, I. Kammakakam, and W. Falath, Mater. Adv. **2**, 1821 (2021).
10 T. H. Maiman, Nature **187**, 493 (1960).
11 D. Zhang, B. Gökce, S. Sommer, R. Streubel, and S. Barcikowski, Appl. Surf. Sci. **367**, 222 (2016).
12 D. Zhang, B. Ranjan, T. Tanaka, and K. Sugioka, Int. J. Extrem. Manuf. **2**, 015001 (2020).
13 D. Zhang, L. C. Wu, M. Ueki, Y. Ito, and K. Sugioka, Int. J. Extrem. Manuf. **2**, 045001 (2020).
14 Y. Zhang, Y. Jiao, C. Li, C. Chen, J. Li, Y. Hu, D. Wu, and J. Chu, Int. J. Extrem. Manuf. **2**, 032002 (2020).
15 D. Zhang, R. Liu, and Z. Li, Int. J. Extrem. Manuf. **4**, 015102 (2022).
16 R. Liu, D. Zhang, and Z. Li, J. Mater. Sci. Tech. **89**, 179 (2021).
17 X. Xie, C. Zhou, X. Wei, W. Hu, and Q. Ren, Opto-Electron. Adv. **2**, 18001701 (2019).
18 D. Serien, and K. Sugioka, Opto-Electron. Adv. **1**, 18000801 (2018).
19 Y. Hu, Z. Wang, D. Jin, C. Zhang, R. Sun, Z. Li, K. Hu, J. Ni, Z. Cai, D. Pan, X. Wang, W. Zhu, J. Li, D. Wu, L. Zhang, and J. Chu, Adv. Funct. Mater. **30**, 1907377 (2020).
20 Y. Hu, H. Yuan, S. Liu, J. Ni, Z. Lao, C. Xin, D. Pan, Y. Zhang, W. Zhu, J. Li, D. Wu, and J. Chu, Adv. Mater. **32**, 2002356 (2020).
21 C. Xin, L. Yang, J. Li, Y. Hu, D. Qian, S. Fan, K. Hu, Z. Cai, H. Wu, D. Wang, D. Wu, and J. Chu, Adv. Mater. **31**, 1808226 (2019).
22 M. H. Mosallanejad, B. Niroumand, A. Aversa, and A. Saboori, J. Alloys Compd. **872**, 159567 (2021).
23 X. Q. Liu, B. F. Bai, Q. D. Chen, and H. B. Sun, Opto-Electron. Adv. **2**, 19002101 (2019).
24 E. Lee, B. Sun, J. Luo, S. Singh, D. Choudhury, D. Yong, X. Yu, and Q. Wang, Opto-Electron. Adv. **3**, 190039 (2020).
25 M. Kim, S. Osone, T. Kim, H. Higashi, and T. Seto, KONAPowder Part. J. **34**, 80 (2017).
26 V. Amendola, D. Amans, Y. Ishikawa, N. Koshizaki, S. Scirè, G. Compagnini, S. Reichenberger, and S. Barcikowski, Chem. Eur. J. **26**, 9206 (2020).
27 A. Fojtik, and A. Henglein, Berichte Bunsen-Gesellschaft **97**, 252 (1993).
28 D. Zhang, B. Gökce, and S. Barcikowski, Chem. Rev. **117**, 3990

(2017).
29 S. Reichenberger, G. Marzun, M. Muhler, and S. Barcikowski, ChemCatChem **11**, 4489 (2019).
30 D. Zhang, J. Liu, P. Li, Z. Tian, and C. Liang, ChemNanoMat **3**, 512 (2017).
31 J. Zhang, M. Chaker, and D. Ma, J. Colloid Interface Sci. **489**, 138 (2017).
32 J. Xiao, P. Liu, C. X. Wang, and G. W. Yang, Prog. Mater. Sci. **87**, 140 (2017).
33 A. Kanitz, M. R. Kalus, E. L. Gurevich, A. Ostendorf, S. Barcikowski, and D. Amans, Plasma Sources Sci. Technol. **28**, 103001 (2019).
34 D. S. Zhang, J. Liu, and C. H. Liang, Sci. China-Phys. Mech. Astron. **60**, 074201 (2017).
35 D. Zhang, and B. Gökce, Appl. Surf. Sci. **392**, 991 (2017).
36 R. C. Forsythe, C. P. Cox, M. K. Wilsey, and A. M. Müller, Chem. Rev. **121**, 7568 (2021).
37 S. X. Liang, L. C. Zhang, S. Reichenberger, and S. Barcikowski, Phys. Chem. Chem. Phys. **23**, 11121 (2021).
38 N. G. Semaltianos, and G. Karczewski, ACS Appl. Nano Mater. **4**, 6407 (2021).
39 N. Lasemi, and G. Rupprechter, Catalysts **10**, 1453 (2020).
40 H. Du, V. Castaing, D. Guo, and B. Viana, Ceram. Int. **46**, 26299 (2020).
41 M. C. Sportelli, M. Izzi, A. Volpe, M. Clemente, R. A. Picca, A. Ancona, P. M. Lugarà, G. Palazzo, and N. Cioffi, Antibiotics **7**, 67 (2018).
42 D. Zhang, Z. Li, and K. Sugioka, J. Phys. Photon. **3**, 042002 (2021).
43 S. Wu, J. Liu, Y. Ye, Z. Tian, X. Zhu, and C. Liang, ACS Appl. Energy Mater. **120**, 9028 (2019).
44 O. R. Musaev, M. S. Driver, E. A. Sutter, A. N. Caruso, J. M. Wrobel, and M. B. Kruger, Appl. Phys. A **113**, 355 (2013).
45 G. Bajaj, and R. K. Soni, Appl. Phys. A **97**, 481 (2009).
46 S. Wu, J. Liu, Y. Ye, Z. Tian, P. Li, Y. Cai, Y. Lin, and C. Liang, Appl. Surf. Sci. **471**, 469 (2019).
47 C. Zhu, X. Dong, X. Mei, M. Gao, K. Wang, and D. Zhao, Appl. Surf. Sci. **568**, 150978 (2021).
48 M. K. Singh, M. C. Mathpal, and A. Agarwal, Chem. Phys. Lett. **536**, 87 (2012).
49 Z. Tian, C. Liang, J. Liu, H. Zhang, and L. Zhang, J. Mater. Chem. **21**, 18242 (2011).
50 Z. Tian, C. Liang, J. Liu, H. Zhang, and L. Zhang, J. Mater. Chem. **22**, 17210 (2012).
51 T. Sasaki, Y. Shimizu, and N. Koshizaki, J. Photochem. Photobiol. A-Chem. **182**, 335 (2006).
52 C. Liang, Y. Shimizu, T. Sasaki, and N. Koshizaki, J. Phys. Chem. B **107**, 9220 (2003).
53 D. Sapkota, Y. Li, O. R. Musaev, J. M. Wrobel, and M. B. Kruger, J. Laser Appl. **29**, 012002 (2017).
54 H. S. Desarkar, P. Kumbhakar, and A. K. Mitra, Mater. Charact. **73**, 158 (2012).
55 S. Wu, J. Liu, D. Liang, H. Sun, Y. Ye, Z. Tian, and C. Liang, Nano Energy **26**, 699 (2016).
56 Y. Ye, P. Wang, E. Dai, J. Liu, Z. Tian, C. Liang, and G. Shao, Phys. Chem. Chem. Phys. **16**, 8801 (2014).
57 M. Y. Sun, J. Yang, T. Lin, and X. W. Du, RSC Adv. **2**, 7824 (2012).
58 T. Gu, J. Gao, E. E. Ostroumov, H. Jeong, F. Wu, R. Fardel, N. Yao, R. D. Priestley, G. D. Scholes, Y. L. Loo, and C. B. Arnold, ACS Appl. Mater. Interfaces **9**, 18911 (2017).
59 Y. Hamanaka, M. Iwata, and J. Katsuno, Appl. Phys. A **123**, 425 (2017).
60 S. Vadavalli, S. Valligatla, B. Neelamraju, M. H. Dar, A. Chiasera, M. Ferrari, and N. R. Desai, Front. Phys. **2**, 57 (2014).
61 O. R. Musaev, E. A. Sutter, J. M. Wrobel, and M. B. Kruger, J Nanopart Res **14**, 654 (2012).
62 P. Liu, C. X. Wang, X. Y. Chen, and G. W. Yang, J. Phys. Chem. C **112**, 13450 (2008).
63 Y. Li, O. R. Musaev, J. M. Wrobel, and M. B. Kruger, J. Laser Appl. **28**, 022004 (2016).
64 M. Rodio, A. Scarpellini, A. Diaspro, and R. Intartaglia, J. Mater. Chem. C **5**, 12264 (2017).
65 J. A. Serrano-Ruz, E. Campos-González, J. Santoyo-Salazar, J. S. Arias-Cerón, A. Chávez-Chávez, G. Gómez-Rosas, A. Pérez-Centeno, I. Ceja, F. de Moure-Flores, M. Meléndez-Lira, A. Hernández-Hernández, M. A. Santana-Aranda, and J. G. Quiñones-Galván, Mater. Res. Express **5**, 015038 (2018).
66 J. Liu, C. Liang, Z. Tian, S. Zhang, and G. Shao, Sci. Rep. **3**, 1741 (2013).
67 D. Zhang, M. Lau, S. Lu, S. Barcikowski, and B. Gökce, Sci. Rep. **7**, 40355 (2017).
68 M. I. Mendivil, B. Krishnan, F. A. Sanchez, S. Martinez, J. A. Aguilar-Martinez, G. A. Castillo, D. I. Garcia-Gutierrez, and S. Shaji, Appl. Phys. A **110**, 809 (2013).
69 Y. Cai, Y. Ye, P. Li, Y. Zhou, J. Liu, Z. Tian, Z. Yang, and C. Liang, Appl. Surf. Sci. **473**, 564 (2019).
70 J. Kou, Y. Wang, X. Liu, X. Zhang, G. Chen, X. Xu, J. Bao, K. Yang, and L. Yuwen, Sci. Rep. **10**, 15095 (2020).
71 K. Zhang, R. A. Ganeev, G. S. Boltaev, P. V. Redkin, P. S. Krishnendu, and C. Guo, Colloids Surf. A-Physicochem. Eng. Aspects **584**, 124016 (2020).
72 R. A. Ganeev, and A. S. Alnaser, Opt. Spectrosc. **127**, 1155 (2019).
73 V. Y. Shur, E. V. Gunina, A. A. Esin, E. V. Shishkina, D. K. Kuznetsov, E. A. Linker, E. D. Greshnyakov, and V. I. Pryakhina, Appl. Surf. Sci. **483**, 835 (2019).
74 K. Y. Niu, J. Yang, S. A. Kulinich, J. Sun, H. Li, and X. W. Du, J. Am. Chem. Soc. **132**, 9814 (2010).
75 T. Tsuji, M. Nakanishi, T. Mizuki, S. Ozono, M. Tsuji, and Y. Tsuboi, Sci. Adv. Mater. **4**, 391 (2012).
76 Y. Wang, N. S. Reddy Satyavolu, and Y. Lu, Curr. Opin. Colloid Interface Sci. **38**, 158 (2018).
77 A. R. Tao, S. Habas, and P. Yang, Small **4**, 310 (2008).
78 Z. Peng, and H. Yang, Nano Today **4**, 143 (2009).
79 K. Kodama, T. Nagai, A. Kuwaki, R. Jinnouchi, and Y. Morimoto, Nat. Nanotechnol. **16**, 140 (2021).
80 M. R. Kalus, N. Bärsch, R. Streubel, E. Gökce, S. Barcikowski, and B. Gökce, Phys. Chem. Chem. Phys. **19**, 7112 (2017).
81 M. M. ElFaham, M. Okil, and A. M. Mostafa, J. Opt. Soc. Am. B **37**, 2620 (2020).
82 S. S. Makridis, E. I. Gkanas, G. Panagakos, E. S. Kikkinides, A. K. Stubos, P. Wagener, and S. Barcikowski, Int. J. Hydrogen Energy **38**, 11530 (2013).
83 R. A. Ismail, K. S. Khashan, M. F. Jawad, A. M. Mousa, and F. Mahdi, Mater. Res. Express **5**, 055018 (2018).
84 V. A. Svetlichnyi, D. A. Goncharov, I. N. Lapin, and A. V. Shabalina, Russ. Phys. J. **61**, 1047 (2018).
85 A. L. Nemoykina, A. V. Shabalina, and V. A. Svetlichnyi, J. Cultural Heritage **39**, 42 (2019).
86 F. Abrinaei, J. Opt. Soc. Am. B **33**, 864 (2016).
87 P. Wang, Y. Ye, D. Liang, H. Sun, J. Liu, Z. Tian, and C. Liang, RSC Adv. **6**, 26977 (2016).
88 Z. Yan, R. Bao, C. M. Busta, and D. B. Chrisey, Nanotechnology **22**, 265610 (2011).
89 H. Pereira, C. G. Moura, G. Miranda, and F. S. Silva, Opt. Laser Tech. **142**, 107181 (2021).
90 C. Liang, T. Sasaki, Y. Shimizu, and N. Koshizaki, Chem. Phys. Lett. **389**, 58 (2004).
91 F. Abrinaei, J. Eur. Opt. Soc.-Rapid Publ. **13**, 15 (2017).
92 A. A. Pilarska, Ł. Klapiszewski, and T. Jesionowski, Powder Tech. **319**, 373 (2017).
93 Z. Yan, Q. Zhao, and D. B. Chrisey, Mater. Chem. Phys. **130**, 403 (2011).
94 M. S. Mastuli, N. Kamarulzaman, M. A. Nawawi, A. M. Mahat, R. Rusdi, and N. Kamarudin, Nanoscale Res Lett **9**, 134 (2014).
95 Y. Kato, Y. Sasaki, and Y. Yoshizawa, Energy **30**, 2144 (2005).

96 D. Jin, X. Gu, X. Yu, G. Ding, H. Zhu, and K. Yao, Mater. Chem. Phys. **112**, 962 (2008).
97 Y. Kato, K. Kobayashi, and Y. Yoshizawa, Appl. Thermal Eng. **18**, 85 (1998).
98 L. Yan, J. Zhuang, X. Sun, Z. Deng, and Y. Li, Mater. Chem. Phys. **76**, 119 (2002).
99 N. Takada, T. Sasaki, and K. Sasaki, Appl. Phys. A **93**, 833 (2008).
100 A. De Bonis, A. Santagata, A. Galasso, A. Laurita, and R. Teghil, J. Colloid Interface Sci. **489**, 76 (2017).
101 D. Zhang, C. Zhang, J. Liu, Q. Chen, X. Zhu, and C. Liang, ACS Appl. Nano Mater. **2**, 28 (2019).
102 P. G. Kuzmin, G. A. Shafeev, G. Viau, B. Warot-Fonrose, M. Barberoglou, E. Stratakis, and C. Fotakis, Appl. Surf. Sci. **258**, 9283 (2012).
103 M. Boutinguiza, B. Rodriguez-Gonzalez, J. del Val, R. Comesaña, F. Lusquiños, and J. Pou, Appl. Surf. Sci. **258**, 9484 (2012).
104 A. Abdolvand, S. Z. Khan, Y. Yuan, P. L. Crouse, M. J. J. Schmidt, M. Sharp, Z. Liu, and L. Li, Appl. Phys. A **91**, 365 (2008).
105 M. Zimbone, M. A. Buccheri, G. Cacciato, R. Sanz, G. Rappazzo, S. Boninelli, R. Reitano, L. Romano, V. Privitera, and M. G. Grimaldi, Appl. Catal. B-Environ. **165**, 487 (2015).
106 C. H. Liang, Y. Shimizu, T. Sasaki, and N. Koshizaki, Appl. Phys. A **80**, 819 (2005).
107 A. Nath, S. S. Laha, and A. Khare, Appl. Surf. Sci. **257**, 3118 (2011).
108 P. Liu, W. Cai, L. Wan, M. Shi, X. Luo, and W. Jing, Trans. Nonferrous Met. Soc. China **19**, s743 (2009).
109 P. Liu, W. Cai, M. Fang, Z. Li, H. Zeng, J. Hu, X. Luo, and W. Jing, Nanotechnology **20**, 285707 (2009).
110 A. Nath, and A. Khare, J. Opt. Soc. Am. B **29**, 351 (2012).
111 A. M. Haleem, R. H. Abbas, M. A. Jawad, and F. Alberaqdar, Toxicol. Environ. Health Sci. **11**, 219 (2019).
112 M. Boutinguiza, B. Rodríguez-González, J. del Val, R. Comesaña, F. Lusquiños, and J. Pou, Nanotechnology **22**, 195606 (2011).
113 H. Zhang, C. Liang, J. Liu, Z. Tian, G. Wang, and W. Cai, Langmuir **28**, 3938 (2012).
114 K. Siuzdak, M. Sawczak, M. Klein, G. Nowaczyk, S. Jurga, and A. Cenian, Phys. Chem. Chem. Phys. **16**, 15199 (2014).
115 C. H. Wu, S. Y. Chen, and P. Shen, CrystEngComm **16**, 2220 (2014).
116 H. Zhang, and J. F. Banfield, J. Mater. Chem. **8**, 2073 (1998).
117 G. Guisbiers, O. Van Overschelde, and M. Wautelet, Appl. Phys. Lett. **92**, 103121 (2008).
118 H. Zhang, and J. F. Banfield, J. Phys. Chem. B **104**, 3481 (2000).
119 P. Jafarkhani, S. Dadras, M. J. Torkamany, and J. Sabbaghzadeh, Appl. Surf. Sci. **256**, 3817 (2010).
120 P. Galizia, G. Maizza, and C. Galassi, Process. Appl. Ceram. **10**, 235 (2016).
121 P. Sharma, and A. Nath, Laser Phys. **30**, 086002 (2020).
122 F. Barreca, N. Acacia, E. Barletta, D. Spadaro, G. Currò, and F. Neri, Appl. Surf. Sci. **256**, 6408 (2010).
123 S. C. Singh, R. K. Swarnkar, and R. Gopal, J. Nanosci. Nanotechnol. **9**, 5367 (2009).
124 N. G. Semaltianos, S. Logothetidis, N. Frangis, I. Tsiaoussis, W. Perrie, G. Dearden, and K. G. Watkins, Chem. Phys. Lett. **496**, 113 (2010).
125 G. G. Guillén, S. Shaji, M. I. M. Palma, D. Avellaneda, G. A. Castillo, T. K. D. Roy, D. I. G. Gutiérrez, and B. Krishnan, Appl. Surf. Sci. **405**, 183 (2017).
126 D. Ettel, O. Havelka, S. Isik, D. Silvestri, S. Wacławek, M. Urbánek, V. V. T. Padil, M. Černík, F. Yalcinkaya, and R. Torres-Mendieta, Appl. Surf. Sci. **564**, 150471 (2021).
127 A. Singh, T. Salminen, M. Honkanen, J. Vihinen, L. Hyvärinen, and E. Levänen, Appl. Surf. Sci. **476**, 822 (2019).
128 A. Chaturvedi, M. P. Joshi, P. Mondal, A. K. Sinha, and A. K. Srivastava, Appl. Surf. Sci. **396**, 303 (2017).
129 X. M.. Liu, J. He, J. Lu, and X. W. Ni, Chin. Phys. B **17**, 2574 (2008).
130 D. W. Fuerstenau, J. Colloid Interface Sci. **256**, 79 (2002).
131 Y. Ishikawa, N. Koshizaki, and S. Sakaki, J. Phys. Chem. C **123**, 24934 (2019).
132 Z. Swiatkowska-Warkocka, A. Pyatenko, K. Koga, K. Kawaguchi, H. Wang, and N. Koshizaki, J. Phys. Chem. C **121**, 8177 (2017).
133 M. Zimbone, G. Cacciato, R. Sanz, R. Carles, A. Gulino, V. Privitera, and M. G. Grimaldi, Catal. Commun. **84**, 11 (2016).
134 X. Chen, C. Meng, Y. Wang, Q. Zhao, Y. Li, X. M. Chen, D. Yang, Y. Li, and Y. Zhou, ACS Sustain. Chem. Eng. **8**, 1095 (2020).
135 Y. Ye, P. Wang, H. Sun, Z. Tian, J. Liu, and C. Liang, RSC Adv. **5**, 45038 (2015).
136 K. S. Khashan, G. M. Sulaiman, F. A. Abdulameer, S. Albukhaty, M. A. Ibrahem, T. Al-Muhimeed, and A. A. AlObaid, Appl. Sci. **11**, 4623 (2021).
137 A. R. Sadrolhosseini, M. Beygisangchin, S. Shafie, S. A. Rashid, and H. Nezakati, Mater. Res. Express **8**, 105003 (2021).
138 D. Banerjee, S. S. B. Moram, C. Byram, J. Rathod, T. Jena, G. K. Podagatlapalli, and V. R. Soma, Appl. Surf. Sci. **569**, 151070 (2021).
139 D. Zhang, Z. Ma, M. Spasova, A. E. Yelsukova, S. Lu, M. Farle, U. Wiedwald, and B. Gökce, Part. Part. Syst. Charact. **34**, 1600225 (2017).
140 J. Xiao, P. Liu, Y. Liang, H. B. Li, and G. W. Yang, J. Appl. Phys. **114**, 073513 (2013).
141 H. Zhang, C. Liang, Z. Tian, G. Wang, and W. Cai, CrystEngComm **13**, 1063 (2011).
142 N. Enríquez-Sánchez, A. R. Vilchis-Nestor, S. Camacho-López, M. A. Camacho-López, and M. Camacho-López, Opt. Laser Tech. **131**, 106418 (2020).
143 R. A. Ganeev, A. S. Zakirov, G. S. Boltaev, R. I. Tugushev, T. Usmanov, P. K. Khabibullaev, T. W. Kang, and A. A. Saidov, Opt. Mater. **33**, 419 (2011).
144 H. Zhang, J. Liu, Y. Ye, Z. Tian, and C. Liang, Phys. Chem. Chem. Phys. **15**, 5684 (2013).
145 B. K. Pandey, A. K. Shahi, and R. Gopal, Appl. Surf. Sci. **283**, 430 (2013).
146 J. Xiao, X. M. Tian, C. Yang, P. Liu, N. Q. Luo, Y. Liang, H. B. Li, D. H. Chen, C. X. Wang, L. Li, and G. W. Yang, Sci. Rep. **3**, 3424 (2013).
147 H. Zhang, C. Liang, Z. Tian, G. Wang, and W. Cai, J. Phys. Chem. C **114**, 12524 (2010).
148 B. K. Pandey, A. K. Shahi, and R. Gopal, Mater. Focus **2**, 303 (2013).
149 B. A. Katsnelson, I. A. Minigaliyeva, V. G. Panov, L. I. Privalova, A. N. Varaksin, V. B. Gurvich, M. P. Sutunkova, V. Y. Shur, E. V. Shishkina, I. E. Valamina, and O. H. Makeyev, Food Chem. Toxicol. **86**, 351 (2015).
150 Q. Yuan, P. Li, J. Liu, Y. Lin, Y. Cai, Y. Ye, and C. Liang, Chem. Mater. **29**, 10198 (2017).
151 N. Elahi, and M. Rizwan, Artif. Organs **45**, 1272 (2021).
152 S. Yu, V. M. Hong Ng, F. Wang, Z. Xiao, C. Li, L. B. Kong, W. Que, and K. Zhou, J. Mater. Chem. A **6**, 9332 (2018).
153 P. Mondal, A. Anweshan, and M. K. Purkait, Chemosphere **259**, 127509 (2020).
154 D. Zhang, W. Choi, Y. Oshima, U. Wiedwald, S. H. Cho, H. P. Lin, Y. K. Li, Y. Ito, and K. Sugioka, Nanomaterials **8**, 631 (2018).
155 V. A. Svetlichnyi, A. V. Shabalina, I. N. Lapin, D. A. Goncharova, D. A. Velikanov, and A. E. Sokolov, Appl. Phys. A **123**, 763 (2017).
156 N. Lasemi, O. Bomatí Miguel, R. Lahoz, V. V. Lennikov, U. Pacher, C. Rentenberger, and W. Kautek, ChemPhysChem **19**, 1414 (2018).
157 A. De Bonis, T. Lovaglio, A. Galasso, A. Santagata, and R. Teghil, Appl. Surf. Sci. **353**, 433 (2015).
158 L. Franzel, M. F. Bertino, Z. J. Huba, and E. E. Carpenter, Appl. Surf. Sci. **261**, 332 (2012).
159 V. A. Svetlichnyi, A. V. Shabalina, I. N. Lapin, D. A. Goncharova, T. S. Kharlamova, and A. I. Stadnichenko, Appl. Surf. Sci. **467-468**, 402 (2019).
160 E. Vahabzadeh, and M. J. Torkamany, J Clust Sci **25**, 959 (2014).
161 S. Amagasa, and Y. Yamada, J. Nucl. Radiochem. Sci. **19**, 14 (2019).

162 V. Amendola, M. Meneghetti, G. Granozzi, S. Agnoli, S. Polizzi, P. Riello, A. Boscaini, C. Anselmi, G. Fracasso, M. Colombatti, C. Innocenti, D. Gatteschi, and C. Sangregorio, J. Mater. Chem. **21**, 3803 (2011).
163 S. Okazoe, Y. Yasaka, M. Kudo, H. Maeno, Y. Murakami, and Y. Kimura, Chem. Commun. **54**, 7834 (2018).
164 G. Gubert, E. Ribeiro, J. Varalda, A. G. Bezerra Jr., W. H. Schreiner, and D. H. Mosca, J. Alloys Compd. **725**, 519 (2017).
165 Y. Liang, P. Liu, J. Xiao, H. Li, C. Wang, and G. Yang, Sci. Rep. **3**, 3051 (2013).
166 V. Amendola, P. Riello, and M. Meneghetti, J. Phys. Chem. C **115**, 5140 (2011).
167 M. L. Chen, Z. W. Gao, X. M. Chen, S. C. Pang, and Y. Zhang, Talanta **182**, 433 (2018).
168 P. Liu, W. Cai, and H. Zeng, J. Phys. Chem. C **112**, 3261 (2008).
169 S. J. Henley, S. Mollah, C. E. Giusca, and S. R. P. Silva, J. Appl. Phys. **106**, 064309 (2009).
170 Y. Yu, H. J. Jung, M. Je, H. C. Choi, and M. Y. Choi, Chemosphere **155**, 250 (2016).
171 M. Curcio, J. V. Rau, A. Santagata, R. Teghil, S. Laureti, and A. De Bonis, Mater. Chem. Phys. **225**, 365 (2019).
172 A. Durdureanu-Angheluta, C. Mihesan, F. Doroftei, A. Dascalu, L. Ursu, M. Velegrakis, and M. Pinteala, Acad. Romana **59**, 151 (2014).
173 A. Kanitz, J. S. Hoppius, M. Del Mar Sanz, M. Maicas, A. Ostendorf, and E. L. Gurevich, ChemPhysChem **18**, 1155 (2017).
174 R. Lahoz, E. Natividad, Á. Mayoral, C. Rentenberger, D. Díaz-Fernández, E. J. Félix, L. Soriano, W. Kautek, and O. Bomati-Miguel, J. Indust. Eng. Chem. **81**, 340 (2019).
175 F. Davodi, E. Mühlhausen, D. Settipani, E. L. Rautama, A. P. Honkanen, S. Huotari, G. Marzun, P. Taskinen, and T. Kallio, J. Colloid Interface Sci. **556**, 180 (2019).
176 X. Luo, A. H. M. Al-Antaki, T. M. D. Alharbi, W. D. Hutchison, Y. C. Zou, J. Zou, A. Sheehan, W. Zhang, and C. L. Raston, ACS Omega **3**, 11172 (2018).
177 G. S. Demirer, A. C. Okur, and S. Kizilel, J. Mater. Chem. B **3**, 7831 (2015).
178 J. Britton, K. A. Stubbs, G. A. Weiss, and C. L. Raston, Chem. Eur. J. **23**, 13270 (2017).
179 V. Amendola, P. Riello, S. Polizzi, S. Fiameni, C. Innocenti, C. Sangregorio, and M. Meneghetti, J. Mater. Chem. **21**, 18665 (2011).
180 R. A. Ismail, G. M. Sulaiman, S. A. Abdulrahman, and T. R. Marzoog, Mater. Sci. Eng.-C **53**, 286 (2015).
181 A. Richter, Y. Li, C. Rehbock, S. Barcikowski, A. Haverich, M. Wilhelmi, and U. Böer, Adv Mater. Inter. **8**, 2002015 (2021).
182 M. A. Al-Kinani, A. J. Haider, and S. Al-Musawi, Plasmonics **16**, 1107 (2021).
183 P. Kupracz, E. Coy, K. Grochowska, J. Karczewski, J. Rysz, and K. Siuzdak, Appl. Surf. Sci. **530**, 147097 (2020).
184 C. Zhang, J. Liu, Y. Ye, Z. Aslam, R. Brydson, and C. Liang, ACS Appl. Mater. Interfaces **10**, 2423 (2018).
185 J. D. Blakemore, H. B. Gray, J. R. Winkler, and A. M. Müller, ACS Catal. **3**, 2497 (2013).
186 B. K. Pandey, A. K. Shahi, and R. Gopal, Appl. Surf. Sci. **347**, 461 (2015).
187 D. Liang, S. Wu, J. Liu, Z. Tian, and C. Liang, J. Mater. Chem. A **4**, 10609 (2016).
188 S. Hu, C. Melton, and D. Mukherjee, Phys. Chem. Chem. Phys. **16**, 24034 (2014).
189 D. Liang, Z. Tian, J. Liu, Y. Ye, S. Wu, Y. Cai, and C. Liang, Electrochim. Acta **182**, 376 (2015).
190 Y. Liang, P. Liu, J. Xiao, H. B. Li, C. X. Wang, and G. W. Yang, Laser Phys. Lett. **11**, 056001 (2014).
191 M. Yu, F. Waag, C. K. Chan, C. Weidenthaler, S. Barcikowski, and H. Tüysüz, ChemSusChem **13**, 520 (2020).
192 E. Budiyanto, S. Zerebecki, C. Weidenthaler, T. Kox, S. Kenmoe, E. Spohr, S. DeBeer, O. Rüdiger, S. Reichenberger, S. Barcikowski, and H. Tüysüz, ACS Appl. Mater. Interfaces **13**, 51962 (2021).
193 H. Zhang, C. Liang, J. Liu, Z. Tian, and G. Shao, Carbon **55**, 108 (2013).
194 J. Zhang, and C. Q. Lan, Mater. Lett. **62**, 1521 (2008).
195 Y. Zhu, Z. Li, Z. Xiao, W. Qiu, M. Fang, and Z. Chen, Mater. Charact. **163**, 110290 (2020).
196 Y. T. Zhu, X. Y. Zhang, and Q. Liu, Mater. Sci. Eng.-A **528**, 8145 (2011).
197 E. L. Ribeiro, S. A. Davari, S. Hu, D. Mukherjee, and B. Khomami, Mater. Chem. Front. **3**, 1302 (2019).
198 E. L. Ribeiro, E. M. Davis, M. Mokhtarnejad, S. Hu, D. Mukherjee, and B. Khomami, Catal. Sci. Technol. **11**, 3002 (2021).
199 L. Jyothi, R. Kuladeep, and D. N. Rao, J. Nanophoton. **9**, 093088 (2015).
200 V. Shukla, C. P. Singh, C. Mukherjee, and K. S. Bindra, Chem. Phys. Lett. **555**, 149 (2013).
201 C. Zhang, J. Liu, Y. Ye, Q. Chen, and C. Liang, Carbon **156**, 31 (2020).
202 Y. L. Chang, S. S. Lin, Y. Zheng, P. Shen, and S. Y. Chen, Appl. Phys. A **123**, 238 (2017).
203 D. Muñetón Arboleda, J. M. J. Santillán, L. J. Mendoza Herrera, M. B. F. van Raap, P. Mendoza Zélis, D. Muraca, D. C. Schinca, and L. B. Scaffardi, J. Phys. Chem. C **119**, 13184 (2015).
204 D. Zhang, B. Ranjan, T. Tanaka, and K. Sugioka, ACS Appl. Nano Mater. **3**, 1855 (2020).
205 H. J. Jung, and M. Y. Choi, J. Phys. Chem. C **118**, 14647 (2014).
206 O. R. Musaev, J. Yan, V. Dusevich, J. M. Wrobel, and M. B. Kruger, Appl. Phys. A **116**, 735 (2014).
207 R. G. Nikov, N. N. Nedyalkov, and D. B. Karashanova, Appl. Surf. Sci. **518**, 146211 (2020).
208 R. Ma, D. Amaranatha Reddy, and T. K. Kim, Bull. Korean Chem. Soc **36**, 5 (2015).
209 A. M. Mostafa, and E. A. Mwafy, Environ. Nanotechnol. Monitoring Manage. **14**, 100382 (2020).
210 H. Sun, Y. Ye, J. Liu, Z. Tian, Y. Cai, P. Li, and C. Liang, Chem. Commun. **54**, 1563 (2018).
211 M. Mardis, N. Takada, S. Machmudah, S. Wahyudiono, K. Sasaki, H. Kanda, and M. Goto, Res. Chem. Intermed. **42**, 4581 (2015).
212 S. Z. Khan, Y. Yuan, A. Abdolvand, M. Schmidt, P. Crouse, L. Li, Z. Liu, M. Sharp, and K. G. Watkins, J. Nanopart. Res. **11**, 1421 (2009).
213 M. K. Singh, A. Agarwal, R. Gopal, R. K. Swarnkar, and R. K. Kotnala, J. Mater. Chem. **21**, 11074 (2011).
214 T. Zhang, Z. Wang, and D. J. Hwang, Appl. Phys. A **123**, 616 (2017).
215 H. J. Jung, and M. Y. Choi, Appl. Surf. Sci. **457**, 1050 (2018).
216 S. Kim, B. K. Yoo, K. Chun, W. Kang, J. Choo, M. S. Gong, and S. W. Joo, J. Mol. Catal. A-Chem. **226**, 231 (2005).
217 P. K. Baruah, A. K. Sharma, and A. Khare, RSC Adv. **9**, 15124 (2019).
218 D. O. O. Galindo, and E. O. Contreras, J. Laser Micro Nanoeng. **12,** 304 (2017).
219 M. Fernández-Arias, M. Boutinguiza, J. Del Val, C. Covarrubias, F. Bastias, L. Gómez, M. Maureira, F. Arias-González, A. Riveiro, and J. Pou, Appl. Surf. Sci. **507**, 145032 (2020).
220 T. Begildayeva, S. J. Lee, Y. Yu, J. Park, T. H. Kim, J. Theerthagiri, A. Ahn, H. J. Jung, and M. Y. Choi, J. Hazard. Mater. **409**, 124412 (2020).
221 M. Khademian, M. Zandi, M. Amirhoseiny, and D. Dorranian, J. Clust. Sci. **28**, 2753 (2017).
222 G. Marzun, H. Bönnemann, C. Lehmann, B. Spliethoff, C. Weidenthaler, and S. Barcikowski, ChemPhysChem **18**, 1175 (2017).
223 D. A. Goncharova, T. S. Kharlamova, O. A. Reutova, and V. A. Svetlichnyi, Colloids Surf. A-Physicochem. Eng. Aspects **613**, 126115 (2021).
224 R. K. Swarnkar, J. K. Pandey, K. K. Soumya, P. Dwivedi, S. Sundaram, S. Prasad, and R. Gopal, Appl. Phys. A **122**, 704 (2016).
225 P. K. Baruah, A. K. Sharma, and A. Khare, Opt. Laser Tech. **108**, 574 (2018).
226 K. Amikura, T. Kimura, M. Hamada, N. Yokoyama, J. Miyazaki, and

Y. Yamada, Appl. Surf. Sci. **254**, 6976 (2008).
227 K. Zhang, R. A. Ganeev, G. S. Boltaev, and C. Guo, Appl. Phys. A **125**, 698 (2019).
228 X. Z. Lin, P. Liu, J. M. Yu, and G. W. Yang, J. Phys. Chem. C **113**, 17543 (2009).
229 K. D. Malviya, and K. Chattopadhyay, J. Mater. Sci. **50**, 980 (2015).
230 T. Begildayeva, A. Ahn, S. S. Naik, S. J. Lee, J. Theerthagiri, T. H. Kim, and M. Y. Choi, Sci. Rep. **11**, 14389 (2021).
231 D. A. Goncharova, T. S. Kharlamova, I. N. Lapin, and V. A. Svetlichnyi, J. Phys. Chem. C **123**, 21731 (2019).
232 D. P. Singh, A. K. Ojha, and O. N. Srivastava, J. Phys. Chem. C **113**, 3409 (2009).
233 R. Rawat, A. Tiwari, N. Arun, S. V. S. N. Rao, A. P. Pathak, S. V. Rao, and A. Tripathi, Appl. Phys. A **126**, 226 (2020).
234 K. Sugioka, and Y. Cheng, Appl. Phys. Rev. **1**, 041303 (2014).
235 Z. Li, C. K. Dong, J. Yang, S. Z. Qiao, and X. W. Du, J. Mater. Chem. A **4**, 2699 (2016).
236 T. Khamliche, S. Khamlich, M. K. Moodley, B. M. Mothudi, M. Henini, and M. Maaza, J. Mol. Liquids **323**, 114975 (2021).
237 X. Kang, D. Teng, S. Wu, Z. Tian, J. Liu, P. Li, Y. Ma, and C. Liang, J. Colloid Interface Sci. **566**, 265 (2020).
238 D. Longano, N. Ditaranto, N. Cioffi, F. Di Niso, T. Sibillano, A. Ancona, A. Conte, M. A. Del Nobile, L. Sabbatini, and L. Torsi, Anal. Bioanal. Chem. **403**, 1179 (2012).
239 D. Longano, N. Ditaranto, N. Cioffi, F. Di Niso, T. Sibillano, F. P. Mezzapesa, A. Ancona, A. Conte, M. A. Del Nobile, L. Sabbatini, and L. Torsi, MRS Proc. **1453**, mrss12-1453-gg11-03 (2012).
240 M. C. Sportelli, M. Izzi, A. Volpe, V. Lacivita, M. Clemente, C. Di Franco, A. Conte, M. A. Del Nobile, A. Ancona, and N. Cioffi, Food Packag. Shelf Life **22**, 100422 (2019).
241 A. A. Menazea, and M. K. Ahmed, Nano-Struct. Nano-Objects **22**, 100464 (2020).
242 S. Shahidi, M. Rashidian, and D. Dorranian, Opt. Laser Tech. **99**, 145 (2018).
243 M. A. Gondal, Q. A. Drmosh, Z. H. Yamani, and T. A. Saleh, Appl. Surf. Sci. **256**, 298 (2009).
244 H. S. Desarkar, P. Kumbhakar, and A. K. Mitra, Laser Phys. Lett. **10**, 055903 (2013).
245 P. Camarda, L. Vaccaro, A. Sciortino, F. Messina, G. Buscarino, S. Agnello, F. M. Gelardi, R. Popescu, R. Schneider, D. Gerthsen, and M. Cannas, Appl. Surf. Sci. **506**, 144954 (2020).
246 E. Solati, L. Dejam, and D. Dorranian, Opt. Laser Tech. **58**, 26 (2014).
247 E. Fazio, A. Cacciola, A. M. Mezzasalma, G. Mondio, F. Neri, and R. Saija, J. Quant. Spectr. Radiat. Transfer **124**, 86 (2013).
248 W. Soliman, N. Takada, N. Koshizaki, and K. Sasaki, Appl. Phys. A **110**, 779 (2013).
249 P. Camarda, L. Vaccaro, F. Messina, and M. Cannas, Appl. Phys. Lett. **107**, 013103 (2015).
250 S. Reich, J. Göttlicher, A. Letzel, B. Gökce, S. Barcikowski, T. dos Santos Rolo, T. Baumbach, and A. Plech, Appl. Phys. A **124**, 71 (2017).
251 B. C. Lin, P. Shen, and S. Y. Chen, J. Phys. Chem. C **115**, 5003 (2011).
252 F. Ataei, D. Dorranian, and N. Motakef-Kazemi, J. Mater. Sci.-Mater. Electron. **32**, 3819 (2021).
253 M. Honda, T. Goto, T. Owashi, A. G. Rozhin, S. Yamaguchi, T. Ito, and S. A. Kulinich, Phys. Chem. Chem. Phys. **18**, 23628 (2016).
254 Y. Ishikawa, Y. Shimizu, T. Sasaki, and N. Koshizaki, J. Colloid Interface Sci. **300**, 612 (2006).
255 N. Yudasari, P. A. Wiguna, W. Handayani, M. M. Suliyanti, and C. Imawan, Appl. Phys. A **127**, 56 (2021).
256 A. M. Mostafa, and E. A. Mwafy, J. Mater. Res. Tech. **9**, 3241 (2020).
257 S. Li, M. Chen, and X. D. Liu, Opt. Express **22**, 18707 (2014).
258 B. C. Lin, P. Shen, and S. Y. Chen, J. Nanopart. Res. **16**, 2444 (2014).
259 Z. Yan, R. Bao, and D. B. Chrisey, Chem. Phys. Lett. **497**, 205 (2010).
260 S. C. Singh, R. K. Swarnkar, and R. Gopal, Bull. Mater. Sci. **33**, 21 (2010).
261 S. C. Singh, and R. Gopal, Phys. E **40**, 724 (2008).
262 H. Zeng, W. Cai, Y. Li, J. Hu, and P. Liu, J. Phys. Chem. B **109**, 18260 (2005).
263 M. Tajdidzadeh, A. Zakaria, Z. A. Talib, A. Nisar, M. B. Kanoun, and S. Goumri-Said, Laser Phys. Lett. **16**, 055603 (2019).
264 S. I. Al-Nassar, F. I. Hussein, and A. K. M, J. Mater. Res. Tech. **8**, 4026 (2019).
265 R. A. Ismail, N. F. Habubi, and E. H. Hadi, Optik **147**, 391 (2017).
266 F. S. Alamro, A. M. Mostafa, H. A. Ahmed, and A. Toghan, Surf. Interfaces **26**, 101406 (2021).
267 A. Yazdanpanah, S. Shahidi, D. Dorranian, and S. Saviz, J. Text. Inst. **113**, 255 (2021).
268 K. S. Choi, H. C. Lichtenegger, G. D. Stucky, and E. W. McFarland, J. Am. Chem. Soc. **124**, 12402 (2002).
269 S. Abdi, and D. Dorranian, Opt. Laser Tech. **108**, 372 (2018).
270 N. Mintcheva, A. A. Aljulaih, W. Wunderlich, S. A. Kulinich, and S. Iwamori, Materials **11**, 1127 (2018).
271 S. U. Awan, S. K. Hasanain, J. Rashid, S. Hussain, S. A. Shah, M. Z. Hussain, M. Rafique, M. Aftab, and R. Khan, Mater. Chem. Phys. **211**, 510 (2018).
272 Y. Kang, F. Yu, L. Zhang, W. Wang, L. Chen, and Y. Li, Solid State Ion. **360**, 115544 (2021).
273 R. Kumar, A. Umar, G. Kumar, and H. S. Nalwa, Ceram. Int. **43**, 3940 (2017).
274 J. Wang, R. Chen, L. Xiang, and S. Komarneni, Ceram. Int. **44**, 7357 (2018).
275 E. A. Gavrilenko, D. A. Goncharova, I. N. Lapin, M. A. Gerasimova, and V. A. Svetlichnyi, Russ. Phys. J. **63**, 1429 (2020).
276 H. Zeng, W. Cai, P. Liu, X. Xu, H. Zhou, C. Klingshirn, and H. Kalt, ACS Nano **2**, 1661 (2008).
277 S. Wu, P. Wang, Y. Cai, D. Liang, Y. Ye, Z. Tian, J. Liu, and C. Liang, RSC Adv. **5**, 9069 (2015).
278 N. Yudasari, M. M. Suliyanti, and C. Imawan, Adv. Nat. Sci-Nanosci. Nanotechnol. **11**, 025003 (2020).
279 K. A. Elsayed, M. Alomari, Q. A. Drmosh, M. Alheshibri, A. Al Baroot, T. S. Kayed, A. A. Manda, and A. L. Al-Alotaibi, Alex. Eng. J. **61**, 1449 (2022).
280 Y. Zhao, S. Li, Y. Zeng, and Y. Jiang, APL Mater. **3**, 086103 (2015).
281 H. Zhang, S. Wu, J. Liu, Y. Cai, and C. Liang, Phys. Chem. Chem. Phys. **18**, 22503 (2016).
282 Z. P. Lu, W. J. Zhu, T. C. Lu, C. M. Meng, L. Xu, and X. H. Li, Acta Phys. Sin. **62**, 176402 (2013).
283 B. Pang, Y. Ma, Z. Tian, J. Liu, S. Wu, D. Teng, P. Li, and C. Liang, J. Colloid Interface Sci. **585**, 452 (2021).
284 Z. Zhao, C. Meng, P. Li, W. Zhu, Q. Wang, Y. Ma, G. Shen, L. Bai, H. He, D. He, D. Yu, J. He, B. Xu, and Y. Tian, Nanoscale **6**, 10370 (2014).
285 M. Zhao, Z. D. Hood, M. Vara, K. D. Gilroy, M. Chi, and Y. Xia, ACS Nano **13**, 7241 (2019).
286 L. Xu, D. Liu, D. Chen, H. Liu, and J. Yang, Heliyon **5**, e01165 (2019).
287 G. A. Volpato, D. Muneton Arboleda, R. Brandiele, F. Carraro, G. B. Sartori, A. Cardelli, D. Badocco, P. Pastore, S. Agnoli, C. Durante, V. Amendola, and A. Sartorel, Nanoscale Adv. **1**, 4296 (2019).
288 E. Fazio, S. G. Leonardi, M. Santoro, N. Donato, G. Neri, and F. Neri, Sens. Actuat. B-Chem. **262**, 79 (2018).
289 J. Quinson, and K. M. Ø. Jensen, Adv. Colloid Interface Sci. **286**, 102300 (2020).
290 M. Kottwitz, Y. Li, H. Wang, A. I. Frenkel, and R. G. Nuzzo, Chemistry-Methods **1**, 278 (2021).
291 J. Wu, and H. Yang, Acc. Chem. Res. **46**, 1848 (2013).
292 Z. Yan, R. Bao, and D. B. Chrisey, Nanotechnology **21**, 145609 (2010).
293 R. Streubel, S. Barcikowski, and B. Gökce, Opt. Lett. **41**, 1486

(2016).
294 M. Cueto, M. Sanz, M. Oujja, F. Gámez, B. Martínez-Haya, and M. Castillejo, J. Phys. Chem. C **115**, 22217 (2011).
295 T. Tsuji, Y. Suzuki, S. Sakaki, Y. Ishikawa, and N. Koshizaki, Elect. Comm. Jpn. **104**, e12330 (2021).
296 F. Mafuné, J. Kohno, Y. Takeda, and T. Kondow, J. Phys. Chem. B **107**, 4218 (2003).
297 A. R. Sadrolhosseini, M. Habibiasr, S. Shafie, H. Solaimani, and H. N. Lim, Int. J. Mol. Sci. **20**, 6153 (2019).
298 S. Moniri, M. R. Hantehzadeh, M. Ghoranneviss, and M. A. Asadabad, Appl. Phys. A **123**, 684 (2017).
299 W. T. Nichols, T. Sasaki, and N. Koshizaki, J. Appl. Phys. **100**, 114912 (2006).
300 F. Mafuné, and T. Kondow, Chem. Phys. Lett. **383**, 343 (2004).
301 X. X. Wang, J. Sokolowski, H. Liu, and G. Wu, Chin. J. Catal. **41**, 739 (2020).
302 S. Moniri, M. Reza Hantehzadeh, M. Ghoranneviss, and M. Asadi Asadabad, Eur. Phys. J. Plus **132**, 318 (2017).
303 M. I. Mendivil Palma, B. Krishnan, G. A. C. Rodriguez, T. K. Das Roy, D. A. Avellaneda, and S. Shaji, J. Nanomater. **2016**, 1 (2016).
304 S. Jendrzej, B. Gökce, V. Amendola, and S. Barcikowski, J. Colloid Interface Sci. **463**, 299 (2016).
305 T. Y. Sun, S. S. Lin, S. Chen, and P. Shen, Mater. Chem. Phys. **205**, 120 (2018).
306 S. Kohsakowski, F. Seiser, J. P. Wiederrecht, S. Reichenberger, T. Vinnay, S. Barcikowski, and G. Marzun, Nanotechnology **31**, 095603 (2019).
307 S. Kohsakowski, R. Streubel, I. Radev, V. Peinecke, S. Barcikowski, G. Marzun, and S. Reichenberger, Appl. Surf. Sci. **467-468**, 486 (2019).
308 H. Mateos, R. A. Picca, A. Mallardi, M. Dell'Aglio, A. De Giacomo, N. Cioffi, and G. Palazzo, Appl. Sci. **10**, 4169 (2020).
309 I. Haxhiaj, S. Tigges, D. Firla, X. Zhang, U. Hagemann, T. Kondo, J. Nakamura, G. Marzun, and S. Barcikowski, Appl. Surf. Sci. **469**, 811 (2018).
310 M. Fischer, J. Hormes, G. Marzun, P. Wagener, U. Hagemann, and S. Barcikowski, Langmuir **32**, 8793 (2016).
311 V. Ramesh, C. Rehbock, B. Giera, J. J. Karnes, J. B. Forien, S. D. Angelov, K. Schwabe, J. K. Krauss, and S. Barcikowski, Langmuir **37**, 9724 (2021).
312 Y. Yang, M. Shi, Q. F. Zhou, Y. S. Li, and Z. W. Fu, Electrochem. Commun. **20**, 11 (2012).
313 E. Bertin, A. Münzer, S. Reichenberger, R. Streubel, T. Vinnay, H. Wiggers, C. Schulz, S. Barcikowski, and G. Marzun, Appl. Surf. Sci. **467-468**, 1181 (2019).
314 G. Marzun, C. Streich, S. Jendrzej, S. Barcikowski, and P. Wagener, Langmuir **30**, 11928 (2014).
315 O. Al-Madanat, M. Curti, C. Günnemann, Y. AlSalka, R. Dillert, and D. W. Bahnemann, Catal. Today **380**, 3 (2021).
316 E. M. Slavinskaya, A. I. Stadnichenko, V. V. Muravyov, T. Y. Kardash, E. A. Derevyannikova, V. I. Zaikovskii, O. A. Stonkus, I. N. Lapin, V. A. Svetlichnyi, and A. I. Boronin, ChemCatChem **10**, 2232 (2018).
317 E. A. Fedorova, A. I. Stadnichenko, E. M. Slavinskaya, L. S. Kibis, O. A. Stonkus, D. A. Svintsitskiy, I. N. Lapin, A. V. Romanenko, V. A. Svetlichnyi, and A. I. Boronin, J. Struct. Chem. **61**, 316 (2020).
318 E. Ogel, M. Casapu, D. E. Doronkin, R. Popescu, H. Störmer, C. Mechler, G. Marzun, S. Barcikowski, M. Türk, and J. D. Grunwaldt, J. Phys. Chem. C **123**, 5433 (2019).
319 K. N. Madlum, E. Jasim Khamees, S. Abdulridha Ahmed, and R. Akram Naji, J. Nanostruct. **11**, 13 (2021).
320 H. Itohiya, Y. Matsushima, S. Shirakawa, S. Kajiyama, A. Yashima, T. Nagano, and K. Gomi, PLoS ONE **14**, e0222634 (2019).
321 M. Cueto, M. Piedrahita, C. Caro, B. Martínez-Haya, M. Sanz, M. Oujja, and M. Castillejo, J. Phys. Chem. C **118**, 11432 (2014).
322 S. Sarkar, and S. C. Peter, Inorg. Chem. Front. **5**, 2060 (2018).
323 B. P. Chaplin, M. Reinhard, W. F. Schneider, C. Schüth, J. R. Shapley, T. J. Strathmann, and C. J. Werth, Environ. Sci. Technol. **46**, 3655 (2012).
324 M. P. Navas, and R. K. Soni, Appl. Surf. Sci. **390**, 718 (2016).
325 T. Nishi, A. Takeichi, H. Azuma, N. Suzuki, T. Hioki, and T. Motohiro, J. Laser Micro Nanoeng. **5**, 192 (2010).
326 H. Park, D. A. Reddy, Y. Kim, S. Lee, R. Ma, and T. K. Kim, Chem. Eur. J. **23**, 13112 (2017).
327 J. Kim, D. Amaranatha Reddy, R. Ma, and T. K. Kim, Solid State Sci. **37**, 96 (2014).
328 G. Cristoforetti, E. Pitzalis, R. Spiniello, R. Ishak, F. Giammanco, M. Muniz-Miranda, and S. Caporali, Appl. Surf. Sci. **258**, 3289 (2012).
329 E. Giorgetti, P. Marsili, S. Cicchi, L. Lascialfari, M. Albiani, M. Severi, S. Caporali, M. Muniz-Miranda, A. Pistone, and F. Giammanco, J. Colloid Interface Sci. **442**, 89 (2015).
330 C. B. Hwang, Y. S. Fu, Y. L. Lu, S. W. Jang, P. T. Chou, C. R. C. Wang, and S. J. Yu, J. Catal. **195**, 336 (2000).
331 H. Park, D. A. Reddy, Y. Kim, S. Lee, R. Ma, M. Lim, and T. K. Kim, Appl. Surf. Sci. **401**, 314 (2017).
332 Y. Kim, R. Ma, D. A. Reddy, and T. K. Kim, Appl. Surf. Sci. **357**, 2112 (2015).
333 R. Zhang, L. Zhu, X. Liu, J. Zhu, and Y. Zhao, ACS Sustain. Chem. Eng. **9**, 7837 (2021).
334 M. Mehrabi, P. Parvin, A. Reyhani, and S. Z. Mortazavi, Mater. Res. Express **4**, 095030 (2017).
335 B. F. Mohazzab, B. Jaleh, M. Nasrollahzadeh, S. Khazalpour, M. Sajjadi, and R. S. Varma, ACS Omega **5**, 5888 (2020).
336 E. M. Slavinskaya, T. Y. Kardash, O. A. Stonkus, R. V. Gulyaev, I. N. Lapin, V. A. Svetlichnyi, and A. I. Boronin, Catal. Sci. Technol. **6**, 6650 (2016).
337 S. A. Davari, J. L. Gottfried, C. Liu, E. L. Ribeiro, G. Duscher, and D. Mukherjee, Appl. Surf. Sci. **473**, 156 (2019).
338 Z. Cheng, Y. Yang, F. Li, and Z. Pan, Trans. Nonferrous Met. Soc. China **18**, 378 (2008).
339 K. Park, A. Rai, and M. R. Zachariah, J. Nanopart Res. **8**, 455 (2006).
340 J. L. Gottfried, Propell. Explos. Pyrotech. **40**, 674 (2015).
341 A. Baladi, and R. Sarraf Mamoory, Appl. Surf. Sci. **256**, 7559 (2010).
342 M. M. ElFaham, M. Okil, and A. M. Mostafa, J. Appl. Phys. **128**, 153104 (2020).
343 G. Viau, V. Collière, L. M. Lacroix, and G. A. Shafeev, Chem. Phys. Lett. **501**, 419 (2011), arXiv: 1005.1461.
344 Y. Wei, Y. Gu, M. Zhao, Y. Dong, J. Chen, and H. Zeng, ACS Appl. Electron. Mater. **2**, 802 (2020).
345 R. M. Altuwirqi, B. Baatiyah, E. Nugali, Z. Hashim, and H. Al-Jawhari, J. Nanomater. **2020**, 1327868 (2020).
346 B. Kumar, and R. K. Thareja, J. Appl. Phys. **108**, 064906 (2010).
347 A. Riahi, S. Khamlich, M. Balghouthi, T. Khamliche, T. B. Doyle, W. Dimassi, A. Guizani, and M. Maaza, J. Mol. Liquids **304**, 112694 (2020).
348 V. Piriyawong, V. Thongpool, P. Asanithi, and P. Limsuwan, J. Nanomater. **2012**, 819403 (2012).
349 I. L. Liu, B. C. Lin, S. Y. Chen, and P. Shen, J. Phys. Chem. C **115**, 4994 (2011).
350 Z. Yan, R. Bao, Y. Huang, and D. B. Chrisey, J. Phys. Chem. C **114**, 11370 (2010).
351 K. Zhang, D. S. Ivanov, R. A. Ganeev, G. S. Boltaev, P. S. Krishnendu, S. C. Singh, M. E. Garcia, I. N. Zavestovskaya, and C. Guo, Nanomaterials **9**, 767 (2019).
352 W. Grochala, and P. P. Edwards, Chem. Rev. **104**, 1283 (2004).
353 I. Levin, and D. Brandon, J. Am. Ceram. Soc. **81**, 1995 (1998).
354 S. A. Al-Mamun, R. Nakajima, and T. Ishigaki, J. Colloid Interface Sci. **392**, 172 (2013).
355 O. V. Al'myasheva, E. N. Korytkova, A. V. Maslov, and V. V. Gusarov, Inorg. Mater. **41**, 460 (2005).
356 I. L. Liu, P. Shen, and S. Y. Chen, J. Phys. Chem. C **114**, 7751 (2010).
357 R. A. Ismail, S. A. Zaidan, and R. M. Kadhim, Appl. Nanosci. **7**, 477 (2017).